Resonance Raman Spectroscopy

Roman S. Czernuszewicz & Marzena B. Zaczek
University of Houston, Houston, TX, USA

METHOD SUMMARY

Acronyms, synonyms

- Resonance Raman (RR)
- Resonance Raman effect (RRE)
- Resonance Raman scattering (RRS)

Measured physical quantities

- Intensity of inelastically (Raman) scattered photons (i) as a function of the wavenumber separation (Raman shift) from the elastically (Rayleigh) scattered photons and (ii) as a function of the exciting radiation wavelengths (three-dimensional spectrum).

Information available

- Vibrational frequencies of the chromophore in resonance with incident frequency.
- Metal coordination geometry and ligand environment via analysis of vibrational frequencies.
- Metal–ligand bond strengths via analysis of vibrational frequencies.
- Electronic assignments via resonance excitation profiles (REPs).

Information NOT available, limitations

- Not useful for nonchromophoric metal sites.
- Insensitive to magnetic properties for metal centers, e.g., Zn^{2+}.
- Cannot be used for absolute quantitation of metal centers.

Examples of questions that can be answered

- What are the spin state, oxidation state, and axial ligation of this heme?
- What is the effect of this substrate/inhibitor/mutation on this metal coordination sphere?
- What type of Fe–S cluster is this?
- What is the Fe–O–Fe bond angle in this diiron center?

Major advantages

- Extremely sensitive to minor structural and electronic changes at the active site.
- Selective determination of the vibrational properties of individual chromophores possible in proteins with multiple chromophoric prosthetic groups.
- Can monitor kinetics of changes at the metal site down to the femtosecond timescale using time-resolved techniques.
- Requires minuscule amount of material for low-temperature studies (~10 µl).
- Can be used at room temperature or low temperature with (frozen) solutions, solids, or single crystals.

Major disadvantages

- Fluorescence or traces of fluorescent impurities can prevent acquisition of RR spectra.
- Meaningful vibrational analysis requires extensive isotope substitution data.
- The factors controlling the extent of resonance enhancement of discrete vibrational modes are generally not well understood.

Sample constraints

- Requires at least 10 µl of pure protein (~1 mM).

1 INTRODUCTION

Resonance Raman (RR) spectroscopy is a powerful and versatile technique for the study of both vibrational and electronic structures of chromophoric molecular systems. RR spectra are obtained by irradiation of the sample with a monochromatic light source whose energy is close to that of an electric-dipole-allowed electronic absorption band. Most of the Raman bands are attenuated by the absorption, but some bands may be greatly enhanced. This effect arises from a coupling of the electronic and vibrational transitions, and the vibrational modes that do show enhancement are localized on the chromophore, that is, on the group of atoms that give rise to the electronic transition.

Early RR spectra[1,2] indicated that only one allowed electronic transition (the resonant one) was responsible for the strongly enhanced intensity of the Raman scattering with excitation lines in the visible or near-ultraviolet region. Classical examples of these are the RR spectra of such inorganic species as MnO_4^-, CrO_4^{2-}, TiI_4, SnI_4, $Mo_2Cl_8^{4-}$, etc.[1] All of the above are characterized by an enormous enhancement of the intensity of one or more totally symmetric vibrational modes, together with an appearance of a long series of overtone bands (usually only one of the totally symmetric modes). The RR spectroscopic studies of the $Mo_2Cl_8^{4-}$ ion[3,4] had verified the close relationship between the electronic transition and the vibrational mode to be resonance enhanced.

Encyclopedia of Inorganic and Bioinorganic Chemistry, Online © 2011 John Wiley & Sons, Ltd.

This article was originally published in the *Encyclopedia of Inorganic Chemistry* in 2008 by John Wiley & Sons, Ltd.
DOI: 10.1002/9781119951438.eibc0303

This ion exhibits an intense absorption band at ~525 nm, which arises from the allowed $\delta \rightarrow \delta^*$ charge-transfer (CT) transition involving excitation of a δ-electron of the quadruple Mo–Mo bond.[5] Thus, it is not surprising that of the three totally symmetric fundamentals, ν(MoMo), ν(MoCl), and δ(ClMoCl), it was only the ν(MoMo) stretch that showed strong RR activity in the spectrum taken with excitation corresponding to the $\delta \rightarrow \delta^*$ CT transition. Similar RR spectra obtained from other metal–metal bonded $M_2X_8^{n-}$ ions[6] have led to the correction of their electronic spectra assignments in the visible region.

The advantage of selective enhancement has quickly made RR spectroscopy a favorite method for the study of relatively large molecules such as heme proteins,[7–14] whose chromophoric center is an iron porphyrin complex (*see* ***Iron Porphyrin Chemistry***). Excitations in the visible and near-ultraviolet region have produced relatively simple Raman spectra, because only the vibrations associated with the heme chromophore are resonance enhanced, but the vibrations of the surrounding polypeptide chains are not. Among those enhanced, the in-plane stretching vibrations of the porphyrin ring (1000–1700 cm^{-1}) showed the largest increase in intensity due to interactions with the $\pi \rightarrow \pi^*$ allowed electronic transitions (400–600 nm), which are also polarized in the porphyrin plane. There was further differentiation of this set, with bands enhanced depending upon whether the excitation wavelength was tuned to the near-UV (Soret) or visible bands (α and β). The RR spectra obtained by using excitation lines with $\lambda_{ex} < 500$ nm, i.e., with lines approaching the energy of the Soret band, were dominated by bands attributable to totally symmetric vibrations. On the other hand, such vibrations were not observed when $\lambda_{ex} > 500$ nm were used ($\alpha-\beta$ region). Instead, bands attributable to nontotally symmetric vibrations were strongly enhanced. This differential enhancement of the Raman bands in different scattering regimes of heme proteins is the first reported example of more complex resonance behavior under multiple resonant state conditions.[7–10] It attracted the attention of theorists and inspired the development of the vibronic theory of RR scattering (*vide infra*).

Progress in the field of Raman and RR spectroscopy has been heavily dependent on laser technology. The advent of accessible and relatively inexpensive laser sources in the early 1960s has caused a revolution in Raman techniques, by largely displacing the traditional mercury discharge lamp as a Raman excitation source. Before lasers were available, the process of obtaining a good quality Raman spectrum of anything but the most straightforward molecular systems involved as much art as science, required about 10–20 ml of sample, and was often a very time-consuming operation. While important early investigations of resonance enhancement were carried out,[15] highly colored materials could not be studied. The laser has changed this situation dramatically by providing an intense directional line source. In fact, the laser is almost ideal as a Raman excitation source; it gives a very narrow, highly monochromatic beam of intense radiation, which can be focused very precisely into a small sample under a variety of flexible sampling geometries.[16–18] The sample can be moved rapidly through the laser beam to minimize complications due to local heating or photochemistry. In addition to the development of laser technology, the introduction of extremely sensitive phototubes and later diode array transducers enabled Raman and RR spectra to be recorded photoelectrically rather than photographically, with consequent enormous saving in recording time. Further, high-quality double and triple monochromators, spectrographs, cutoff filters, and Fourier-transform Raman interferometers of high efficiency have been developed,[19] so that it is now possible to scan to within a few wavenumbers of the exciting laser line and acquire excellent quality Raman and RR spectra of any material in any physical state.

Technical advances continue to grow, and applications will certainly multiply. The purpose of this article is to lay out the principles behind RR spectroscopy and to illustrate them with examples from recent research, especially in the context of bioinorganic chemistry.

2 TECHNICAL BACKGROUND

2.1 IR and Raman Basics

Molecular vibrational frequencies (10^{-13}–10^{-14} Hz) lie in the infrared (IR) region of the electromagnetic spectrum. Transitions to vibrationally excited states can therefore be probed by direct absorption of IR photons (IR spectroscopy) (*see* ***Vibrational Spectroscopy***).[20–22] All molecules except homonuclear diatomic molecules (e.g., H_2, O_2, N_2, and the halogens) absorb IR light. In IR spectroscopy the vibrational frequency is observed as a peak in the absorption spectrum at the absolute frequency of the absorbed IR radiation. Alternatively, inelastic collisions of the sample molecules with the quanta of light in the ultraviolet, visible, or near-infrared regions can induce the same vibrational transition via an inelastic light scattering process. This Raman process is shown diagrammatically in relation to IR absorption in Figure 1. All molecules including the homonuclear diatomics are Raman scatterers. In Raman spectroscopy, the exciting photon has much higher frequency and energy than the molecular vibration. As a result of the inelastic collision, part of the incident photon energy $h\nu_0$, equal to the vibrational quantum, $\upsilon \rightarrow \upsilon'$, is retained by the vibrating molecule, while the scattered photon emerges with lower frequency, $\nu_0 - \nu_{\upsilon,\upsilon'}$, and energy $h(\nu_0 - \nu_{\upsilon,\upsilon'})$ (Stokes scattered radiation). The molecular vibration is therefore encoded in the Raman spectrum as the frequency separation between the incident photon (or the elastic scattering Rayleigh peak) and the scattered photon (Figure 2). A Raman experiment requires illuminating the sample with *monochromatic* radiation and

Encyclopedia of Inorganic and Bioinorganic Chemistry, Online © 2011 John Wiley & Sons, Ltd.

This article was originally published in the *Encyclopedia of Inorganic Chemistry* in 2008 by John Wiley & Sons, Ltd.
DOI: 10.1002/9781119951438.eibc0303

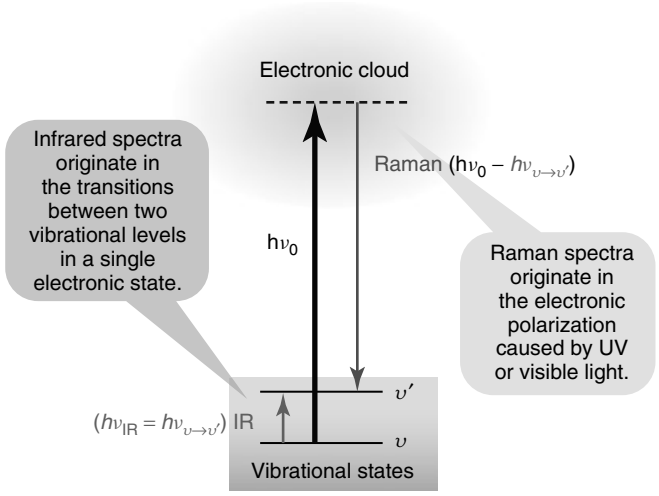

Figure 1 Origin of infrared (IR) absorption and Raman scattering spectra

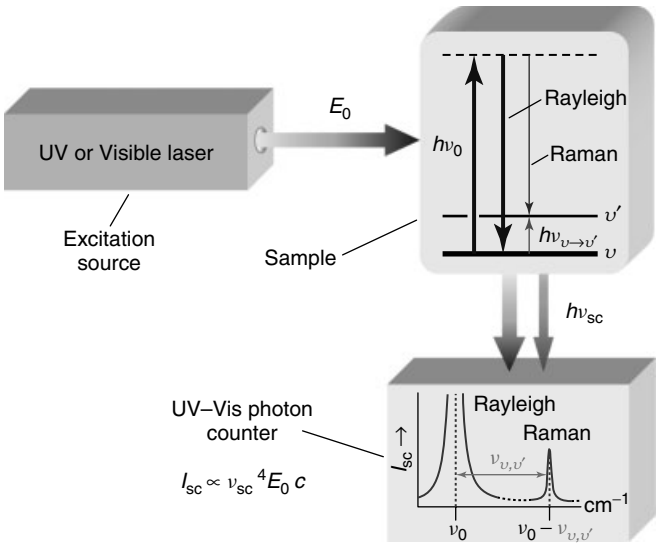

Figure 2 Measurement of scattered light at 90°: The excitation radiation for the Raman experiment must be monochromatic. Scattering of UV or visible photons produces an intense Rayleigh peak and weaker Raman peaks, displaced from the Rayleigh by $\nu_{\upsilon,\upsilon'}$. These arise because of energy transfer from the incident photon $h\nu_0$ to the molecule, which is raised to an excited vibrational level. The readout signal is proportional to the flux of the scattered light (I_{sc}), which is directly related to the fourth power of the scattered frequency (ν_{sc}), irradiance of the source (E_0), and the concentration of scattering molecules

analyzing the polychromatic radiation scattered by the sample. In practice, a monochromatic radiation of any convenient frequency from the laser is shone on to the sample and the absolute radiant power of scattering can be measured at any convenient angle with respect to the excitation beam; 90° collection geometry is shown in Figure 2.

If the incident frequency is offset to zero, then Raman peaks occur at the same frequencies as peaks in the IR spectrum. Different selection rules, however, govern the intensity of the IR- and Raman-active vibrational modes. Absorption of IR photons requires a change in the dipole moment during molecular vibration, and IR band intensity $I_{IR} \propto (\partial\mu/\partial Q_k)^2$, where μ is the dipole moment and Q_k is the vibrational coordinate. Raman scattering, on the other hand, depends on the variation of the polarizability (or induced dipole moment) of the molecule, α, during vibration, and Raman band intensity $I_R \propto (\partial\alpha/\partial Q_k)^2$. Hence, the vibrations of polar bonds such as O–H, N–H, S–H, and C=O are more readily observed in the IR spectrum, while vibrations of less polar bonds are better seen in the Raman spectrum (C≡C, C=C, P=S, S–S, and C–S). Moreover, totally symmetric bond stretching vibrations, which preserve the symmetry of the molecule and produce large polarizability changes, usually dominate the Raman spectra, whereas antisymmetric stretching and deformation modes, which distort the molecule and involve large dipole moment changes, tend to be more intense in IR spectra. This makes Raman spectroscopy more favorable for the study of biological materials, because there is considerably less spectral interference from the deformation modes associated with the H-bond network of water molecules; these are often dominant features in the IR spectra of aqueous samples.[20] The IR spectra of liquid H_2O and D_2O are shown in Figure 3. The Raman spectra of liquid and frozen water (H_2O, D_2O) are shown in Figure 4.

For highly symmetrical molecules and ions such as $TiCl_4$ (T_d), C_6H_6 (D_{6h}), and $PtCl_4^{2-}$ (D_{4h}), both IR and Raman spectroscopies are required to obtain the full set of vibrational frequencies. If a molecule or an ion possesses a center of inversion, there is a *rule of mutual exclusion*; no fundamental vibration that is active in the IR absorption can be active in the Raman scattering, and no fundamental vibration that is active

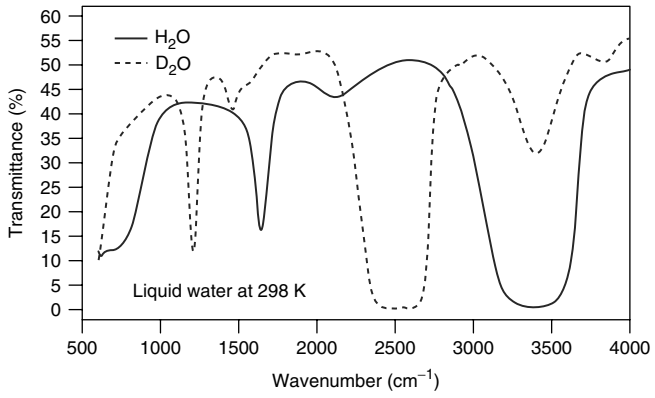

Figure 3 Infrared spectra of neat liquid H_2O (solid line) and D_2O (dashed line)

Encyclopedia of Inorganic and Bioinorganic Chemistry, Online © 2011 John Wiley & Sons, Ltd.

This article was originally published in the *Encyclopedia of Inorganic Chemistry* in 2008 by John Wiley & Sons, Ltd.
DOI: 10.1002/9781119951438.eibc0303

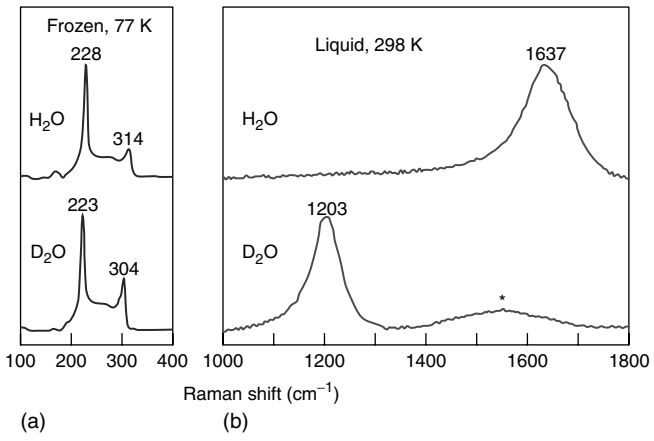

Figure 4 Raman spectra of H_2O and D_2O: (a) as ice at 77 K and (b) as neat liquid at 298 K

in the Raman scattering can be active in the IR absorption. Thus, IR absorption and Raman scattering are complementary and overlapping methods for investigating the vibrations of molecules. Table 1 summarizes the basic aspects of IR and Raman spectroscopy.

2.2 The Raman Effect

The Raman effect – first predicted from theoretical considerations by A. Smekal (1923) and H. A. Kramers and W. Heisenberg (1924) – is a *light scattering* phenomenon with a change of frequency.[23,24] When monochromatic light of frequency ν_0 passes through molecular matter, much of the light continues in its original direction, but a small fraction ($\sim 10^{-3}$) is scattered in other directions (Figure 5). Most of the scattered light emerges at the same frequency as the incident light; this is *elastic* or *Rayleigh scattering*; except for being deflected, the photons neither lose nor gain energy in their collisions with molecules. Rayleigh scattering carries no information about molecular vibrational transitions. A few collisions, however, are *inelastic*. A net transfer of quantized energy ($\Delta E = h\nu_k$) occurs and some scattered light ($\sim 10^{-6}$) obtains new modified frequencies ($\nu_0 \pm \nu_k$). The frequency changes are equal to the frequencies associated with transitions between vibrational (υ_k) or, less frequently, rotational or electronic levels of the system. These two forms of light scattering with change of frequency were first observed by C. V. Raman and K. S. Krishnan in liquids,[25,26] and independently by G. Landsberg and L. Mandelstam in

Table 1 Basic characteristics of infrared (IR) and Raman spectroscopy[a]

Parameter	Infrared spectroscopy	Raman spectroscopy
Spectroscopic phenomenon	Absorption of light: $h\nu_{IR} = \Delta E_{vibr}$	Inelastic scattering of light: $h\nu_{ex} - h\nu_{sc} = \Delta E_{vibr}$
Allowed transition	$\Delta\upsilon = +1, +2, +3, \ldots$	$\Delta\upsilon = \pm1, \pm2, \pm3, \ldots$ (transitions for $\Delta\upsilon = +2, +3, \ldots$, i.e., overtones are considerably less conspicuous than in IR)
Excitation	Polychromatic IR radiation	Monochromatic radiation (ν_{ex}) in the UV, visible, or near IR
Molecular origin	Dipole moment: $\mu = q\boldsymbol{r}$	Induced dipole moment: $\boldsymbol{P} = \alpha\boldsymbol{E}$
Requirement for vibrational activity	Change in dipole moment during vibration: $(\partial\mu/\partial Q_k)0 \neq 0$	Change in polarizability during vibration: $(\partial\alpha/\partial Q_k)0 \neq 0$
Band intensity	$I_{IR}{}^{1/2} \propto (\partial\mu/\partial Q_k)0$	$I_R{}^{1/2} \propto (\partial\alpha/\partial Q_k)_0$
Frequency measurement	Absolute: $\nu_{vibr} = \nu_{IR}$	Relative to the excitation frequency: $\nu_{vibr} = \nu_{ex} - \nu_{sc}$
Readout signal	Comparative: transmittance: $(T = \Phi_s/\Phi_r)$ or absorbance $(A = -\log T)$	Absolute: radiant power or intensity of scattered radiation
Spectral plot	Linear in $\%T$ or logarithmic in A versus wavenumber (cm^{-1})	Linear: Raman intensity versus wavenumber shift (cm^{-1})
Dominant spectral feature	Vibrations destroying molecular symmetry: antisymmetric stretching and deformation modes	Vibrations preserving molecular symmetry: symmetric stretching modes
Inactive molecule	Homonuclear diatomics	None
Centrosymmetric molecule	Only ''u''-symmetry modes active	Only ''g''-symmetry modes active
Medium	Water is a strong absorber and is a poor solvent for IR studies	Water is a weak scatterer and is a good solvent for Raman studies

[a] h, Planck's constant; ΔE_{vibr}, energy difference of vibrational levels; ν, photon frequency; $\Delta\upsilon$, change in vibrational quantum number; q, charge; $\boldsymbol{r}$, charge spacing; α, molecular polarizability; $\boldsymbol{E}$, electric field; Φ_s and Φ_s, radiant powers transmitted by the sample and reference cells, respectively; Q_k, vibrational normal coordinate ($k \leqslant 3N - 6$); ''g'' and ''u'', normal modes of vibration symmetric (*gerade*) and antisymmetric (*ungerade*) with respect to the molecular center of inversion.

Encyclopedia of Inorganic and Bioinorganic Chemistry, Online © 2011 John Wiley & Sons, Ltd.

This article was originally published in the *Encyclopedia of Inorganic Chemistry* in 2008 by John Wiley & Sons, Ltd.
DOI: 10.1002/9781119951438.eibc0303

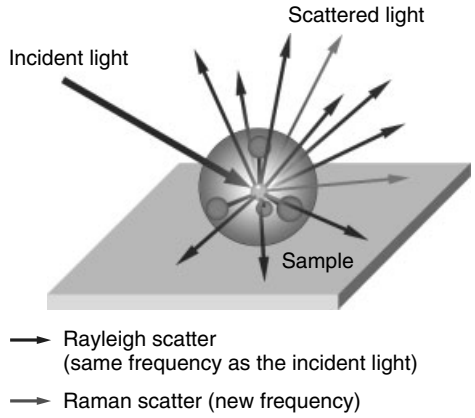

Figure 5 Principle of Rayleigh (elastic) and Raman (inelastic) scattering

quartz[27] in 1928, and are now called *Raman scattering*. C. V. Raman received the Nobel Prize in 1930 for his work on the scattering of light. In 1998, the Raman effect was designated an ACS National Historical Chemical Landmark in recognition of its significance as a tool for analyzing the composition of liquids, gases, and solids. Radiation scattered with a frequency lower than that of the incident light (i.e., $\nu_0 - \nu_k$) is referred to as *Stokes Raman scattering*, while that at the higher frequency (i.e., $\nu_0 + \nu_k$) is called *anti-Stokes Raman scattering*. The magnitude of the frequency shift from the incident radiation provides a measure of the vibrational energy level spacing. In practice, the former spectral region is used for this purpose because the Stokes Raman scattering is *always* more intense than the anti-Stokes Raman at normal temperatures.

The transfer of energy results from the perturbation of the electronic wavefunction of the molecule by the rapidly changing electric field of the photon. The wavefunction of the perturbed system can be expressed as a linear combination of all possible wavefunctions of the unperturbed molecule, with time-dependent coefficients. For a very short time interval ($<10^{-14}$ s), the photon loses identity and becomes indistinguishable from the kinetic and potential energy of the perturbed electrons. Formally, the molecule is regarded as having attained a higher nonstationary energy level (*virtual state*); it returns to a stationary (typically vibrational) state by reemitting (scattering) a photon (Figure 6). If the molecule returns to its original stationary state, the reemitted photon has the same frequency as the incident photon (Rayleigh scattering, $\nu_{sc} = \nu_0$). However, if the final state differs from the initial state by a vibrational quantum ($h\nu_k$), the photon is reemitted with shifted frequencies (Raman scattering, $\nu_{sc} = \nu_0 \pm \nu_k$). At temperatures normally used, a decrease

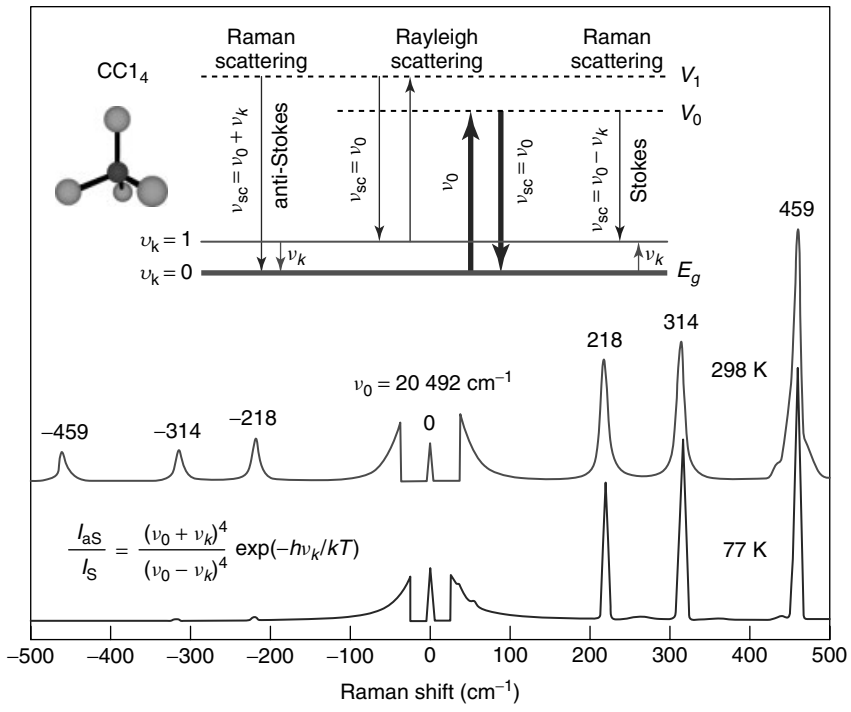

Figure 6 Energy transfer diagram illustrating Rayleigh and Raman scattering (*top*), and Raman spectra for CCl_4 excited at room (298 K) and liquid-N_2 (77 K) temperatures by Ar^+ ion laser radiation of $\lambda_0 = 488.0$ nm or $\nu_0 = 20\,492$ cm^{-1} (*bottom*). The number above the peaks is the Raman shift, $\Delta\tilde{\nu} = \tilde{\nu}_0 - \tilde{\nu}_{sc}$ cm^{-1}. Since the fraction of molecules occupying excited states depends on the Boltzmann factor ($kT = 207$ cm^{-1} at 298 K), the intensities of anti-Stokes bands fall off rapidly with decreasing temperature ($kT = 54$ cm^{-1} at 77 K) and increasing vibrational frequency ν_k

Encyclopedia of Inorganic and Bioinorganic Chemistry, Online © 2011 John Wiley & Sons, Ltd.

This article was originally published in the *Encyclopedia of Inorganic Chemistry* in 2008 by John Wiley & Sons, Ltd.
DOI: 10.1002/9781119951438.eibc0303

in frequency (Stokes emission) is more probable because there are few thermally excited molecules. Although we can speak of a sequence of events in which the emission of a photon from the virtual state follows an absorption process, it is important to appreciate that these processes are actually simultaneous and cannot be separated in time. This means that the Rayleigh and Raman scattering are two-photon processes in which one photon is destroyed and one created at the same time (*induced secondary emission processes*).

The scattered radiation has a spectrum characteristic of the given substance, with an intense band at the incident frequency, ν_0, resulting from Rayleigh scattering, and fainter Raman bands on both sides of ν_0 at distances corresponding to the molecular vibrational frequencies, ν_k. Typical examples of such bands are seen in Figure 6, which displays the Raman spectra obtained on pure carbon tetrachloride, CCl_4, at 298 K (liquid) and 77 K (frozen liquid) upon excitation with an Ar^+ ion laser line at 488.0 nm (20 492 cm^{-1}).[28,29] The measured spectral frequencies are expressed in wavenumber shifts $\Delta\tilde{\nu}$, or *Raman shifts*, which are defined as the *difference in wavenumbers* (cm^{-1}) between the incident and scattered rays, $\Delta\tilde{\nu} = \tilde{\nu}_0 - \tilde{\nu}_{sc}$. Hence, $\Delta\tilde{\nu} = \tilde{\nu}_0 - \tilde{\nu}_0 = 0\,cm^{-1}$ for the Rayleigh peak and $\Delta\tilde{\nu} = \tilde{\nu}_0 - (\tilde{\nu}_0 \pm \tilde{\nu}_k) = \pm\tilde{\nu}_k\,cm^{-1}$ for the Raman peaks. Since Stokes transitions occur at wavenumbers $\tilde{\nu}_0 - \tilde{\nu}_k$, they exhibit *positive* Raman shifts (an *increase* of energy by the scattering system); anti-Stokes transitions occur at $\tilde{\nu}_0 + \tilde{\nu}_k$, and exhibit *negative* Raman shifts (a *decrease* of energy by the scattering system). That is, Stokes bands of CCl_4 are found at 218, 314, and 459 cm^{-1} while their anti-Stokes counterparts occur at -218, -314, and $-459\,cm^{-1}$, regardless of the wavelength of excitation. In general, only the *fundamental* vibrational modes show up in the Raman spectrum because of the much greater probability of transitions involving the two lowest energy vibrational states ($\upsilon_k = 0$, $\upsilon_k' = 1$) of a molecule.

2.3 Requirements for Raman Scattering

In Rayleigh scattering, the sample particles, like molecules, scatter radiation *elastically* by removing radiant energy from the incident beam of (usually) UV–visible photons and instantly reemitting that energy in all directions as the molecules return to their unperturbed forms.[21] Except for undergoing a brief polarization, i.e., momentary distortions on irradiation, the scattering molecules neither gain nor lose energy in their collisions with photons. The Rayleigh light intensity increases with the size of scattering particles; it has a symmetrical and uniform angular distribution, and varies directly with the fourth power of the frequency. For a substance to Rayleigh scatter radiation, it must possess polarizable molecules or aggregates of polarizable molecules with dimensions significantly smaller ($d_m < 0.05\lambda_0$) than the wavelength of the incident radiation (λ_0). (Scattering of radiation by larger particles ($0.05\lambda_0 < d_m < \lambda_0$) is often called *Debye scattering*, while that by still larger particles ($d_m > \lambda_0$) is often termed *Mie scattering*.) Since typical molecular dimensions are on the order of nanometers, the UV–visible photons (~200–680 nm) readily satisfy this criterion and Rayleigh scattering will always be observed in the Raman spectrum, unless it is suppressed with bandpass filters.

The Raman effect differs from Rayleigh scattering in that the molecules scatter part of the incident radiation energy *inelastically* by increasing (Stokes) or decreasing (anti-Stokes) their own (usually) vibrational energy. For a molecular vibration to Raman scatter radiation, it must (i) have a frequency considerably lower than that of the incident radiation and (ii) change the magnitude and/or direction of the *induced electric dipole moment*, or of the molecular polarizability. Excitation (for a spontaneous Raman effect) must be carried out by radiation having a frequency that is well away from any electronic absorption transitions. These criteria are easy to describe physically when we remember that light can be considered as having oscillating electric and magnetic fields and that a molecule has an electron cloud of negatively charged orbitals. *A molecule scatters electromagnetic radiation because it is polarizable*. When a fluctuating electric field $\boldsymbol{E}$ of frequency ν_0 (laser beam) $\gg \nu_k$ (vibrational frequency) strikes a molecule, it sets the electron cloud around heavy and fixed nuclei of the molecule into oscillatory motion. In its distorted form, the molecule is temporarily *polarized*, that is, it undergoes a momentary charge displacement, forming an *induced electric dipole moment* $\boldsymbol{P}$, which oscillates at the frequency, ν_0, of the incoming laser beam. However, if the oscillating dipole induced by light activates (excites) or deactivates (relaxes) a molecular vibration of frequency ν_k, the frequency of the electron cloud oscillation will change correspondingly to $\nu_0 - \nu_k$ or $\nu_0 + \nu_k$. Thus, the polarized molecule becomes an instant source of its own radiation (vibrating electrons emit radiation in all directions) by reemitting excitation energy as light of frequency $\nu_{sc} = \nu_0$ on immediately relaxing to its original stationary energy state (Rayleigh scattering) or at frequencies $\nu_{sc} = \nu_0 \pm \nu_k$ on returning to its stationary states other than the original one (Raman scattering).

The scattered intensity varies directly with the square of the induced dipole moment $\boldsymbol{P} = \alpha\boldsymbol{E}$, where α is the polarizability of the molecule, a volumetric measure of its electron cloud distortion in the path of an incident light, relative to the nuclear framework. The polarizability α is closely related to the structure and bonding properties of the molecule and is *always* nonzero; it increases with decreasing electron density, decreasing bond strength, and increasing bond length. The probability of transition for fundamentals in the Raman spectrum is proportional to the square of the polarizability gradient along the normal coordinate of the vibration, $(\partial\alpha/\partial Q_k)_0$. Accordingly, if there is no net change in polarizability when the vibration occurs, i.e., $(\partial\alpha/\partial Q_k)_0 = 0$, the intensity of a band in the Raman spectrum equals zero and the vibration is said to be Raman inactive. In contrast, the probability of transition of fundamentals in IR absorption

Encyclopedia of Inorganic and Bioinorganic Chemistry, Online © 2011 John Wiley & Sons, Ltd.

This article was originally published in the *Encyclopedia of Inorganic Chemistry* in 2008 by John Wiley & Sons, Ltd.
DOI: 10.1002/9781119951438.eibc0303

is proportional to the square of the dipole moment gradient along the normal coordinate of the vibration, $(\partial\mu/\partial Q_k)_0$. Accordingly, if there is no change in dipole moment when the vibration occurs, i.e., $(\partial\mu/\partial Q_k)_0 = 0$, the intensity of a vibrational band in the IR spectrum equals zero and the vibration is said to be IR inactive.

2.4 Molecular Symmetry and Vibrational Activity

For a molecule that has little or no symmetry, it is usually correct to assume that all its vibrational modes are both IR and Raman active.[20,21] However, when the molecule has considerable symmetry, it is not always easy to picture whether the molecular dipole moment and polarizability will change during the vibration, especially for large and complex molecules. Fortunately, we can easily solve this problem by resorting to simple symmetry selection rules. The molecular vibration is active in IR absorption if it belongs to the same representation as at least one of the dipole moment components (μ_x, μ_y, μ_z) or, since the dipole moment is a vector, as one of the Cartesian coordinates (x, y, z). In contrast, the molecular vibration is active in Raman scattering if it belongs to the same representation as at least one of the polarizability components (α_{xx}, α_{xy}, etc.) or, since the polarizability is a tensor, as one of the binary products of Cartesian coordinates (x^2, xy, etc.) or their linear combinations ($x^2 + y^2$, $x^2 - y^2$, etc.). The symmetry species of the Cartesian coordinates and their binary products are customarily given in the point group *character tables*. IR and Raman activities for vibrational modes of any symmetry species can therefore be simply read off from these tables. Figure 7 is an example of a character table for the point group C_{4v}. It follows from that table that the symmetry species (irreducible representations) $\Gamma(z) = A_1$ and $\Gamma(x, y) = E$, and hence fundamental vibrations of type A_1 and E are *allowed* and of type A_2, B_1, and B_2 are *forbidden* in the IR spectrum for any molecule that belongs to the C_{4v} point group. The vibrations of type A_2 are also *forbidden* in the Raman spectrum of C_{4v} molecules but those of type A_1, B_1, B_2, and E are all Raman *allowed* because $\Gamma(x^2 + y^2, x^2) = A_1$, $\Gamma(x^2 - y^2) = B_1$, $\Gamma(xy) = B_2$, and $\Gamma(xz, yz) = E$ in C_{4v} point group.

2.5 Depolarization Ratios and Symmetry of Vibrations

Useful information on the scattering process and on the symmetry of the vibration involved can be obtained by measuring the depolarization ratio, ρ, of a Raman band.[1,21,24,30] The incident and scattered photons in Raman scattering both involve a polarization (plane in which the radiation vibrates), and the polarization of the scattered light is related to but not necessarily the same as that of the incident light, even if the sample molecules are randomly oriented. If the incident radiation is linearly (or plane) polarized, as it is with a laser source, the Raman scattered light can be polarized to various degrees that depend on the nature of the active vibration. The depolarization ratio is given by $\rho = I_\perp/I_\parallel$, where $I_\perp$ and $I_\parallel$ are the intensities of Raman light that is linearly polarized perpendicular and parallel, respectively, to the polarization of the excitation radiation. Experimentally, it is obtained by inserting a polarization analyzer between the sample and the monochromator, which upon rotation by 90° passes $I_\perp$ or $I_\parallel$ (Figure 8). For totally symmetric vibrations, which by nature do preserve molecular symmetry during the motion of the nuclei, the incident beam polarization is largely maintained in the scattered light leading to small ρ values ($0 \leqslant \rho < 3/4$,

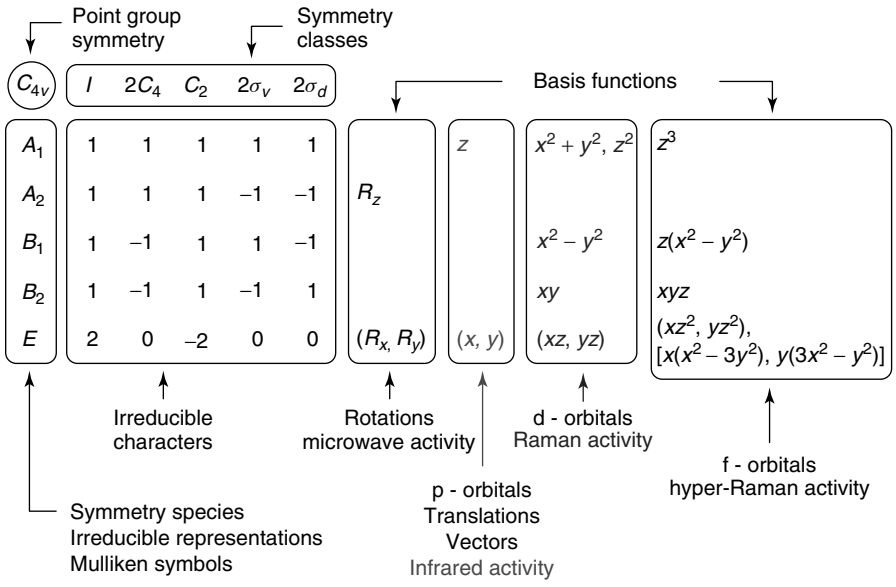

Figure 7 The structure of the character table for the symmetry point group C_{4v}

Encyclopedia of Inorganic and Bioinorganic Chemistry, Online © 2011 John Wiley & Sons, Ltd.

This article was originally published in the *Encyclopedia of Inorganic Chemistry* in 2008 by John Wiley & Sons, Ltd.
DOI: 10.1002/9781119951438.eibc0303

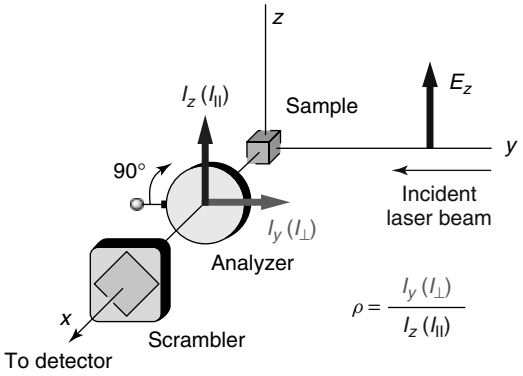

Figure 8 Schematic layout of a typical 90° Raman depolarization experiment showing the positions of the polarization analyzer and the scrambler. The analyzer may simply be a polaroid sheet, which can be rotated by 90° to allow the parallel (‖) and perpendicular (⊥) components of the scattered light to pass through to the detector. The function of a scrambler is to change linear into circular polarization of the light entering the Raman spectrometer slit in order to avoid measurement errors due to the variable spectrometer transmittance of the light polarized in different directions

polarized Raman bands). The higher the symmetry of a molecule, the closer to zero is the value of ρ. It should also be pointed out that the polarized bands are (usually) the strongest features in the Raman spectrum. On the other hand, if the vibrational motion distorts the symmetry (nontotally symmetric vibrations), a significant depolarization can occur producing depolarized Raman bands. From scattering theory, it is predicted that for such vibrations $\rho = 3/4$. In the Raman spectrum of CCl_4, shown in Figure 9, the dominant band at 459 cm^{-1} loses nearly all intensity in the perpendicular scattering ($\rho = 0.006$) and a number of weaker bands at 217, 314, 759, and 788 cm^{-1} are only slightly weakened ($\rho = 0.75$). The band at 459 cm^{-1} is therefore immediately assignable to a totally symmetric vibration of the molecule and the ones at 217, 314, 759, and 788 cm^{-1} cannot arise from totally symmetric modes.

Under resonance or near-resonance excitation conditions, however, certain nontotally symmetric modes can also give rise to anomalously ($\rho > 3/4$) or even inversely ($\rho = \infty$) polarized Raman bands.[9] Figure 10 depicts RR spectra of nickel(II) porphine (NiP) and indeed the strongest bands show exactly the opposite of what is observed for CCl_4 (Figure 9), i.e., the perpendicular scattered radiation (⊥) is dramatically more intense than that with parallel radiation (‖). NiP has a D_{4h} symmetry and these bands arise from the A_{2g} vibrational modes that have rotational symmetry themselves ($\Gamma(R_z) = A_{2g}$ in D_{4h} point group). Modes of this type are normally Raman forbidden, but can be activated under certain resonant excitations in the RR spectrum by vibronic mixing of excited electronic states (*vide infra*). Table 2 summarizes the ranges of values expected for the depolarization ratio for bands arising from modes of various symmetries in the off-resonance and RR spectra.[1,30]

The depolarization ratio in Raman scattering has no true counterpart in IR absorption. However, the dipole moment is

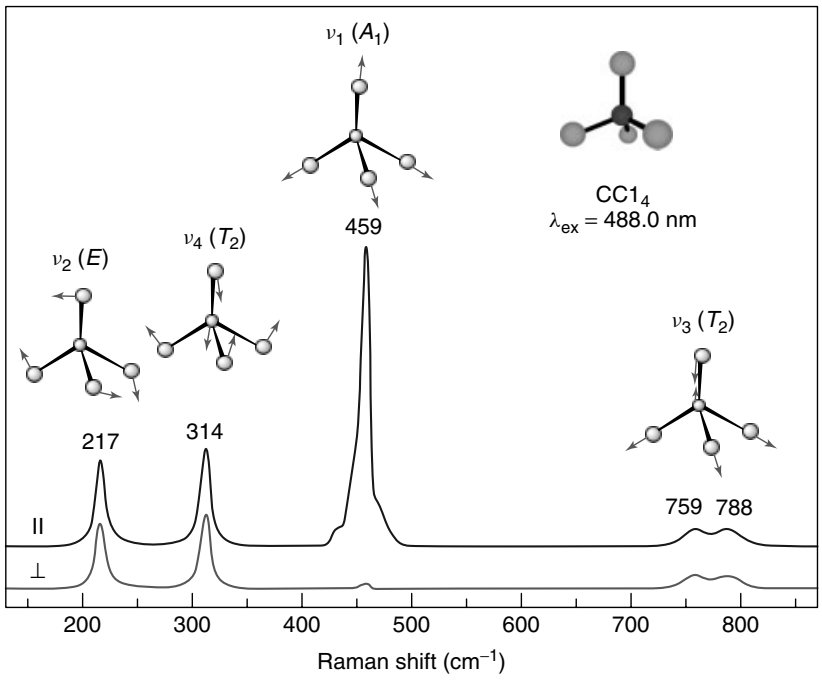

Figure 9 Parallel (‖) and perpendicular (⊥) scattered Raman spectra from liquid CCl_4 showing the polarized (ν_1) and depolarized (ν_2, ν_3, and ν_4) bands associated with totally symmetric (A_1) and nontotally symmetric (E, T_2) vibrations, respectively

Encyclopedia of Inorganic and Bioinorganic Chemistry, Online © 2011 John Wiley & Sons, Ltd.

This article was originally published in the *Encyclopedia of Inorganic Chemistry* in 2008 by John Wiley & Sons, Ltd.
DOI: 10.1002/9781119951438.eibc0303

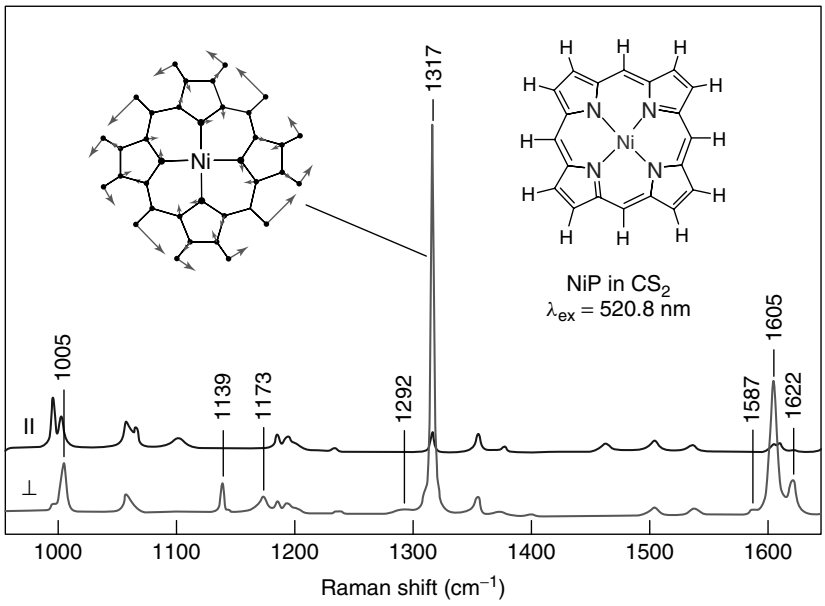

Figure 10 Parallel (∥) and perpendicular (⊥) scattered resonance Raman spectra from NiP in CS_2 showing the anomalously polarized bands (labeled) associated with the ring A_{2g} vibrations

Table 2 Values of depolarization ratio for vibrational Raman bands observed in normal Raman and resonance Raman spectra

Type of Raman scattering	Vibrational band character	Polarizability tensor symmetry	Depolarization ratio
Off-resonance (all cases) and resonance (most cases)	Polarized (totally symmetric modes)	Symmetric, $\alpha_{\rho\sigma} = \alpha_{\sigma\rho}$	$0 < \rho < 3/4$
	Depolarized (nontotally symmetric modes)	Symmetric, $\alpha_{\rho\sigma} = \alpha_{\sigma\rho}$	$\rho = 3/4$
Resonance (special cases)	Anomalously polarized (nontotally symmetric modes, normally Raman forbidden)	Nonsymmetric, $\alpha_{\rho\sigma} \neq \alpha_{\sigma\rho}$	$\rho > 3/4$
	Inversely polarized (nontotally symmetric modes, normally Raman forbidden)	Antisymmetric, $\alpha_{\rho\sigma} = -\alpha_{\sigma\rho}$	$\rho = \infty$

a vector quantity, and the absorption of IR light depends on the relative orientation of the molecule and the photon electric vector. If all the molecules are aligned, as in a crystal or a stretched film, and the photon vector points along a molecular axis, e.g., z, then absorption occurs for those vibrations that displace the dipole along z. Vibrations that are purely x or y polarized would be absent. Thus, extra information about the character of the vibration is available from IR absorption spectra for oriented samples.

2.6 Enhancement of Raman Scattering

The intensity of Raman scattering depends strongly on the excitation frequency.[21,22] Figure 11 illustrates what happens if, for a given molecular system, we change excitation frequency so that it moves from the transparent region (a) to the vicinity of an allowed electronic absorption band (b)–(e). As discussed before, excitation in the transparent region of a scattering system leads to a normal (or off-resonance) Raman effect. Under this circumstance, the intensity of Raman bands is described by a ν^4 law (Figure 2), and some advantage can be taken of this dependence by using the higher frequency irradiation (e.g., the blue and green lines of the argon laser, rather than the red line of the helium–neon laser). However, when the frequency of the exciting laser line is close to (preresonance) or equal to (resonance) the frequency of an allowed electronic absorption of a molecule, as in (b) and (c), the intensities of certain Raman bands are greatly increased (up to 10^6-fold) above their off-resonance values. This happens because the polarizability, and its dependence on the molecular motions, is enhanced via the electronic transition. Not all Raman bands intensify,

Encyclopedia of Inorganic and Bioinorganic Chemistry, Online © 2011 John Wiley & Sons, Ltd.

This article was originally published in the *Encyclopedia of Inorganic Chemistry* in 2008 by John Wiley & Sons, Ltd.
DOI: 10.1002/9781119951438.eibc0303

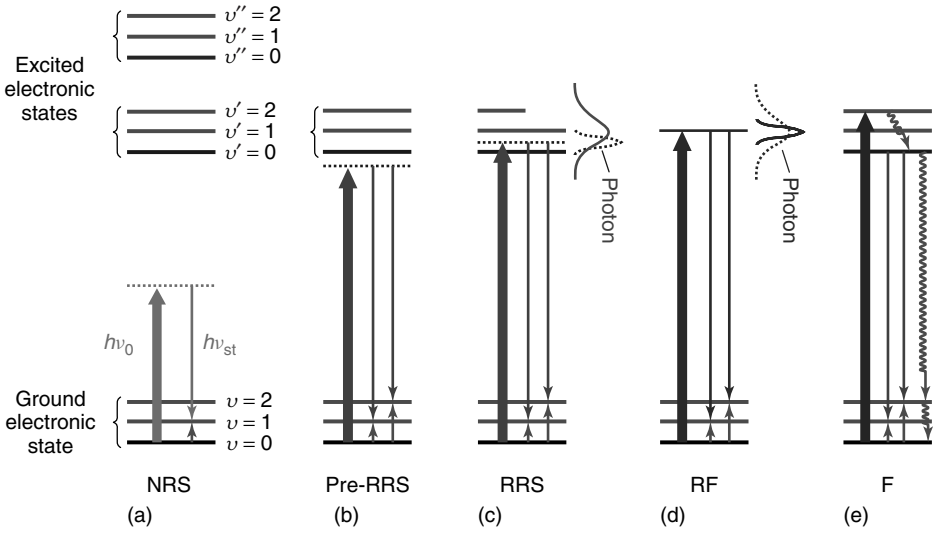

Figure 11 Diagram of Stokes transitions ($h\nu_{St}$) of Raman scattering (a)–(c) and fluorescent emission (d), (e) as a function of excitation energy ($h\nu_0$). (a) Normal Raman scattering occurs upon excitation in the transparent region of the molecule. The molecular polarizability creates a nonstationary (virtual) state to interact with $h\nu_0$, which does not resemble any particular molecular state. Many excited electronic states contribute to this state and the scattering process is nonselective in that all vibrations (usually fundamental) that can change the polarizability may be observed. (b) Preresonance Raman scattering in which $h\nu_0$ approaches the energy of an electronic transition. The interacting state is then dominated by this electronic state, which produces some enhancement of Raman scattering (10–100-fold) and possible appearance of overtones. (c) Resonance Raman scattering, in which the interacting state is dominated by a few vibronic levels in the interior of the excited electronic state. Many Raman bands are then attenuated by the absorption, but those associated with normal coordinates that can carry the molecule into its excited-state geometry may be greatly enhanced (10^3–10^6 times). (d) Resonance fluorescence occurs when $h\nu_0$ coincides with a single sharp level of the electronic manifold (small molecules in gas phase). The distinction between RRS and RF is that the RF involves actual population of the upper state (its width is smaller than that of the $h\nu_0$ pulse), the emission decaying with the excited-state lifetime, whereas RRS process is simultaneous (actually $<10^{-14}$ s) with the excitation pulse. If not in exact resonance with the upper state, only RR scattering occurs. (e) Relaxed fluorescence, in which radiational relaxation to the ground state is preceded by prior radiationless relaxation to the lowest vibrational level of the excited electronic state. This produces a red-shifted broad envelope of emission on the 10^{-6}–10^{-8} timescale

however, but only those due to vibrational transitions that couple with the electronic transition. This is illustrated in Figure 12 which shows a dramatic increase in intensity of the Cu–S(Cys) vibrational modes near 400 cm^{-1} as the excitation wavelength (647.1 nm) approaches that of the (Cys)S → Cu(II) CT electronic transition (~600 nm) in the blue copper protein, azurin (*see* ***Copper Proteins with Type 1 Sites***).[16] Another example of RR scattering was seen in Figure 10, where stretching modes of the porphyrin π bonds are enhanced because of their coupling with the $\pi-\pi^*$ resonant transitions of NiP.[31–33] Thus, the correct identification of the vibrational modes showing RR enhancement will aid in the assignment of the resonant electronic transition and vice versa.

The laser frequency is an important consideration in Raman applications because resonance enhancement greatly increases both the sensitivity and the selectivity of the technique. Nonresonance Raman scattering is weak enough that sample concentrations in the molar range are often required to obtain good quality spectra, but resonance enhancement can lower the required concentration to the millimolar to micromolar ranges. Selectivity is an equally important feature since vibrational spectroscopy frequently suffers from crowding and overlap of bands when complex molecules or mixtures are investigated. Since only Raman modes associated with the excited-state distortion are enhanced, the RR spectrum is simplified and one can be sure that the enhanced bands are associated with the chromophore; interferences from other parts of the molecule or other constituents of the mixture are eliminated. Of course, this selectivity means a loss of information if the nonchromophoric parts of the sample are of interest. Wide tunability of the laser source is desirable so that different chromophores in the sample (or different excited states of the same chromophore, which may enhance different Raman bands) can be accessed. The main differences between Raman and RR scattering are summarized in Table 3.

2.7 Electronic Structure and RR Scattering Mechanisms

The vibronic theory of the RR effect distinguishes two major intensity enhancement mechanisms that play a dominant role in the RR spectra: (i) *Franck–Condon* (*FC*) *principle* and (ii) *Herzberg–Teller* (*HT*) *vibronic coupling*, which have quite different properties.[21,33–35] The FC scattering mechanism involves displacement of the potential minima of the ground and excited electronic states along a vibrational normal

Encyclopedia of Inorganic and Bioinorganic Chemistry, Online © 2011 John Wiley & Sons, Ltd.

This article was originally published in the *Encyclopedia of Inorganic Chemistry* in 2008 by John Wiley & Sons, Ltd.
DOI: 10.1002/9781119951438.eibc0303

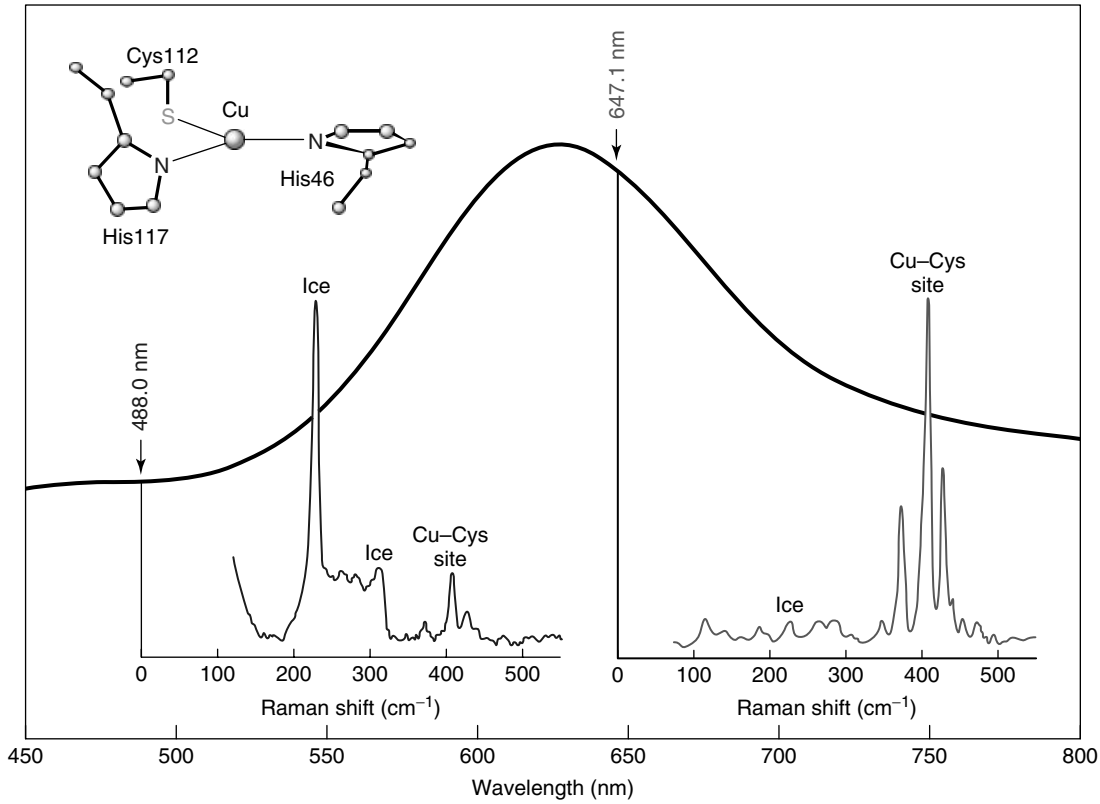

Figure 12 Vibrational enhancement selectivity available from resonance Raman spectroscopy. The UV–visible spectrum of a *P. aeruginosa* azurin is shown together with two different Raman spectra (frozen solution at 77 K) that derive from laser excitation within the S(Cys) → Cu(II) charge-transfer absorption band at 625 nm (647.1 nm) and away from the absorption (488.0 nm). Excitation within resonance leads to dramatically increased Raman scattering from the Cu active site, whereas off-resonance excitation produces a spectrum dominated by bands of nonchromophoric ice

Table 3 Main differences between Raman and resonance Raman scattering

Raman scattering	Resonance Raman scattering
B-term effective (any Raman allowed mode)	A-term (totally symmetric modes), B-term (nontotally symmetric modes), and C-term (first overtones and binary combinations of vibronically active modes) effective
Polarized (p) and depolarized (dp) bands only	Anomalously polarized (ap) and inversely polarized (ip) bands attainable as well
Overtones and combination bands very weak and seldom observable	Overtones and combination bands common
More vibrations observed in the spectrum	Some vibrations selectively enhanced
No electronic information	Electronic information present
Inherently weak scattering ($10^6 - 10^9$ times weaker than Rayleigh scattering)	Much stronger scattering ($10^3 - 10^6$ times greater than normal Raman scattering)
Intensity arises from the dependence of the ground-state polarizability on molecular vibrations only	Ground-state polarizability and its dependence on molecular vibrations is enhanced via electronic transition(s)

coordinate, whereas the HT scattering mechanism involves a transfer of the transition moment between different excited electronic states induced by a vibrational excitation. This means that by moving into the resonance region, the vibrational modes that reflect the change in geometry when converting the molecule from its ground to excited state (FC allowed) or those that are able to vibronically couple the resonant excited state to some other electronic state with different transition moments (HT allowed) will be strongly enhanced. In general, the former effect is most pronounced for *totally symmetric modes* and *allowed resonant electronic transitions*, whereas the latter is pronounced for *nontotally symmetric modes* and

Encyclopedia of Inorganic and Bioinorganic Chemistry, Online © 2011 John Wiley & Sons, Ltd.

This article was originally published in the *Encyclopedia of Inorganic Chemistry* in 2008 by John Wiley & Sons, Ltd.
DOI: 10.1002/9781119951438.eibc0303

weakly allowed or forbidden resonant electronic transitions. This selective enhancement is one of the most important and valuable aspects of RR spectroscopy, since it leads to a considerable simplification of the observed spectra; the RR spectra consist primarily of bands arising from either totally or nontotally symmetric vibrations depending upon the nature of the resonant electronic transitions.

To determine the scattered radiation spectrum of an oscillating molecule under conditions of resonance excitation, we must consider how the polarizability α varies not only with normal modes of vibration but also with frequency of the incident radiation that excites them. For a molecule in a molecular state $|g\rangle$ (initial) perturbed by the electromagnetic wave of frequency ν_0 so that it passes into a molecular state $|f\rangle$ (final) while scattering light of frequency $\nu_0 \pm \nu_k$ ($\nu_k = \nu_f - \nu_g$), the matrix elements of α for the vibrational transition k, $[\alpha_{\rho\sigma}]_k$, are given by the Kramers–Heisenberg–Dirac (KHD) dispersion equation[36,37]:

$$[\alpha_{\rho\sigma}]_k = \frac{1}{h}\sum_e \left(\frac{\langle f|M_\rho|e\rangle\langle e|M_\sigma|g\rangle}{\nu_{eg} - \nu_0 + i\Gamma_e} + \frac{\langle f|M_\sigma|e\rangle\langle e|M_\rho|g\rangle}{\nu_{eg} + \nu_0 + i\Gamma_e} \right) \quad (1)$$

where ρ, $\sigma = x, y, z$, which independently refer to the molecule-fixed nonrotating Cartesian coordinate system and represent the polarizations of the incident (σ) and scattered light (ρ), $|g\rangle$ and $|f\rangle$ are the initial and final states of the molecule, and the summation is over all the excited electronic states $|e\rangle$. The integrals $\langle f|M_\sigma|e\rangle$ and $\langle e|M_\rho|g\rangle$ are the electric dipole transition moments along the ρ and σ directions; M is the electron position operator; $h\nu_0$ is the energy of the incident radiation; and Γ_e is a damping factor (which prevents the denominator at resonance from reaching zero), reflecting the finite natural lifetime and sharpness of the excited state, $|e\rangle$.

Far from resonance ($\nu_0 \ll \nu_{eg}$), the magnitude of $[\alpha_{\rho\sigma}]_k$ is independent of ν_0; the number of excited electronic states contributing to the polarizability is large. In this case, all the energy denominators in the KHD equation become large and the scattering tensor $[\alpha_{\rho\sigma}]_k$ correspondingly small, leading to very weak scattering (normal Raman or Raman scattering). As the excitation frequency, ν_0, is tuned to the frequency of an electronic transition, ν_{eg}, the first (resonance) term of the KHD equation will become dominant and large because $\nu_{eg} - \nu_0 \approx 0$ in its denominator, and the second (nonresonance) term will become negligible. As a result, the scattered intensity is expected to increase drastically (but not to infinity owing to the Γ_e term) when ν_0 is in resonance region, provided the resonant state $|e\rangle$ has a large enough transition dipole moment from the ground state. The summation over all the electronic states can be relaxed except for the electronic state in resonance, and by applying (following Albrecht[36]) the adiabatic Born–Oppenheimer approximation of separability of electronic and vibrational wavefunctions for $|g\rangle$, $|e\rangle$, and $|f\rangle$ states, the KHD equation can be rewritten as

$$[\alpha_{\rho\sigma}]_k = \frac{1}{h}\sum_\upsilon \frac{\langle j|(\mu_\rho)_e|\upsilon\rangle\langle\upsilon|(\mu_\sigma)_e|i\rangle}{\nu_{\upsilon i} - \nu_0 + i\Gamma_\upsilon} \quad (2)$$

where $(\mu_\rho)_e = \langle g|(\mu_\rho)_e|e\rangle$ and $(\mu_\sigma)_e = \langle e|(\mu_\sigma)_e|g\rangle$ are the pure electronic transition moments, along ρ and σ directions, for the resonant excited state e; of which υ is a particular vibrational level of bandwidth Γ_υ; $\nu_{\upsilon i}$ is the transition frequency from the ground vibrational level i to the level υ; $|i\rangle$, $|j\rangle$, and $|\upsilon\rangle$ represent vibrational states of a given normal coordinate, Q_k; and the summation is over all excited-state vibrational levels, υ. The dependence of $(\mu_{\rho,\sigma})_e$ on Q_k is small if the Born–Oppenheimer approximation is valid and therefore it can be expanded as a Taylor series:

$$\mu_e = \mu_e^0 + \sum_k \mu_e' Q_k + \ldots \quad (3)$$

where $\mu_e' = (\partial\mu_e/\partial Q_k)_0$. (In writing equation (3), we have dropped the polarization subscripts.) When the electronic resonant transition is weakly allowed, μ_e' can be of the same magnitude as μ_e^0, or even exceed it, if the excited-state $|e\rangle$ can gain absorption strength from other excited states by vibronic mixing via the coordinate Q_k (called *vibronic coupling*). In the HT formalism for the vibronic coupling,[36–38]

$$\mu_e' = \mu_s^0 \frac{\langle s|(\partial H_e/\partial Q_k)_0|e\rangle}{\nu_s - \nu_e} \quad (4)$$

where $|s\rangle$ is another excited state that can be mixed in to $|e\rangle$ by Q_k; ν_s and μ_s are the frequency and transition dipole moment of the mixing electronic state, $|s\rangle$; and $(\partial H_e/\partial Q_k)_0$ is the vibronic coupling operator that connects two excited states $|e\rangle$ and $|s\rangle$, with H_e being the Hamiltonian for the total electronic energy of the molecule. Thus, the stronger the transition to the state $|s\rangle$, and the closer it is in energy to $|e\rangle$, the larger the μ_e' will be.

Substitution of equations (4) and (3) into equation (2) yields an expression with many terms, of which the first three terms, called *A-*, *B-*, *and C-terms*, are the dominant mechanisms in RR scattering.

$$[\alpha]_k = \mathbf{A} + \mathbf{B} + \mathbf{C} + \cdots \quad (5)$$

where

$$\mathbf{A} = (\mu_e^0)^2 h^{-1} \sum_\upsilon \frac{\langle j|\upsilon\rangle\langle\upsilon|i\rangle}{\nu_{\upsilon i} - \nu_0 + i\Gamma_\upsilon} \quad (6)$$

$$\mathbf{B} = \mu_e^0 \mu_e' h^{-1} \sum_\upsilon \frac{\langle j|Q_k|\upsilon\rangle\langle\upsilon|i\rangle + \langle j|\upsilon\rangle\langle\upsilon|Q_k|i\rangle}{\nu_{\upsilon i} - \nu_0 + i\Gamma_\upsilon} \quad (7)$$

$$\mathbf{C} = (\mu_e')^2 h^{-1} \sum_\upsilon \frac{\langle j|Q_k|\upsilon\rangle\langle\upsilon|Q_k|i\rangle}{\nu_{\upsilon i} - \nu_0 + i\Gamma_\upsilon} \quad (8)$$

Each term of equations (6)–(8) is factorized into parts that can be related to the electronic and vibrational wavefunctions and excitation frequency. The electronic contribution (matrix elements of μ_e^0 and μ_e'), weighted with the differential energy denominators ($\nu_{\upsilon i} - \nu_0 + i\Gamma_\upsilon$), determines the *total* enhancement of all the normal vibrations for a given

Encyclopedia of Inorganic and Bioinorganic Chemistry, Online © 2011 John Wiley & Sons, Ltd.

This article was originally published in the *Encyclopedia of Inorganic Chemistry* in 2008 by John Wiley & Sons, Ltd.
DOI: 10.1002/9781119951438.eibc0303

electronic transition and a given ν_0. Since μ_e^0 and μ_e' in $[\alpha]_k$ also determine the optical absorption spectrum, structural information often emerges from the interpretation of both the RR and UV–visible spectra. The vibrational part described by FC factors and $(\partial H_e/\partial Q_k)_0$ (vibronic coupling operator) governs the intensity distribution among the enhanced modes, and is therefore responsible for the selectivity of the vibrational mode enhancement, the enhanced modes containing information about the vibronic nature of the electronic transitions as well as the molecular distortion and dynamics at the electronic excited state(s).

2.7.1 *A-term RR Scattering*

The A-term is the leading RR scattering mechanism encountered in practice and involves vibrational interactions with a single excited electronic state, $|e\rangle$, by way of FC overlap integrals, $\langle j|\upsilon\rangle$ and $\langle\upsilon|i\rangle$ (FC scattering), as illustrated in Figure 13. This term is nonzero only if $\mu_e^0 > 0$ and $\langle\upsilon|i\rangle\langle j|\upsilon\rangle \neq 0$. Consequently, the A-term is most pronounced for strongly allowed electronic transitions, with large values of $(\mu_e)^2$ and substantial nonorthogonalities of the FC factors $\langle\upsilon|i\rangle$ and $\langle j|\upsilon\rangle$ upon electronic excitation, such as electric-dipole-allowed $\sigma-\sigma^*$, $\pi-\pi^*$, and CT transitions. Excitations into weak electronic transitions, such as forbidden $\pi-\pi^*$, ligand field d–d, and spin forbidden transitions, will not produce significant FC scattering.[16,21,22] The relative enhancements for different vibrational modes are determined by the values of the FC factors, which are nonzero, and may become large if there is a substantial shift of the excited-state potential, Δ_k^e, along the vibrational coordinate Q_k. Only totally symmetric modes are subject to A-term enhancement, because they can satisfy the latter condition ($\Delta_k^e \neq 0$) by symmetry. Frequently, Δ_k^e in the excited electronic state is large enough to give appreciable magnitudes of $\langle\upsilon|i\rangle\langle j|\upsilon\rangle$ products for up to several quanta of vibrational energy. Intense overtone progression $n_k\nu_k$ of totally symmetric modes ν_k can then be observed in the RR spectrum, making it possible to determine their harmonic frequencies and anharmonicity constants. Clark and coworkers have carried out extensive work in this area on coordination compounds.[1,39] The longest progressions observed thus far

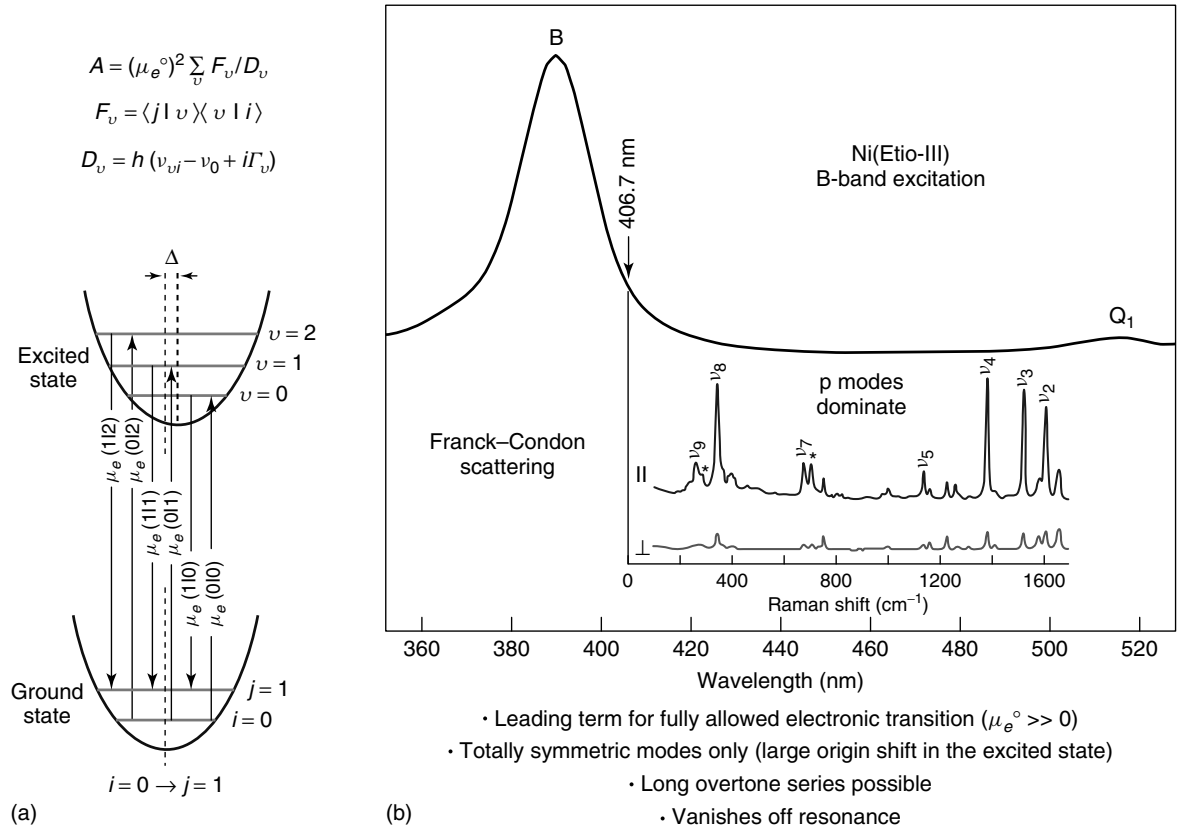

Figure 13 (a) Diagrammatic representation of Raman process responsible for A-term resonance scattering. The applicable electronic transition moment and vibrational overlap integral is indicated for each contributing transitions for $\upsilon = 0$, 1, and 2 intermediate levels of the resonant excited state. (b) Soret electronic transition excitation and Franck–Condon (A-term) scattering in metalloporphyrins. Soret absorption band (B) is shown for Ni(Etio-III) together with the RR spectra in parallel (‖) and perpendicular (⊥) scattering excited at 406.7 nm. Resonance with the Soret absorption band enhances mainly polarized bands (p), arising from totally symmetric modes, A_{1g}. The asterisks indicate solvent bands (CH_2Cl_2)

Encyclopedia of Inorganic and Bioinorganic Chemistry, Online © 2011 John Wiley & Sons, Ltd.

This article was originally published in the *Encyclopedia of Inorganic Chemistry* in 2008 by John Wiley & Sons, Ltd.
DOI: 10.1002/9781119951438.eibc0303

are for the diatomic I_2 (up to $n_1 = 25$), the linear-chain $([Pt(tn)_2][Pt(tn)_2Br_2])^{4-}$ (up to $n_1 = 18$), tetrahedral SnI_4 (up to $n_1 = 15$), and μ-oxo-bridged $[Ru_2OCl_{10}]^{4-}$ (up to $n_2 = 12$) for which the respective $\nu_2 < 400\,cm^{-1}$.[1,39]

2.7.2 *B-term RR Scattering*

The B-term scattering arises from the vibronic coupling of the resonant state, $|e\rangle$, to another excited state, $|s\rangle$ (HT scattering). Since the magnitude of μ_e' increases with the oscillator strength of μ_s and decreasing frequency separation between the $|e\rangle$ and $|s\rangle$ states, the B-term scattering is most pronounced when the exciting frequency is tuned to a weakly allowed electronic transition that is mixed vibronically with a nearby strong one ($\mu' e > \mu_e^0$ under this circumstance). The B-term denominator is the same as for the A-term, but its numerator contains the Q_k-dependent vibrational overlap integrals $\langle \upsilon | Q_k | i \rangle$ and $\langle j | Q_k | \upsilon \rangle$. These integrals connect ground- and excited-state vibrational levels that differ by one quantum (Figure 14). When they are multiplied by FC factors $\langle j | \upsilon \rangle$ or $\langle \upsilon | i \rangle$, having the same quantum numbers in the ground and excited states (e.g., $\langle 1|1\rangle$ and $\langle 0|0\rangle$) , the numerator does not vanish even if there is no excited-state shift of the potential upon electronic excitation. Thus, B-term scattering is exhibited only by fundamental vibrational modes and the vibrations enhanced may have any symmetry that is contained in the direct product of the two electronic transition representations, $(\Gamma|e\rangle \times \Gamma|s\rangle)$. The relative enhancement factors for different mode symmetries depend on the effectiveness of the vibration in coupling the excited states $|e\rangle$ and $|s\rangle$. Consequently, B-term scattering provides a primary mechanism for RR activity of nontotally symmetric modes, which can be, and usually are, enhanced. The more efficient the vibronic coupling of the two excited electronic states, the more effective B-term enhancement can be observed. Moreover, under nonresonance

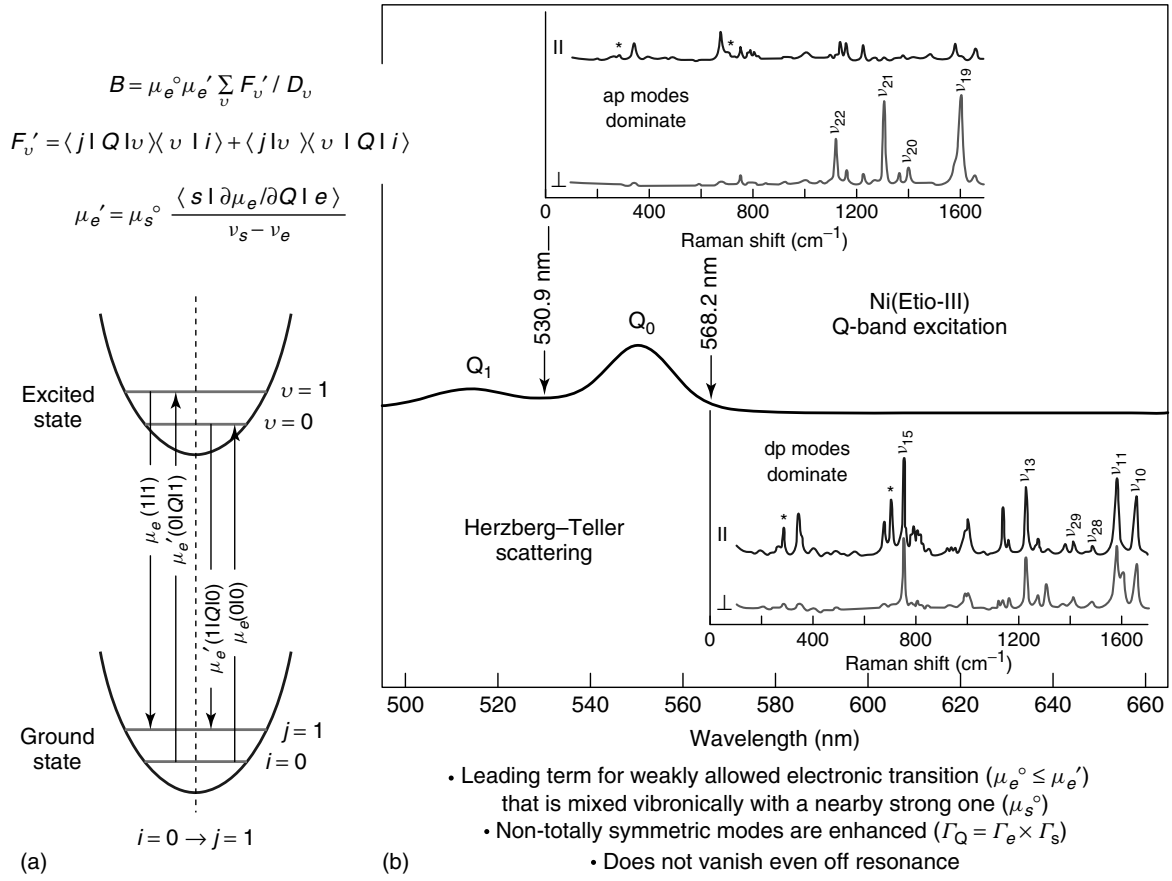

Figure 14 (Left) Diagrammatic representation of Raman process responsible for B-term resonance scattering. The applicable electronic transition moment and vibrational overlap integral is indicated for each contributing transition for $\upsilon = 0$, 1, and 2 intermediate levels of the resonant excited state. (Right) Q-electronic transition excitation and Herzberg–Teller (B-term) scattering in metalloporphyrins. Q absorption band (Q_0 and Q_1) are shown for NiEtio-III together with the RR spectra in parallel (‖) and perpendicular (⊥) scattering excited at 530.9 (top) and 568.2 nm (bottom). Resonance in the Q-band region enhances depolarized (B_{1g}, B_{2g}) and anomalously polarized (A_{2g}) modes that are effective in vibronic mixing of the Q and Soret electronic transitions. Owing to interference effects, the A_{2g} modes are brought out most strongly via excitation between Q_0 and Q_1 (530.9 nm), while the B_{1g} and B_{2g} modes are brought out more strongly with excitation outside the Q bands (568.2 nm). The asterisks indicate solvent bands (CH_2Cl_2)

Encyclopedia of Inorganic and Bioinorganic Chemistry, Online © 2011 John Wiley & Sons, Ltd.

This article was originally published in the *Encyclopedia of Inorganic Chemistry* in 2008 by John Wiley & Sons, Ltd.
DOI: 10.1002/9781119951438.eibc0303

conditions, when the energy denominator $(\upsilon_{\upsilon i} - \upsilon_0 + i\Gamma_\upsilon)$ can be factored out, the sum over all excited states in the numerator of equation (7) reduces to $\langle j|Q_k|i\rangle$, which is nonzero for $j = i + 1$, i.e., fundamental modes. Thus, off-resonance Raman scattering is preserved by the B-term (although under these conditions any specific resonance effects are lost in the sum over all excited states of equation (7)).

2.7.3 A- and B-term RR Scattering Illustrated

RR scattering by heme proteins and metalloporphyrins (*see* ***Iron Porphyrin Chemistry***-)[14,31–33] provides a classical example of the differential A- and B-term vibrational enhancement pattern, as shown in Figures 13 and 14 for nickel(II) etioporphyrin-III, Ni(Etio-III),[40] which occurs naturally in crude oils and marine sediments. The electronic absorption spectrum of Ni(Etio-III) is due to two allowed in-plane $\pi-\pi^*$ transitions, $a_{1u} \rightarrow e_g{}^*$ and $a_{2u} \rightarrow e_g{}^*$, which have the same $a_{1u} \times e_g = a_{2u} \times e_g = E_u$ symmetry in the idealized D_{4h} point group of the porphyrin chromophore.[40,41] The in-phase mixing of these $\pi-\pi^*$ transitions gives rise to very intense absorption in the violet region at 391 nm, known as the *B or Soret band* (Figure 13), whereas their out-of-phase combination produces much weaker absorption in the yellow region at 551 nm, known as the Q_0 *or* α *band* (Figure 14). There is also a composite side band in the green region at 515 nm that results from vibronic coupling between the Q_0 and B transitions, referred to as the Q_1 *or* β *band*. As expected, laser irradiation of Ni(Etio-III) near the Soret absorption band (406.7-nm excitation, Figure 13) leads to RR spectra that are dominated by the polarized peaks (p, $\rho = I_\perp/I_\parallel \approx 1/8$) arising from the totally symmetric vibrations of the porphyrin skeleton, A_{1g}.[40] This dominance reflects that only totally symmetric vibrations, that is, those capable of shifting the excited-state potential surface, are subject to the FC (A-term) enhancement mechanism for allowed electronic transitions (equation 6). Porphyrin structure-sensitive modes ν_2, ν_3, ν_4, and ν_8 are especially strong, indicating large geometric displacements in the excited state along these vibrational coordinates.

Laser irradiation of Ni(Etio-III) near the α (568.2-nm excitation) and β bands (530.9-nm excitation) also produces strong resonance enhancement, as shown in Figure 14. In contrast to Soret-band excitation, it is the depolarized (dp, $\rho \approx 3/4$) and anomalously polarized (ap, $\rho \gg 3/4$) Raman peaks from the nontotally symmetric vibrations that are dominant.[40] These vibrations derive their intensity from the B-term (HT scattering) involving a vibronic coupling of the two excited states of the α and Soret electronic transitions (which is also responsible for the β absorption side band). Since both the Soret and α excited states are of E_u symmetry, the allowed symmetries of the mixing vibrations are $E_u \times E_u = A_{1g} + A_{2g} + B_{1g} + B_{2g}$. The A_{1g} modes are, however, not efficient in vibronic coupling. The B_{1g} and B_{2g} modes both give depolarized bands, while the A_{2g} modes give anomalously polarized bands. The Q-band resonance is also subject to an interference effect between 0–0 and 0–1 components, which produces an additional RR selectivity among the mixing nontotally symmetric modes.[31] It selects for A_{2g} modes at excitation wavelengths falling in between α and β bands, while excitation on either side selects for B_{1g} and B_{2g} modes.[35] This is the reason that ap bands are dominant with 530.9-nm excitation, whereas dp bands dominate the 568.2-nm excited spectrum (Figure 14).

2.7.4 C-term RR Scattering

The C-term RR scattering is a dominant mechanism when the exciting frequency is in resonance with a vibronic side band of a forbidden or weakly allowed 0–0 electronic transition, where the side band is allowed ($\mu_s^0 \neq 0$) due to the vibronic coupling between the 0–0 transition and another strongly allowed transition ($|g\rangle \rightarrow |s\rangle$). Under such conditions, the vibronic transition moment μ_e' described by equation (4) is much greater than μ_e^0 and since the electronic factor is $(\mu_e')^2$ in equation (8), the C-term can outweigh the B-term. The special feature of the C-term RR scattering is that it gives rise to first overtones ($k = l$) and binary combination tones ($k \neq l$) of those vibrational modes that are effective in coupling the two electronic states, instead of the fundamentals. This is because the numerator of the C-term equation (8) contains products of two Q-dependent integrals, $\langle j|Q_k|\upsilon\rangle$ and $\langle\upsilon|Q_l|i\rangle$. Since each of these connects vibrational states differing by one quantum, the final state, $|j\rangle$, must differ from $|i\rangle$ by two quanta, i.e., $j = i \pm 2$, as diagrammatically shown in Figure 15. Consequently, only first overtones ($k = l$) and binary combinations ($k \neq l$) are enhanced by the C-term. An example is shown in Figure 15(a), where overtone and combination bands involving the high-frequency ap and dp modes $\nu_{19}(A_{2g})$, $\nu_{10}(B_{1g})$, $\nu_{11}(B_{1g})$, $\nu_{20}(A_{2g})$, and $\nu_{29}(B_{2g})$ in the β-resonant spectrum of vanadyl tetraphenylporphyrin, VO(TPP), are seen to be dramatically stronger than the fundamentals.[32,42] The α absorption band shows no discernible intensity in this case (Figure 15(b)), indicating accidental degeneracy of the a_{1u} and a_{2u} porphyrin π orbitals, while the β band retains ≈10% of the intensity of the Soret band. As a result, $\mu_e^0 \approx 0$ but $\mu_e' \neq 0$ and $B \ll C$.

3 APPLICATIONS

3.1 The Mononuclear Type-1 Cu Site in Cupredoxins

The mononuclear blue (or type 1) copper proteins (cupredoxins) (*see* ***Copper Proteins with Type 1 Sites***), involved in biological electron transport, share a common structural motif, in which the single Cu(II) ion is tightly bound (1.9–2.2 Å) to two histidine and one cysteine ligand

Encyclopedia of Inorganic and Bioinorganic Chemistry, Online © 2011 John Wiley & Sons, Ltd.

This article was originally published in the *Encyclopedia of Inorganic Chemistry* in 2008 by John Wiley & Sons, Ltd.
DOI: 10.1002/9781119951438.eibc0303

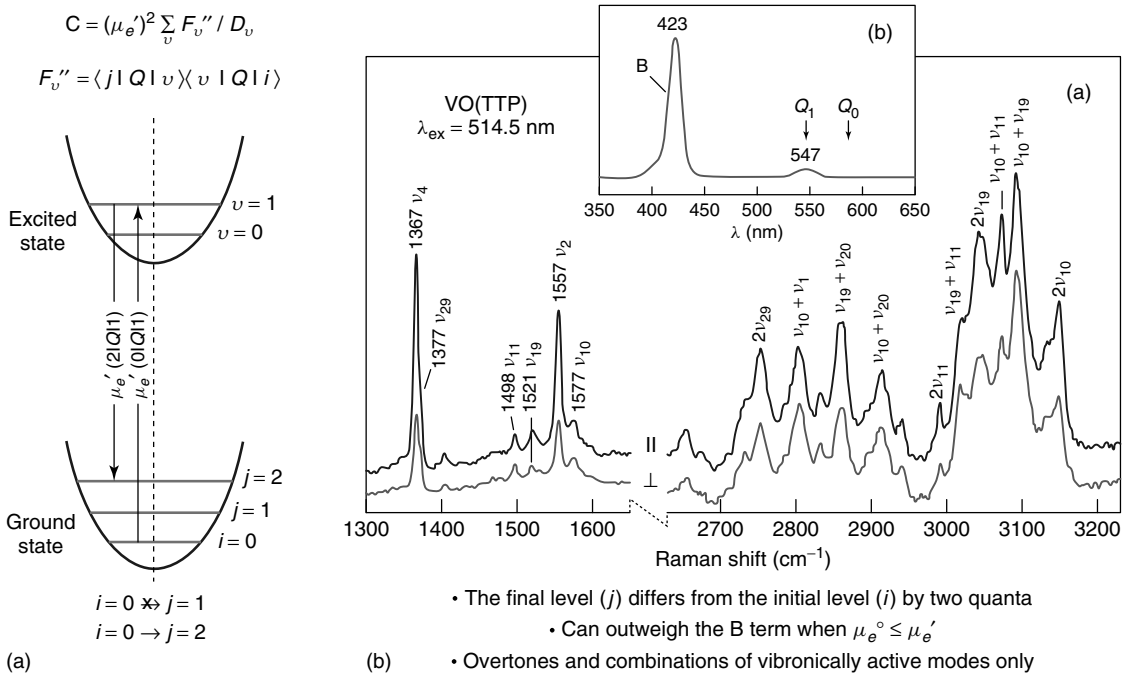

Figure 15 (A) Diagrammatic representation of Raman process responsible for C-term resonance scattering. The applicable electronic transition moment and vibrational overlap integral is indicated for each contributing transition for $\upsilon = 0$ and 1 intermediate levels of the resonant excited state. (B) The RR spectra (a) in parallel ($\parallel$) and perpendicular ($\perp$) scattering of solid (VO)TPP (rotating KCl pellet) excited at 514.5 nm showing strong enhancement of overtone and combination modes involving vibronically active ν_{19}, ν_{10}, ν_{11}, and ν_{29}, which themselves are very weak. The Q_0 absorption band (b) is virtually invisible in this case, giving very large overtone/fundamental ratios via the much larger C-term than B-term scattering

in a distorted trigonal CuN_2S planar geometry.[43–47] These three residues are conserved in all cupredoxins. A methionine thioether sulfur atom or, in some cases, a glutamine amide oxygen atom is present above the trigonal plane at a long distance (~2.6–3.1 Å). The azurin structure is different in that it has a fifth distant (~2.8–3.2 Å) ligand to copper, the peptide carbonyl oxygen from glycine (Gly45) across the N_2S plane (His46, His117, Cys112) from the methionine residue (Met121).[48–50] The trigonal bonding arrangement lowers the energy of the half-occupied copper $d_{x^2-y^2}$ orbital, relative to its energy in the usual tetragonal complexes of Cu(II), and in addition orients $d_{x^2-y^2}$ for optimal overlap with the π, instead of the σ filled orbital on the cysteine sulfur atom. Both factors lead to an unusually low energy (Cys)S → Cu(II) CT transition, ~625 nm, which accounts for the intense blue color of these proteins.

The main effect of CT excitation should be to weaken the Cu(II)–S(Cys) bond, and RR enhancement of the Cu(II)–S(Cys) stretching mode, $\nu(CuS)_{Cys}$, is therefore expected. This is a FC overlap argument, based upon equation (6). The Cu(II)–S(Cys) bond is short (~2.1–2.2 Å)[51] and a high stretching frequency is expected, ~400 cm^{-1}. The other Cu(II)–ligand stretches should be at much lower frequencies, because of the very long bonds for the methionine and peptide ligands, and because of the high effective mass of the rigid imidazole rings. Hence, a single dominant RR band might be expected, near 400 cm^{-1}. This is, in fact, what is observed[52] for a set of model compounds, LCu(II)–SR, where L = hydrotris(3,5-diisopropyl-1-pyrazolyl)borate (Figure 16).[53] When R is varied from *t*-butyl to triphenylmethyl to pentafluorophenyl, the frequency of this band decreases from 437 to 422 to 409 cm^{-1}, consistent with the expected weakening of the Cu–S bond due to increasing electron withdrawal. For the blue copper proteins, however, laser excitation within a (Cys)S → Cu(II) CT band results in a group of four or more strong RR fundamental bands near 400 cm^{-1}, as well as a series of weak-to-moderate bands below 300 cm^{-1} and groups of weaker features in the first (~800 cm^{-1}) and second (~1200 cm^{-1}) overtone regions of the ~400 cm^{-1} fundamentals.[43–47] The 647.1-nm excitation spectrum of azurin from *Pseudomonas aeruginosa*,[43] shown in Figure 17, exemplifies the unusual but characteristic richness of the type-1 copper RR scattering. Another property is the species dependence of RR scattering from proteins that have ostensibly the same active site structure. Despite homologous structures, different families of blue copper proteins, as well as individual members of the same family, exhibit considerable dissimilarities regarding the number of RR modes observed, their frequencies, and relative intensities (Figure 18).

The source of this band multiplicity and spectral differences has been a matter of considerable speculation.[45,47]

Encyclopedia of Inorganic and Bioinorganic Chemistry, Online © 2011 John Wiley & Sons, Ltd.

This article was originally published in the *Encyclopedia of Inorganic Chemistry* in 2008 by John Wiley & Sons, Ltd.
DOI: 10.1002/9781119951438.eibc0303

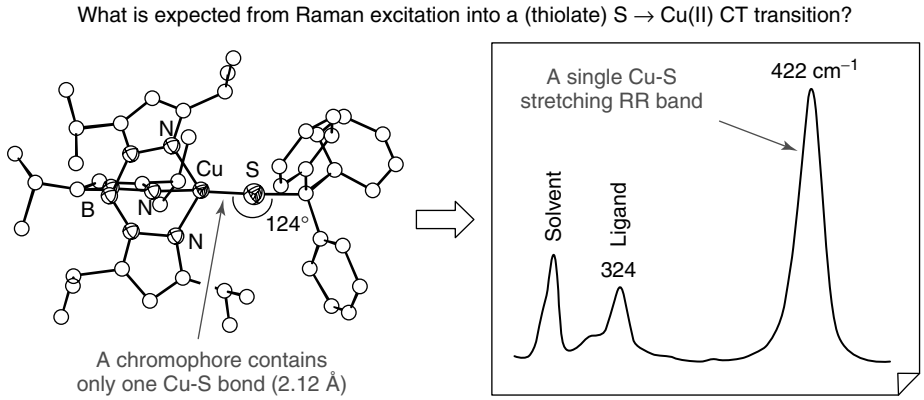

Figure 16 Structural diagram and 647.1-nm excitation RR spectrum of the blue copper site analog complex, LCu(II)−SR (L = hydrotris(3,5-diisopropyl-1-pyrazolyl)borate).[53] A single Cu–S stretching mode is seen in the RR spectrum,[52] as expected from excitation into RS → Cu CT transition of a chromophore containing only one terminal Cu–S bond

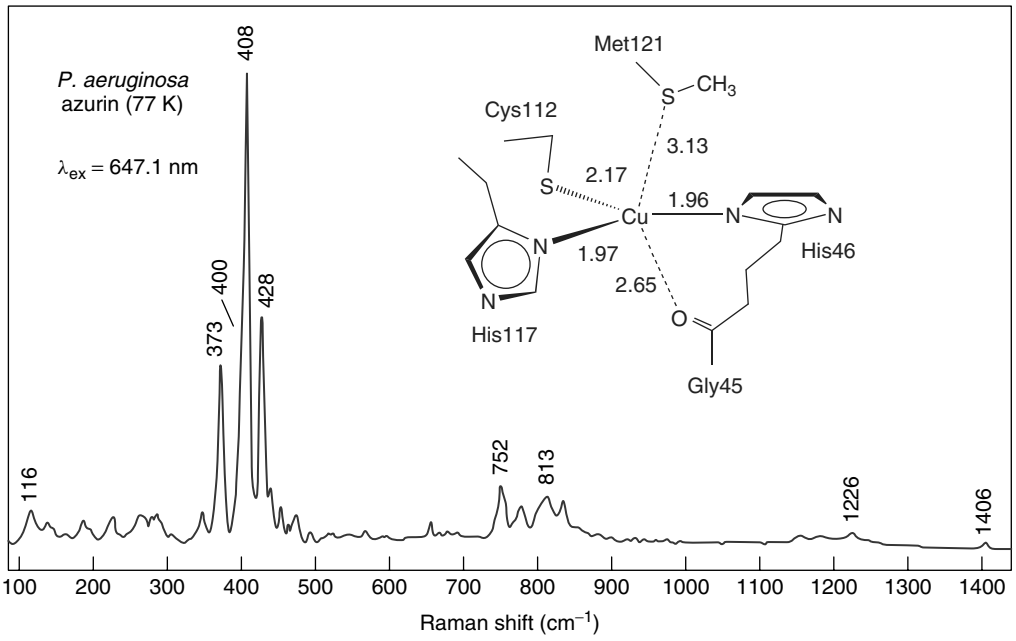

Figure 17 Low-temperature (77 K) RR spectrum of *P. aeruginosa* azurin obtained with 647.1-nm excitation wavelength and structural drawing of the active site showing distances (Å) to the three strong (Cys112, His46, His117) and two weak ligands (Met121, Gly45)

Significantly, the LCu–SR model compound gives three RR bands of nearly equal intensities near 400 cm^{-1} when R = *s*-butyl. Normal coordinate analysis (NCA) calculations indicate that the simple interchange of a methyl group and a hydrogen atom, between R = *t*-butyl and *s*-butyl, is sufficient to induce significant mixing of the C–C–C bending coordinates, δ(CCC), with the Cu–S(thiolate) stretching coordinate, ν(CuS), thereby accounting for the three strong bands.[52] No doubt mixing of ν(CuS) with heavy atom bending coordinates of the cysteine ligand produces some complexity seen in the cupredoxin spectra. Such mixing was anticipated in an early study of stellacyanin,[54] in which the two main RR bands were each found to shift upon $^{65}\rightarrow^{63}$Cu substitution, by half the amount expected for an isolated Cu–S oscillator, implying nearly equal contributions from ν(CuS) and another coordinate. Further insight into the coordinate mixing phenomenon has been obtained by $^{34}\rightarrow^{32}$S substitution in *P. aeruginosa* azurin and site-specific mutants,[44,55,56] *A. lcaligenes denitrificans* azurin,[57] *Cucumber sativus* stellacyanin,[58] and *Populus nigra* plastocyanin,[59] carried out by bacterial expression of the respective protein gene.

Figure 19 presents the 350–450 cm^{-1} RR spectra for the natural abundance wild-type (WT) *P. aeruginosa* azurin and its M121G (Met121 replaced with glycine) and H46D

Encyclopedia of Inorganic and Bioinorganic Chemistry, Online © 2011 John Wiley & Sons, Ltd.

This article was originally published in the *Encyclopedia of Inorganic Chemistry* in 2008 by John Wiley & Sons, Ltd.
DOI: 10.1002/9781119951438.eibc0303

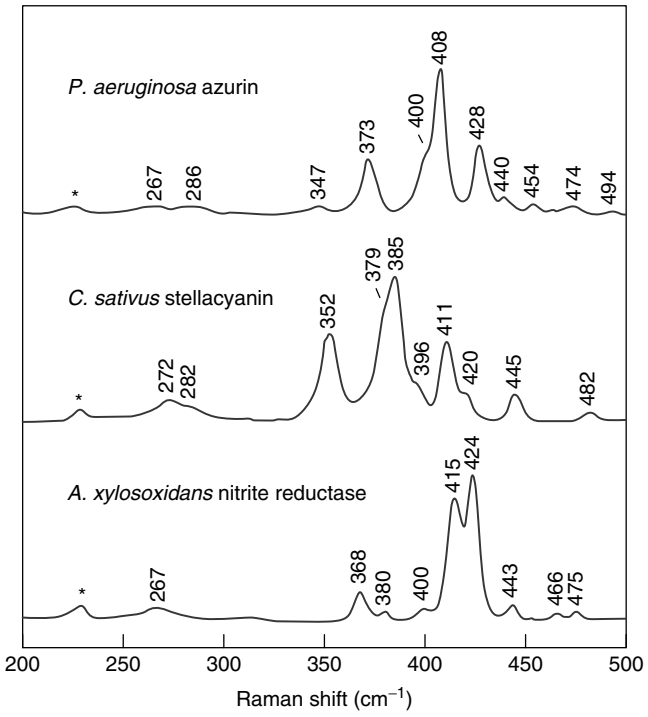

Figure 18 Low-temperature (77 K) RR spectra in the 200–500 cm^{-1} region of indicated blue Cu proteins excited at 568.2 (stellacyanin, NiR) and 647.1 nm (azurin). Asterisks denote ice band

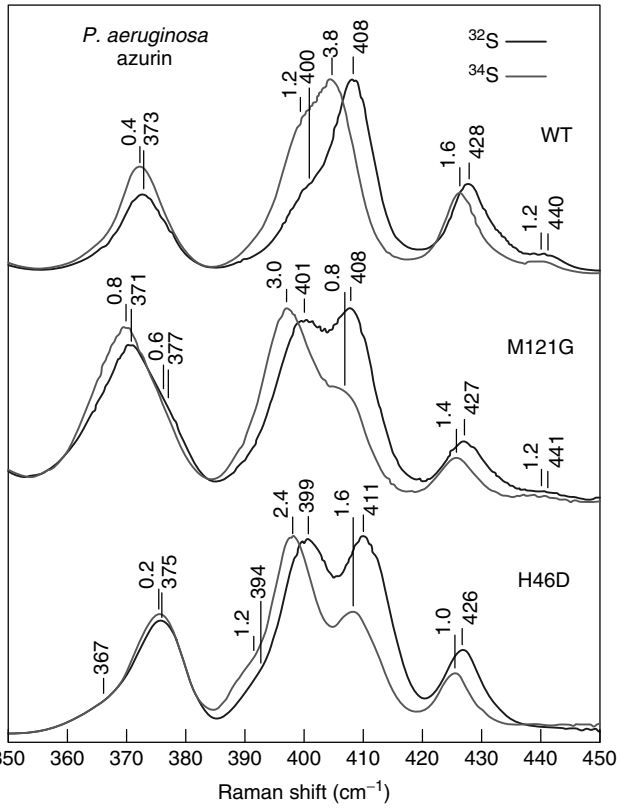

Figure 19 Low-temperature (77 K) RR spectra of *P. aeruginosa* azurins from cells grown on [^{32}S]- or [^{34}S]sulfate, excited at 647.1 (WT) and 568.2 nm (mutants). Italic numbers show the [$\nu(^{32}S) - \nu(^{34}S)$] band shifts

(His46 replaced with aspartate) Cu site mutants, and their corresponding [^{34}S]Cys112-substituted proteins.[55] Each spectrum shows four dominant RR peaks in this region (~370, ~400, 408, and ~427 cm^{-1}) that are characteristic for the type-1 Cu structure of the Cu(II)–Cys chromophores. Among these, the bands showing the greatest intensity and [^{34}S]Cys isotope shift, 408 (WT) and ~400 cm^{-1} (mutants), are identified with the vibrational mode involving primarily stretching of the Cu(II)–S(Cys) bond. This assignment is also corroborated by the $^{63/65}$Cu isotope shifts, as shown in Table 4.[44] A shift of the $\nu(CuS)_{Cys}$ character from the 408 cm^{-1} peak of WT to the ~400 cm^{-1} peaks in H46D and M121G indicates a decrease of the Cu(II)–S(Cys) interaction in both mutants as their Cu sites adopt more tetrahedral character relative to the WT site.[44,55,60]

There are far too many strong bands (up to nine) in the cupredoxin RR spectra near 400 cm^{-1} to be entirely due to the metal–ligand stretches, and attention must turn to other vibrational modes of the active site. Toward this end, site-selective isotopomers of azurin[61] and plastocyanin[62] were genetically produced with ^{2}H and ^{15}N labels in the cysteine C_β hydrogen and amide nitrogen atom positions, respectively, and their high-resolution RR spectra were recorded and analyzed.[43,61–63] Figure 20 shows the effects on the RR spectrum in the 350–450 (fundamental) and 650–850 cm^{-1} (first overtone) regions of selective deuterium labeling of the Cys112 β-hydrogen atoms in *P. aeruginosa* azurin, carried out by bacterial expression of the azurin gene using a Cys auxotrophic *E. coli* strain and cysteine(3,3-D_2).[61] Three of the four RR bands with $\nu(CuS)_{Cys}$ character are markedly affected by [$C_\beta D_2$]Cys112 incorporation; the 408 and 373 cm^{-1} bands undergo shifts of −6 and −4 cm^{-1}, respectively, while a shoulder near 400 cm^{-1} loses most of its intensity and drops ~3 cm^{-1} in frequency. The fourth S-dependent band at 428 cm^{-1} is much less sensitive to $C_\beta D_2$ labeling, shifting approximately −1.5 cm^{-1}. These shifts are further emphasized by the first overtone and combination bands as indicated in the figure. On the other hand, selective labeling of the nitrogen atom in the azurin Cys112 residue causes only small changes in the [^{15}N]Cys112 RR spectrum.[61] Three shoulders at 264, 400, and 377 cm^{-1} all shift downward by ~1 cm^{-1}, while the ^{34}S-sensitive peaks at 408 and 428 cm^{-1} shift less than 0.5 cm^{-1}, indicating only a small contribution from the amide group of the cysteinate ligand. Hence, the [$C_\beta D_2$]Cys and [^{15}N]Cys RR data[43,61–63] unambiguously establish that the multiple S-dependent bands of cupredoxins contain contributions mainly from CH_2 group-dependent deformations of Cu-bound cysteine,[43,56] as predicted by RR studies on model compounds[52] and ^{34}S- and $^{63/65}$Cu-substituted proteins.[54,55,59]

However, growth of azurins,[45,56,60,61] stellacyanin,[58] and plastocyanin[59] on $^{15}NH_4Cl$(aq), which completely labels

Encyclopedia of Inorganic and Bioinorganic Chemistry, Online © 2011 John Wiley & Sons, Ltd.

This article was originally published in the *Encyclopedia of Inorganic Chemistry* in 2008 by John Wiley & Sons, Ltd.
DOI: 10.1002/9781119951438.eibc0303

Table 4 Effects of ^{34}S, ^{65}Cu, and D_2O substitutions on frequencies of the 370–430 cm^{-1} RR bands for type-1 Cu sites in azurins

Azurin	RR frequency and isotope shift (cm^{-1})				Total shift
Wild type	373	400	408	428	
$^{32}S \rightarrow {}^{34}S$	−0.4	−1.2	−3.8	−1.6	−7.0
$^{63}Cu \rightarrow {}^{65}Cu$	−0.6	−1.0	−0.4	−0.4	−2.4
$H_2O \rightarrow D_2O$	−0.5	−1.0	−0.5	−1.5	−3.5
M121L[a]	372	400	405	427	
$^{63}Cu \rightarrow {}^{65}Cu$	−0.8	−0.6	−0.7	−0.4	−2.5
$H_2O \rightarrow D_2O$	−0.5	−1.0	−0.5	−2.0	−4.0
M121G[b]	371	401	408	427	
$^{32}S \rightarrow {}^{34}S$	−0.8	−3.0	−0.8	−1.4	−6.4
$^{63}Cu \rightarrow {}^{65}Cu$	−0.6	−0.8	−0.6	−0.4	−2.4
$H_2O \rightarrow D_2O$	−2.5	−1.5	−2.0	−2.0	−7.0
H46D[c]	375	399	411	426	
$^{32}S \rightarrow {}^{34}S$	−0.2	−2.4	−1.6	−1.0	−5.2
$^{63}Cu \rightarrow {}^{65}Cu$	−0.6	−0.6	−0.5	−0.2	−1.9
$H_2O \rightarrow D_2O$	−1.5	−3.5	−3.0	−4.5	−12.5

[a] ^{34}S data not available for M121L azurin.
[b] M121G azurin shows a shoulder at 377 cm^{-1}, which downshifts ∼0.6 and ∼0.3 cm^{-1} on ^{34}S and ^{65}Cu substitutions, respectively.
[c] H46D azurin shows a shoulder at 394 cm^{-1}, which downshifts ∼1.2 cm^{-1} on ^{34}S substitution. All data are from Czernuszewicz *et al.*[44]

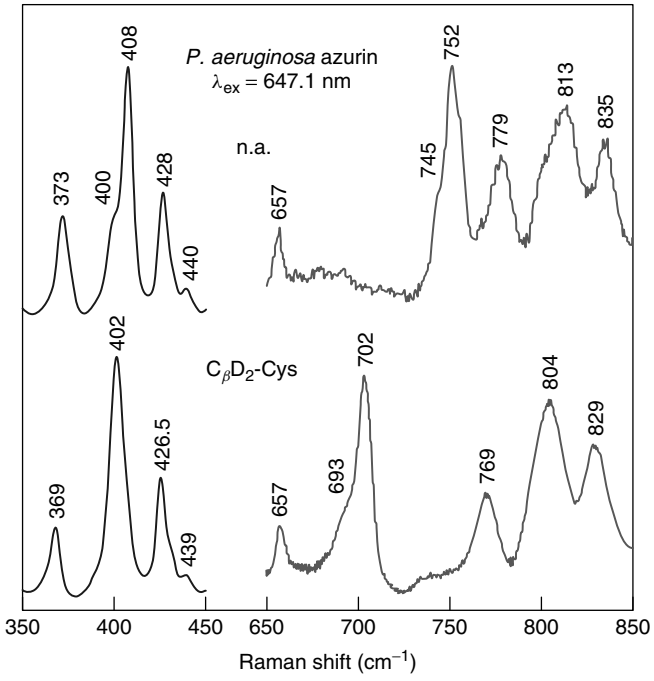

Figure 20 RR spectra of *P. aeruginosa* azurin and its [CβD2] Cys112-labeled protein obtained at 77 K with 647.1-nm excitation

all nitrogen atoms in the protein with ^{15}N, leads to the RR spectra that exhibit relatively large (1.0–4.2 cm^{-1} for *P. aeruginosa* azurin[56]) shifts to lower frequencies for nearly all the fundamental Raman bands in the 100–500 cm^{-1} region. Even the ^{34}S-sensitive strongest Raman bands in the 400 cm^{-1} region showed these downshifts.[56] At first, these results seem to support an earlier suggestion[54,64] that the deformation coordinates of Cu-bound histidine residues could also be good candidates for kinematic mixing with $\nu(CuS)_{Cys}$. Selective isotope labeling of the histidine imidazole ring has become possible through the availability of the azurin ligand mutants (H46G and H117G).[65–67] These mutants bind exogenous imidazole to generate blue copper sites almost indistinguishable from those of the WT proteins. Incorporation of [^{15}N] imidazole into either the H46G or H117G mutant gives no ^{15}N-sensitive RR bands other than a ∼285 cm^{-1} band assigned to $\nu(CuN_{Im})$ (∼1 cm^{-1} downshift).[68] Clearly, the substantially larger ^{15}N shifts observed for cupredoxins grown in the $^{15}NH_4Cl$ media are due to contributions from vibrations of the backbone amides rather than the histidine ligands. It is also apparent from the [^{15}N]Cys-dependent RR experiments that coupling of ν(CuS) to cysteine amide coordinates alone is not sufficient to explain the observed [^{15}N] protein shifts. That a single ν(CuS) stretch of cupredoxins undergoes extensive kinematic coupling with internal vibrational coordinates of not just one (cysteine) but several side chain residues has been obtained from NCA calculations of azurin[43] and plastocyanin.[63] The multiple vibrational features in the azurin RR spectrum arise from kinematic coupling between ν(CuS) and the internal ligand deformation modes of the coordinated Cys112 and at least three other residues (Thr113, Phe111, and Phe110) linked to Cys112 in the polypeptide chain.

3.2 Effects of Met121 Mutation on the Azurin Active Site

Substitution of amino acid residues at the metal center by site-directed mutagenesis can alter the geometry and properties of the active site, thus allowing elucidation of the minimal requirements for the proper functioning of the metalloprotein.[44,60] As an example, Figure 21 and Table 5 show the results of RR scattering from a series of *P. aeruginosa* azurins in which the active site Met121 has

Encyclopedia of Inorganic and Bioinorganic Chemistry, Online © 2011 John Wiley & Sons, Ltd.

This article was originally published in the *Encyclopedia of Inorganic Chemistry* in 2008 by John Wiley & Sons, Ltd.
DOI: 10.1002/9781119951438.eibc0303

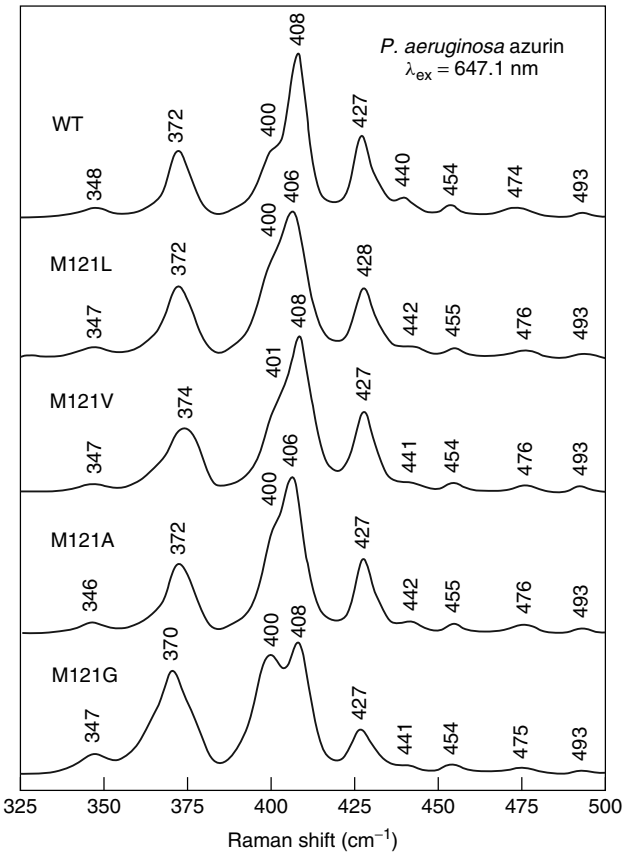

Figure 21 Low-temperature (77 K) RR spectra of *P. aeruginosa* azurin and indicated mutants (M121X, X = glycine, alanine, valine, and leucine) obtained in the 320–500 cm^{-1} region with 647.1- and 568.2-nm (M121G) excitations

been replaced by smaller hydrophobic amino acids: glycine (M121G), alanine (M121A), valine (M121V), and leucine (M121L).[60] The data emphasize that azurin RR spectra contain precise structural information regarding the nature of extremely subtle and minor variations in copper–amino acid interactions caused by Met121 replacements. Among the four most prominent peaks seen at 373, 400(sh), 408, and 427 cm^{-1} for WT azurin (Figure 21, top spectrum), the strongest one at 408 cm^{-1} bears the highest $\nu(CuS)_{Cys}$ character,[55] because it shifts the most to lower frequency (~4 cm^{-1}) upon ^{34}S substitution (Figure 19); the other three peaks shift appreciably less (~1.0–2.5 cm^{-1}). Thus, to a first approximation, the position of the most intense azurin fundamental peak reflects the strength of the Cu(II)–S(Cys) interaction. The RR spectral patterns of M121A, M121V, and M121L closely resemble that of the WT azurin; there are only small differences (±0.5 to ±2 cm^{-1}) in the positions of the bands (Table 5) and slight changes in the relative intensities, which indicate that a trigonal N_2S bonding arrangement about Cu(II) of the WT azurin has not been altered much by mutations of Met121 to alanine, valine, and leucine.[60] That M121A, M121V, and M121L retain trigonal character of the Cu is also highlighted

Table 5 Optical spectral parameters and $Cu–S_{Cys}$ RR stretching frequencies for *P. aeruginosa* azurins and their complexes with exogenous ligands[a]

Protein[b]	$\lambda_1(\varepsilon_1)$[c]	$\lambda_2(\varepsilon_2)$[c]	$\nu(CuS)_{Cys}$[d]
WT	**628** (5.5)	480 (0.04)	372, 400, **408**, 427
Met121Gly	**612** (4.9)	453 (0.8)	370, **400**, 408, 427
Azido	550 (1.9)	**422** (3.2)	300, 342, **357**, 391
Thiocyanato	550 (1.4)	**415** (3.5)	300, 318, **344, 353**, 392
Cyano	550 (0.9)	**432** (3.4)	300, 329, **338**, 352, 390
Met121Ala	**625** (5.6)	463 (0.5)	372, 400, **406**, 427
Azido	520 (2.7)	**409** (5.2)	299, **339**, 353, 363, 389
Thiocyanato	530 (1.7)	**409** (4.6)	300, **339**, 353, 389
Cyano	520 (1.1)	**413** (5.1)	298, **329, 338**, 351, 390
Met121Val	**626** (5.2)	460 (0.8)	374, 400, **408**, 428
Azido	520 (1.8)	**416** (5.5)	300, 345, **355**, 392
Thiocyanato	550 (1.1)	**416** (3.5)	300, **342**, 350, 393
Cyano	550 (1.0)	**420** (3.7)	300, 329, **337**, 352, 390
Met121Leu	**630** (6.0)	480 (0.1)	372, 400, **406**, 428
Azido	350 (1.2)	**412** (3.0)	300, 343, **358**, 391
Thiocyanato	–	–	301, **342**, 354, 391
Cyano	550 (1.1)	**416** (3.7)	300, 329, **337**, 354, 391

[a] λ_{max} are given in nm, ε_{max} in $mM^{-1}\,cm^{-1}$, and $\nu(CuS)_{Cys}$ in cm^{-1}; absorption and the RR bands with the highest intensity are indicated by bold numbers.
[b] All samples in pH 7 solutions.
[c] Values from Bonander *et al*.[69]
[d] Values from Franczkiewicz *et al*.[60]

by the axiality of the electron paramagnetic resonance (EPR) signals[69] and small ratios of the molar absorptivities for electronic transitions in the violet (λ_2, ~460 nm) and red regions (λ_1, ~620 nm), $R_f = \varepsilon(\lambda_2)/\varepsilon(\lambda_1)$[45,68] (Table 5).

In contrast, the M121G mutant displays the most pronounced changes in the RR spectrum near 400 cm^{-1} (Figure 21, bottom) relative to those of the WT and the other three Met121 mutants under study. It would seem from a comparison of the spectra of all five proteins that the frequencies of the M121G bands are not as changed as their intensities, including the major peaks at 370, 400, 408, and 427 cm^{-1}. However, as we have demonstrated above, through ^{34}S-isotope labeling of the Cys112 ligand,[44,55] the predominantly $\nu(CuS)_{Cys}$ band downshifted from 408 cm^{-1} (WT) to 400 cm^{-1} upon mutation of Met121 to glycine (Figure 19). Since there are still at least four major bands between 360 and 430 cm^{-1}, this implies an increase in frequency for the shoulder at 400 cm^{-1} observed in WT that now has moved to higher energy (408 cm^{-1}) in M121G. Such a frequency crossover indicates differences in kinematic coupling between vibrations of the Cu–Cys moiety because of ground-state alteration. A shift of the $\nu(CuS)_{Cys}$ character from the 408 cm^{-1} band of the WT to the 400 cm^{-1} band in M121G indicates that the Met121 → glycine substitution causes the $Cu–S_{Cys}$ interaction to weaken, as the Cu site adopts more tetrahedral character relative to the WT site. Consistent with the weaker $Cu–S_{Cys}$ interaction is the higher cysteine C_β–S stretching mode frequency (760 cm^{-1} in M121G versus 751 cm^{-1} in WT),[44] whereas the enhanced

Encyclopedia of Inorganic and Bioinorganic Chemistry, Online © 2011 John Wiley & Sons, Ltd.

This article was originally published in the *Encyclopedia of Inorganic Chemistry* in 2008 by John Wiley & Sons, Ltd.
DOI: 10.1002/9781119951438.eibc0303

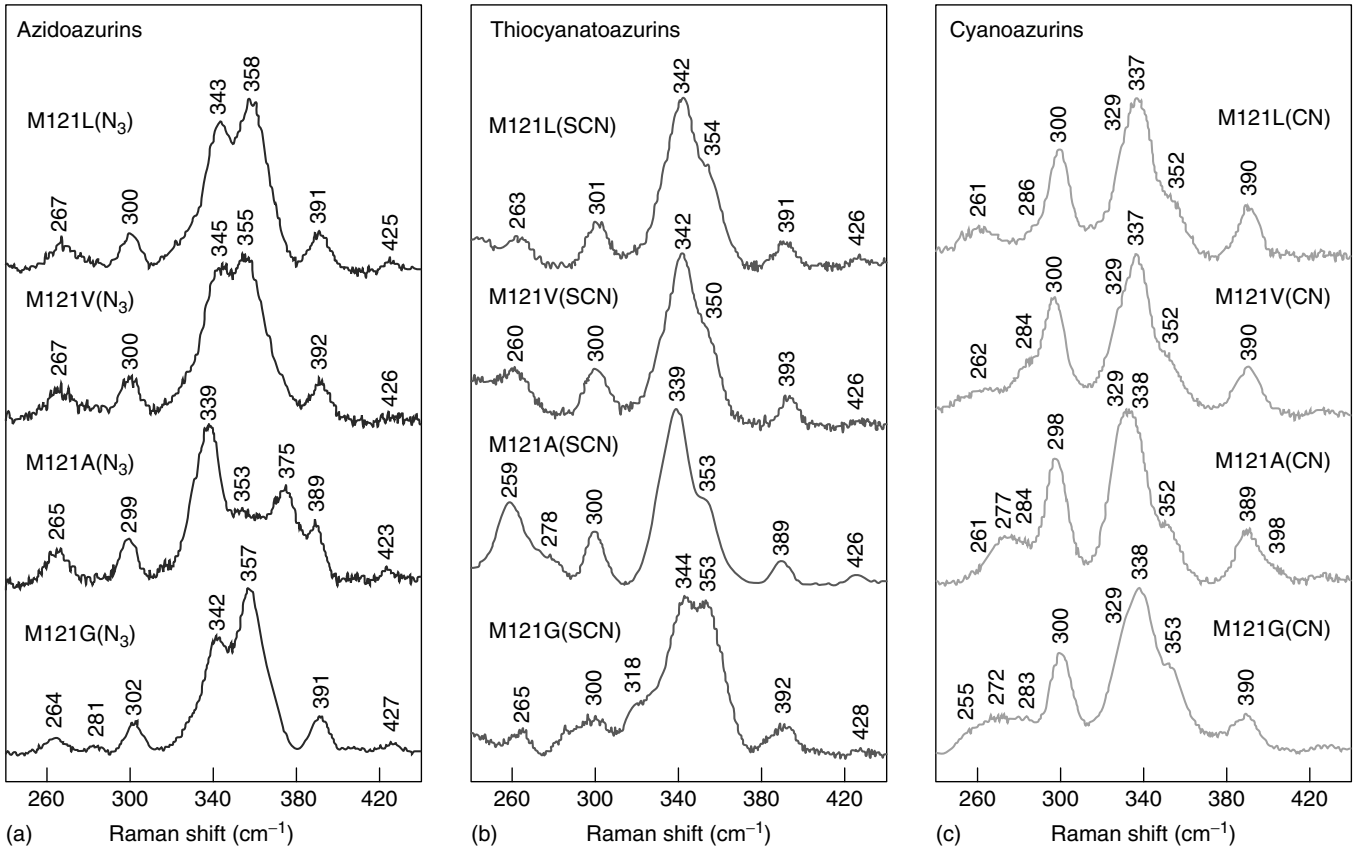

Figure 22 Low-temperature (77 K) RR spectra of indicated (a) azido, (b) thiocyanato, and (c) cyanoazurins obtained in the 240–440 cm^{-1} region with 406.7-nm excitation wavelength

tetrahedral character of the Cu in M121G is emphasized by increased absorption in the violet region (Table 5) and rhombicity of the EPR signal.[69]

3.3 Effects of Exogenous Ligand Coordination on Type-1 Cu Site

Figure 22 compares the RR spectra below 500 cm^{-1} for the azurin Met121X mutants (M121L, M121V, M121A, and M121G) treated with azide, thiocyanate, or cyanide, where most of the copper–ligand vibrations are expected to occur.[44,60] All spectra were obtained on frozen solutions (77 K) using a Kr^+ ion laser excitation at 406.7 nm. This excitation is in close resonance with an intense absorption band of the adducts in the violet region (Table 5), which arises from a hypsochromic shift of the ~620 nm (Cys)S → Cu(II) CT transition due to a strong apical interaction provided by exogenous ligand binding. The optical parameters and the vibrational frequencies of the dominant RR peaks are summarized in Table 5, and one example of the optical absorption of complexes is given in Figure 23. While the Met121X azurins exhibit the most strongly enhanced vibrational modes in the 400 cm^{-1} region, assigned to the

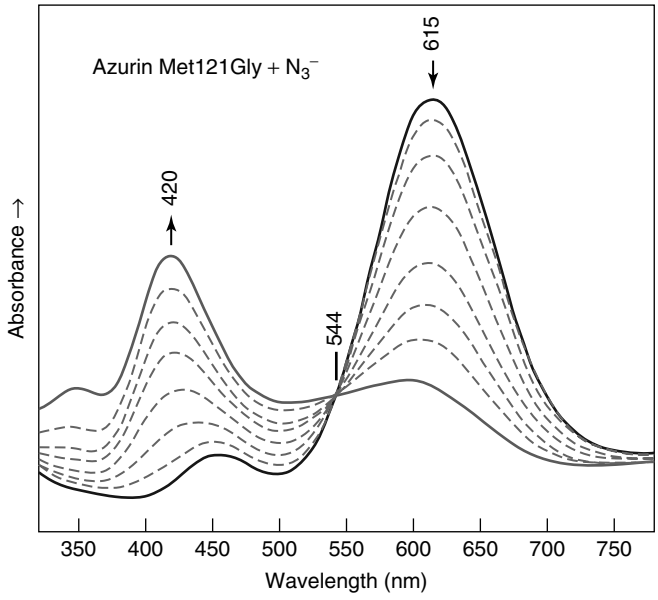

Figure 23 Changes in the UV–visible absorption spectrum of *P. aeruginosa* M121G azurin on sequential addition of aqueous sodium azide

Encyclopedia of Inorganic and Bioinorganic Chemistry, Online © 2011 John Wiley & Sons, Ltd.

This article was originally published in the *Encyclopedia of Inorganic Chemistry* in 2008 by John Wiley & Sons, Ltd.
DOI: 10.1002/9781119951438.eibc0303

Cu–S(Cys) vibrations, the strongest bands in their azido, thiocyanato, and cyano adducts occur in the ~350 cm^{-1} region. Such behavior is characteristic of a structural rearrangement of the metal center to a distorted tetrahedron with a markedly weakened Cu(II)–S(Cys) bond caused by strong coordination of an exogenous anion. To investigate the origin of these new sets of bands, the RR spectrum (413.1-nm excitation) was obtained on the ^{34}S-labeled M121G azurin mixed with aqueous NaN_3, focusing on the 280–450 cm^{-1} spectral region.[44,55] The greatest influence of ^{34}S-mass incorporation occurs with the most intense peak at 357 cm^{-1}, which shifts 3.0 cm^{-1} to lower frequency (Figure 24, bottom). This substantial isotope shift identifies the 357 cm^{-1} mode of M121G–azide as predominantly due to stretching of the Cu(II)–S(Cys) bond, analogous to the 401 cm^{-1} mode of M121G that also shifts 3.0 cm^{-1} upon ^{34}S substitution (Figure 24, top). Meanwhile, the frequency of the β-carbon–sulfur(Cys) stretch, $\nu(CS)_{Cys}$, increased from 758 cm^{-1} in M121G to 773 cm^{-1} in the M121G–azide complex (Table 5). These vibrational results indicate a substantially weaker Cu(II)–S(Cys) interaction in the M121G–azide complex and, by extension, in all other adducts.

The most remarkable feature of Figure 24 is that at least four more bands around the dominant 357 cm^{-1} vibration also display isotope sensitivity (^{34}S minus ^{32}S): one strong peak at 342 (−1.6) and three weaker peaks at 302 (−1.2), 391 (−2.6), and 427 (−1.2) cm^{-1}. Thus, these bands must also arise from the vibrational modes that involve some motion of the cysteinyl sulfur atom. This finding is extraordinary in that the extensive kinematic coupling between the $\nu(CuS)_{Cys}$ stretch and internal vibrational modes of the protein matrix exhibited by cupredoxins is evidently independent of their Cu(II)–S(Cys) bond strength.

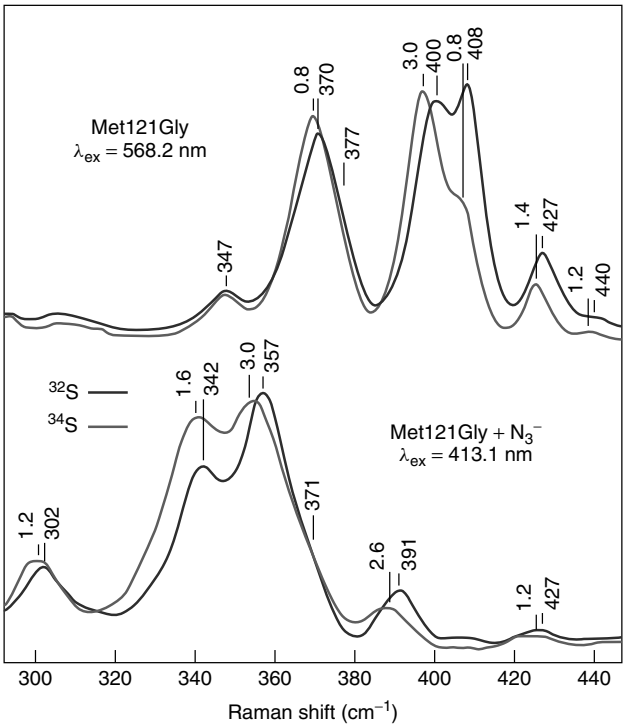

Figure 24 Low-temperature (77 K) RR spectra of *P. aeruginosa* M121G azurin and its azide adduct in the natural abundance and ^{34}S-labeled excited at 568.2 (M121G) and 413.1 nm (M121G–azide) Italic numbers show the [$\nu(^{32}S) - \nu(^{34}S)$] band shifts

Two azide-related vibrational modes in the M121A–N_3^- adduct were found at 375 and 2024 cm^{-1} and assigned as the ν(Cu–N_3) and $\nu_{as}(N_3)$ stretching modes based on $^{15}N_3/^{14}N_3$ isotopic shifts, −8 and −67 cm^{-1}, respectively, as shown in Figure 25.[60] Their counterparts in the glycine, valine, and leucine variants occur near 371 and 2045 cm^{-1} (Table 6), suggesting a weaker azide interaction with the Cu site than in the alanine variant. A nearly complete set of the thiocyanato-bound vibrational frequencies afforded by RR spectra of M121V–SCN^- has permitted accurate band assignments based on the observed $S^{13}CN^-$ and $SC^{15}N^-$ isotope shifts (Figure 26) and the results of NCA calculations.[60] In particular, the characteristic ν(S–CN) (~720 cm^{-1}) and ν(C≡N) (~2100 cm^{-1}) stretching frequencies established that SCN^- binds to the metal via the S atom to give a planar Cu–S–C≡N moiety. The CN^- ligand coordinates to the copper via its carbon atom giving rise to two ^{13}CN-sensitive weak bands at approximately 277 and 398 cm^{-1}, assigned as the ν(Cu–CN) stretch and the δ(Cu–C≡N) bend, respectively (Table 6).

3.4 Metal Substitution in Cupredoxins

Replacement of the Cu(II) ion in native and site-directed mutants of cupredoxins with other divalent metal ions such as Mn(II), Zn(II), Ni(II), Co(II), Ru(II), or Cd(II) proved useful in structural and spectroscopic characterization of type-1 copper sites by a number of different techniques.[70] Single crystal structures of several Zn(II)-, Cd(II)-, Ni(II)-, and Co(II)-substituted azurins showed the metal center that is better described as a distorted tetrahedron, instead of trigonal bipyramidal as in the Cu(II) azurin, because the metal ion is shifted away from the Met121 sulfur toward the carbonyl O-ligand of Gly45.[49,71] Figure 27 shows a comparison of the electronic absorption spectra obtained at room temperature from solutions of WT (Cu-containing) *P. aeruginosa* azurin and its Ni(II)- and Co(II)-substituted metalloderivatives.[70] Addition of Ni(II) or Co(II) to apoazurin causes the major cysteine-to-metal CT electronic transition to blue shift from 627 nm (Cu azurin) to 440 (Ni azurin) and 330 nm (Co azurin). As a result, pronounced changes are also observed in the RR scattering of Ni(II) and Co(II) azurins when the laser excitation is tuned through their absorption bands at 440 and 330 nm, respectively.This is shown in Figure 28, which reports the RR spectra taken in the 100–500 cm^{-1} region from a frozen (77 K) solution of *P. aeruginosa* Ni(II)-substituted azurin upon excitation with laser radiation at 406.7,

Encyclopedia of Inorganic and Bioinorganic Chemistry, Online © 2011 John Wiley & Sons, Ltd.

This article was originally published in the *Encyclopedia of Inorganic Chemistry* in 2008 by John Wiley & Sons, Ltd.
DOI: 10.1002/9781119951438.eibc0303

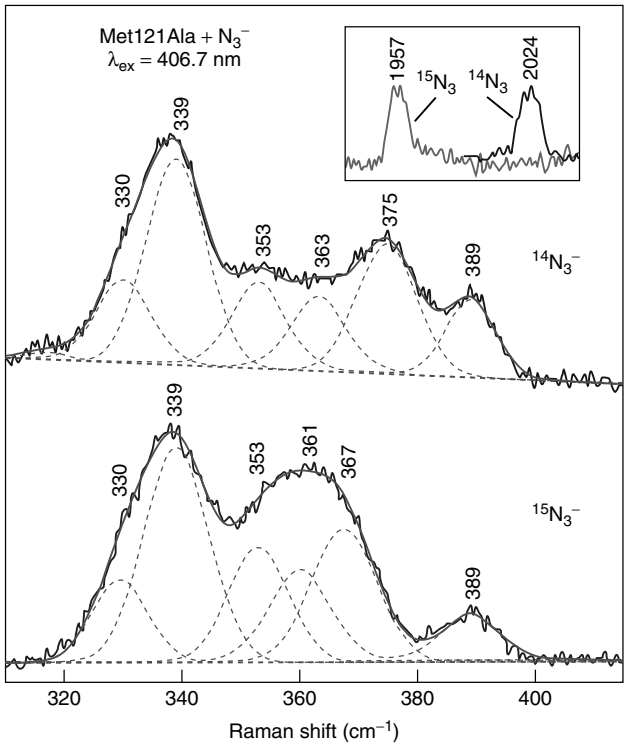

Figure 25 Curve-fitting analyses of the 310–415 cm^{-1} RR spectra of natural abundance and $^{15}N_3$-labeled azido-M121A azurins (77 K)

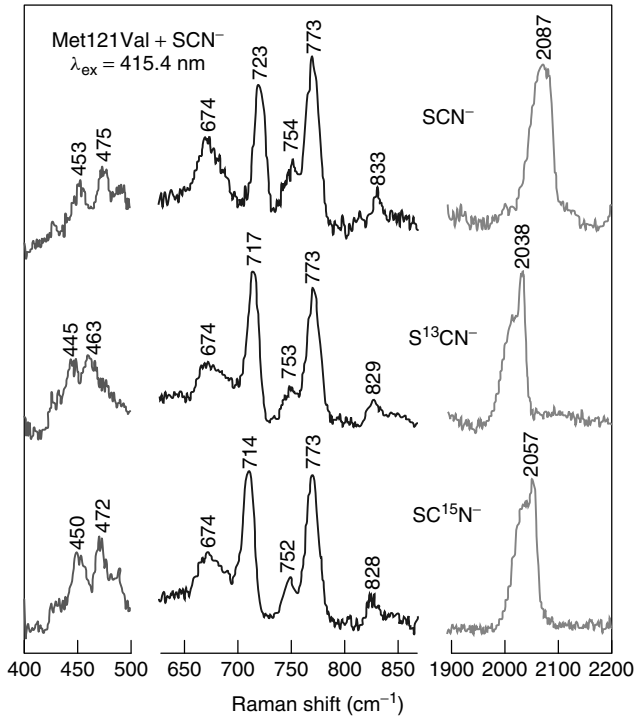

Figure 26 Low-temperature (77 K) RR spectra of thiocyanato-M121V azurin and its $S^{13}CN$ and $SC^{15}N$ isotopomers excited at 415.4-nm wavelength

Table 6 Ligand vibrations of *P. aeruginosa* azurin derivatives[a]

Vibration[b]	M121G	M121A	M121V	M121L
ν(C–S)$_{Cys}$[c]	758	753	758	751
		Azidoazurins		
ν(C–S)$_{Cys}$[c]	773	771	772	773
ν(Cu–N_3)	∼371sh	∼375sh	∼370sh	∼370sh
ν_{as}(N_3)	2042, 2051sh	2024	2048	2044
		Thiocyanatoazurins		
ν(C–S)$_{Cys}$[c]	768	766	773	768
ν(Cu–SCN)	242	237	240	244
δ(S–C≡N)$_{oop}$	454	446	453	450
δ(S–C≡N)$_{ip}$	470	457	475	472
ν(C–S)	–	712	723	–
ν(C≡N)	2072	2103	2087	2070
		Cyanoazurins		
ν(C–S)$_{Cys}$[c]	770	767	770	771
ν(Cu–CN)	–	277	–	–
δ(Cu–C≡N)	–	398	–	–

[a]Values for frequencies reported in cm^{-1} from RR spectra; sh = shoulder. [b]Cu–L and internal ligand vibrations of exogenous ligand (ν = stretching, δ = bending, as = antisymmetric, ip = in-plane, and oop = out-of-plane), except where noted. [c]C–S stretch of endogenous cysteine ligands; ν(C–S)$_{Cys}$ = 751 cm^{-1} for WT azurin.

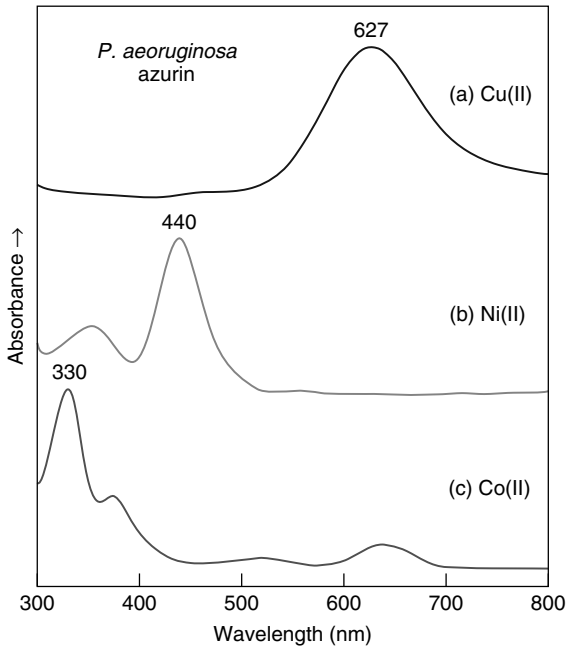

Figure 27 Room temperature UV–visible spectra of (a) native *P. aeruginosa* azurin and its (b) Ni(II)-, and (c) Co(II)-substituted derivatives

413.1, 441.6, 457.9, and 488.0 nm, and in Figure 29 where its 413.1-nm excitation spectrum is compared to that of the WT protein excited at 647.1 nm. Table 7 lists the observed RR

Encyclopedia of Inorganic and Bioinorganic Chemistry, Online © 2011 John Wiley & Sons, Ltd.

This article was originally published in the *Encyclopedia of Inorganic Chemistry* in 2008 by John Wiley & Sons, Ltd.
DOI: 10.1002/9781119951438.eibc0303

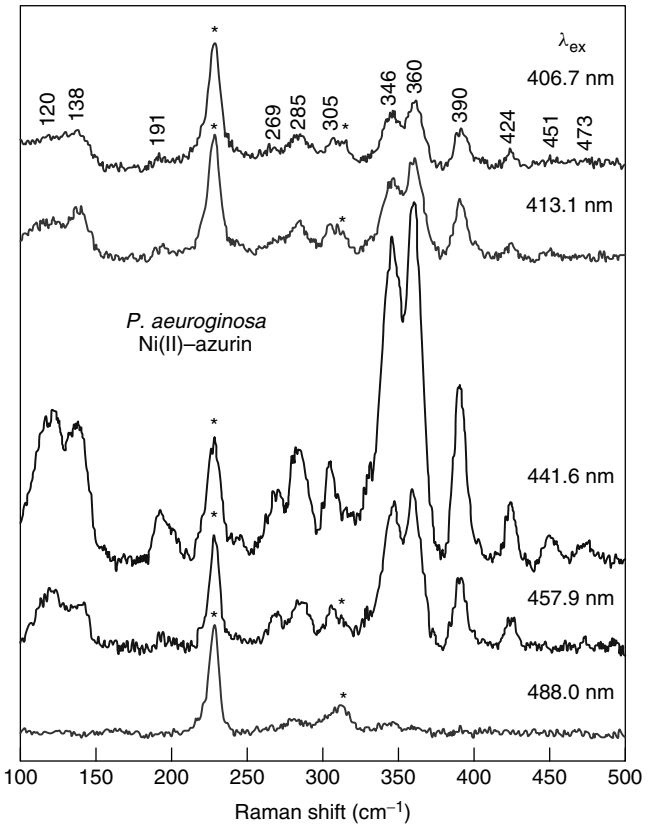

Figure 28 RR spectra (77 K) of Ni(II)-substituted *P. aeruginosa* azurin obtained with indicated excitation wavelengths. Asterisks indicate ice Raman bands

frequencies for the fundamental vibrations (100–1750 cm^{-1}) of both native *P. aeruginosa* azurin and its Ni(II) derivative,[70] together with those reported for Cu(II) and Ni(II) derivatives of *Alcaligenes xylosoxidans* azurin II[72] and *R. vernicifera* stellacyanin.[73]

Ni(II)-substituted azurin gives numerous vibrational bands in the 100–500 cm^{-1} range, which are maximally resonance enhanced with exciting radiation at 441.6 nm (as judged by the intensity of the protein Raman peaks relative to the ice band) (Figure 28), and which uniformly correspond to the vibrational modes of native azurin (Figure 29). Essentially, all of the 100–500 cm^{-1} vibrational modes that are observed for the native Cu(II) azurin are also detected in its Ni(II) derivative. The major vibrations that are observed for the Ni(II)-substituted azurin include a group of three intense RR peaks at 346, 360, and 391 cm^{-1} (Figure 29a), which clearly correspond to the strongest RR peaks at 373, 401(sh), 408, and 428 cm^{-1} of the native Cu(II) azurin (Figure 29b). Similarly, Co(II)-substituted azurin also gives three bands at 345, 360, and 390 cm^{-1} upon preresonant excitation at 354.2 nm (spectrum not shown).[70] Although [^{34}S]Cys isotopic shifts are not available for Ni(II)- and Co(II)-substituted derivatives, the apoprotein samples of *P. aeruginosa* azurin were reconstituted with different Ni isotopes (^{58}Ni or ^{62}Ni) and their high-resolution RR spectra were recorded to provide evidence for the Ni(II)–ligand vibrations. Figure 30 shows that upon substitution of ^{62}Ni for ^{58}Ni, the peaks at 424, 390, 360, 346, 285, and 269 cm^{-1} undergo shifts of −0.4, −1.0, −2.0, −0.8, −1.6, and −1.4 cm^{-1}, respectively. Thus, all of these RR bands must arise from vibrational motions that have nickel–ligand oscillatory character. The strongest Ni(II)-azurin band at 360 cm^{-1}, which exhibits the largest isotope shift (−2 cm^{-1}) upon substitution of ^{58}Ni for ^{62}Ni is ascribed to the predominantly Ni(II)–S(Cys) stretching mode, $\nu(NiS)_{Cys}$, analogous to the dominant 408 cm^{-1} $\nu(CuS)_{Cys}$ mode in WT azurin. The $\nu(NiS)_{Cys}$ character is also detected for the bands at 346 and 390 cm^{-1} from their $^{62/58}$Ni isotope shifts (−0.8 and −1.0 cm^{-1}), which is consistent with kinematic coupling of the metal–thiolate stretch with internal vibrations of the cysteine ligand side chain observed in the RR spectra of cupredoxins. Meanwhile, the frequency of the β-carbon–sulfur(Cys) stretching vibration, $\nu(CS)_{Cys}$, increased from 751 cm^{-1} in Cu(II) azurin to 763 cm^{-1} in Ni(II) azurin (Table 7, Figure 29). Taken together, these vibrational results indicate that Ni(II) substitution causes a significant weakening of the metal–S(Cys) bond as the metal coordination changes from trigonal bipyramidal of Cu(II) azurin to tetrahedral in Ni(II)-modified protein. This bond weakening is supported by the trend found in X-ray crystallographic studies of *P. aeruginosa* azurin and its Ni(II) derivative, which showed a much longer Ni–S(Cys) bond distance (2.39 Å) in Ni(II) azurin than in the WT protein (2.25 Å).[49,71]

The excitation wavelength-dependent RR spectra (Figure 28) also provided unambiguous evidence for the nature of the CT electronic transition at 440 nm as due to (Cys)S → Ni(II). Figure 31 compares the Ni(II)-azurin optical absorption spectrum with excitation profiles for the three most intense $^{58/62}$Ni-sensitive RR bands at 346, 360, and 390 cm^{-1}. The profiles are quite similar and closely track the absorption band in the violet region.

3.5 Substrate Binding to Type-2 Cu Site in Blue Nitrite Reductase

Copper-containing nitrite reductases (NiRs) (*see* ***Copper Enzymes in Denitrification***), involved in the anaerobic respiratory pathway as a part of the denitrification process, utilize two types of metal centers, type-1 copper (T1Cu) and type-2 copper (T2Cu), to transfer electrons in the reduction of NO_2^- to NO and further to N_2O and N_2.[74] X-ray crystal structure determinations of several Cu-containing NiRs showed that these enzymes are trimers constituted of three identical monomers, each monomer containing two Cu sites.[75–78] The coordination environment of the T1Cu is consistent with all other blue copper electron-transfer proteins. The T1Cu of *A. xylosoxidans* NiR is coordinated by two histidines, one methionine, and one cysteine in a distorted tetrahedral arrangement, while the T2Cu is ligated by two histidines from one monomer and by one histidine form a

Encyclopedia of Inorganic and Bioinorganic Chemistry, Online © 2011 John Wiley & Sons, Ltd.

This article was originally published in the *Encyclopedia of Inorganic Chemistry* in 2008 by John Wiley & Sons, Ltd.
DOI: 10.1002/9781119951438.eibc0303

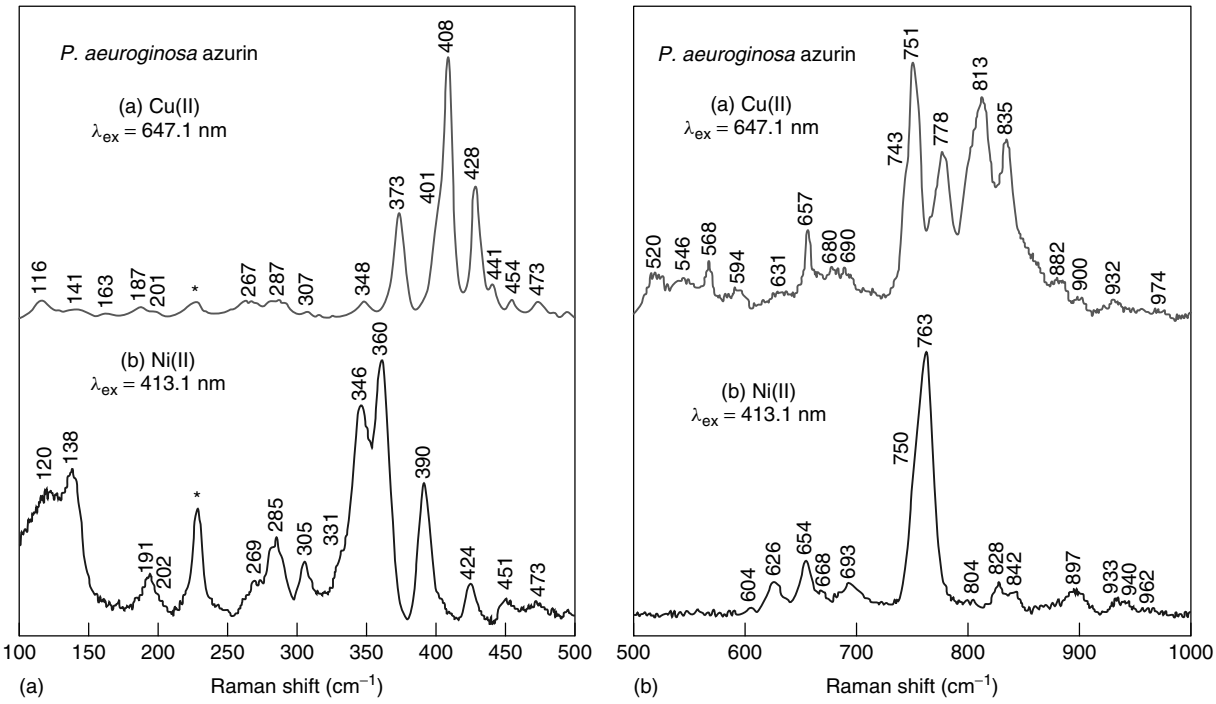

Figure 29 Low-temperature (77 K) RR spectra of *P. aeruginosa* azurin obtained in the(A) 100–500 cm^{-1} and (B) 500–1000 cm^{-1} regions on (a) native Cu(II) protein (647.1-nm excitation) and (b) its Ni(II)-substituted derivative (413.1-nm excitation). Asterisks indicate ice Raman bands

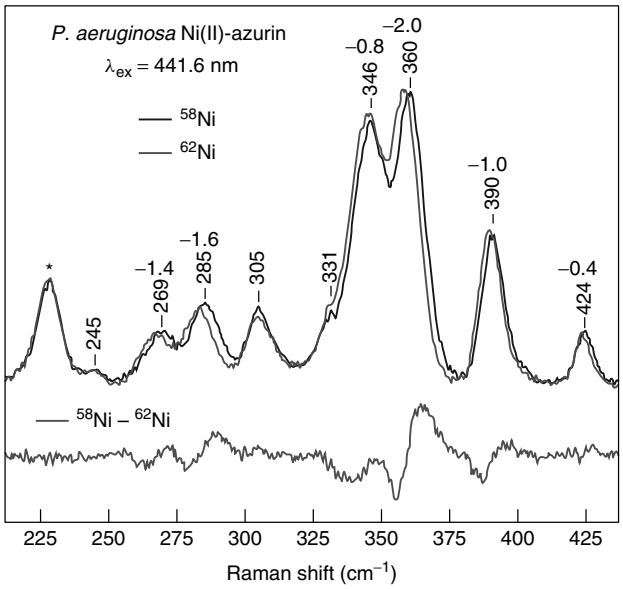

Figure 30 Effects of Ni-isotope substitution on the 200–430 cm^{-1} RR spectrum of *P. aeruginosa* azurin Italic numbers show the $[\nu(^{58}Ni) - \nu(^{62}Ni)]$ band shifts

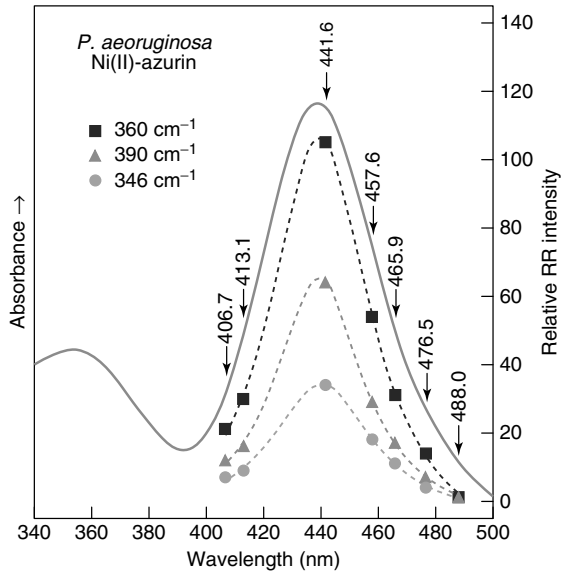

Figure 31 Excitation profiles of *P. aeruginosa* Ni(II) azurin (77 K) superimposed on the electronic absorption spectrum (298 K)

second monomer. The two copper sites of *A. xylosoxidans* NiR are directly connected through adjacent residues Cys130 and His129 that are coordinated to the T1Cu and T2Cu centers, respectively. This linkage provides a 12.5 Å pathway for efficient electron transfer from the T1Cu to T2Cu site.[78] X-ray crystallographic studies on the NO_2^--soaked NiR crystals have revealed that the T2Cu is the substrate-binding site, with an asymmetric coordination of NO_2^- to the Cu.[76–78]

Encyclopedia of Inorganic and Bioinorganic Chemistry, Online © 2011 John Wiley & Sons, Ltd.

This article was originally published in the *Encyclopedia of Inorganic Chemistry* in 2008 by John Wiley & Sons, Ltd.
DOI: 10.1002/9781119951438.eibc0303

Table 7 Observed resonance Raman frequencies (cm^{-1}) for fundamental vibrational modes of native Cu(II) and Ni(II)-substituted cupredoxins

Azurin[a] *P. aeruginosa*		Azurin II[b] *A. xylosoxidans*		Stellacyanin[c] *R. vernicifera*		
Cu(II)	Ni(II)	Cu(II)	Ni(II)	Cu(II)	Ni(II)	Assignment[d]
116	120					δ(NMS)
141	138					τ(CC)
187	191					δ(CCC) + δ(OCC)
267[e]	269	259		273	275	δ(CCN) + $\nu(MN)_{sym}$
287[e]	285	273		285		$\nu(MN)_{sym}$
307	305			315		$\nu(MN)_{asym}$
348	331sh	332sh		349		$\delta(CO)_{ip}$ + δ(CCN)
373	346[g]	375	331sh	360		δ(CCN) + δ(CCC)
401sh	**346**[g]	**400**		**376**	**350**	ν(MS) + δ(CCN)
408[f]	**360**	**412**	**349**	**387**	**376**	ν(MS) + δ(SCC)
428	390	426	366	418		δ(CCC) + ν(MS)
440	424			423		δ(OCC) + δ(CCC)
454	451	463		447	454	δ(OCC) + δ(CCC)
474	473			463	467	δ(CCN)
494	493			488		δ(CCN)
631	626					Amide IV
657	654	654				Amide VI
690	693					Amide IV + VI
743sh	750sh					$\delta(CO)_{wag}$ + ν(CS)
751	**763**	**750**	**755**		**762**	ν(CS)
846sh	842					Amide V
900	897					Amide V
932	933					Amide V
1001	1000					$\nu(C_\alpha C_\beta)$
1033	1045[g]					$\nu(C_\alpha C_\beta)$
1067	1068					$\nu(C_\alpha C_\beta) + \nu(C_\alpha N)$
1150sh	1147					$\nu(C_\alpha N)$
1193sh	1198					Amide III
1224	**1229**					Amide III + CH bend
1243sh	1252					Amide III
1272sh	1275					CH_2 twist
1300	1301					CH bend
1313	1312					CH bend + CH_2 wag
1344	1350					CH bend + CH_2 wag
1406	**1417**					CH_2 scissor
1433	1432					Amide II
1450	1449					Amide II
1504	1510					Amide II
1589	1588					Amide I
1631	1622					Amide I
1650	1643					Amide I
1678	1682					Amide I

[a]Native and Ni(II) azurin data from Czernuszewicz *et al*.[70] [b]Native and Ni(II) azurin II data from Hannan *et al*.[72] [c]Native and Ni(II) stellacyanin data from Musci *et al*.[73] [d]Assignments based on NCA calculations of *P. aeruginosa* azurin.[44] [e]Contain contributions from peaks at 262/268 and 280/286 cm^{-1}, respectively. [f]Boldface numbers indicate the RR peaks with the greatest intensity; sh = shoulder. [g]Possibly overlapping bands.

The RR spectroscopic investigation of blue Cu-containing *A. xylosoxidans* NiR (*Ax*NiR) has recently been carried out,[74] and the structural rearrangements at the electron-transfer site of T1Cu caused by substrate binding (NO_2^-) and the depletion of T2Cu, are briefly presented in this section. The electronic absorption spectrum of the *A. xylosoxidans* NiR exhibits the intense absorption band due to T1Cu (Cys)S → Cu(II) CT transition at 597 nm. The T2Cu site does not contribute to the visible spectrum. Trace (a) in Figure 32(A) shows the RR spectrum of the enzyme obtained at room temperature by excitation at 647.1 nm.[74] The *A. xylosoxidans* NiR has its own unique T1Cu spectrum in the $\nu(CuS)_{Cys}$ region, with one strong peak at 412 cm^{-1}, a prominent shoulder at 420 cm^{-1}, and additional small features at 364 and 376 cm^{-1}.

Encyclopedia of Inorganic and Bioinorganic Chemistry, Online © 2011 John Wiley & Sons, Ltd.

This article was originally published in the *Encyclopedia of Inorganic Chemistry* in 2008 by John Wiley & Sons, Ltd.
DOI: 10.1002/9781119951438.eibc0303

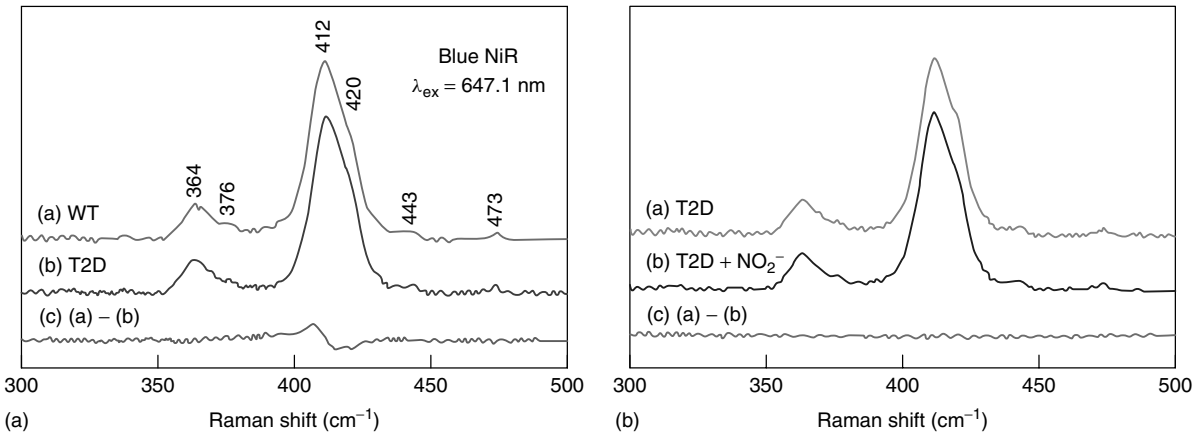

Figure 32 (A) RR spectra of (a) holo-*Ax*NiR (WT) and (b) its T2Cu-depleted protein (T2D) in 20 mM phosphate buffer (pH 7.0), and (c) their difference spectrum. (B) RR spectra of T2D *Ax*NiR in the absence (a) and presence (b) of nitrite and their difference spectrum (c)

To investigate the spectral contribution of the T2Cu, the RR spectra of type-2-copper-depleted (T2D) *A. xylosoxidans* NiR were measured. Trace b in Figure 32(A) shows that the T2D enzyme gave a spectrum almost identical to that of the holoenzyme (trace a in Figure 32A). The difference spectrum (trace c in Figure 32A) between T2D and holoenzyme revealed that the Raman bands associated with stretching the Cu(II)–S(Cys) bond, particularly those at 412 and 420 cm^{-1}, are slightly shifted to higher frequencies upon removal of the T2Cu ion, because of the subtle rearrangement of the T1Cu–Cys130–His129–T2Cu intersite structure.

By the sensitive RR difference spectroscopic technique, *A. xylosoxidans* NiR in the presence of various nitrite concentrations has been probed (Figure 33). The RR spectra of blue NiR recorded in the presence and absence of nitrite do not show significant changes (Figure 33a and b), but their difference spectra (Figure 33i) clearly show that the substrate binding alters the structure of the T1Cu site in NiR. The Raman bands of $\nu(CuS)_{Cys}$ at 412, 420, and 364 cm^{-1} all shift to higher energies in the presence of nitrite, and the intensity of the difference spectra depends on the concentration of nitrite (Figure 33c–i). These spectral changes, upon treatment of the enzyme with aliquots of increasing NO_2^- concentration, imply that nitrite does not enter the coordination sphere of the T1Cu center in NiR but rather binds to its T2Cu ion, as had been previously established by X-ray crystallography.[76–78] The increased frequencies of the Raman bands at 412, 420, and 364 cm^{-1} in nitrite-bound enzyme suggest that there could be a stronger Cu(II)–S(Cys) bonding than that in the absence of substrate, or a weakened hydrogen bonding to the coordinated sulfur ligand of cysteine, as a result of the T1Cu–T2Cu intersite structural rearrangement. That substrate binding occurs at the T2Cu site has been supported by the RR spectra of T2D *A. xylosoxidans* NiR measured in the presence and absence of nitrite. The results are presented in Figure 32(B), where it can be seen that the spectrum of T2D enzyme does not show any changes in the $\nu(CuS)_{Cys}$ bands by the addition of nitrite, as evident from the nitrite-treated T2D minus untreated T2D difference spectrum (trace c in Figure 32B).

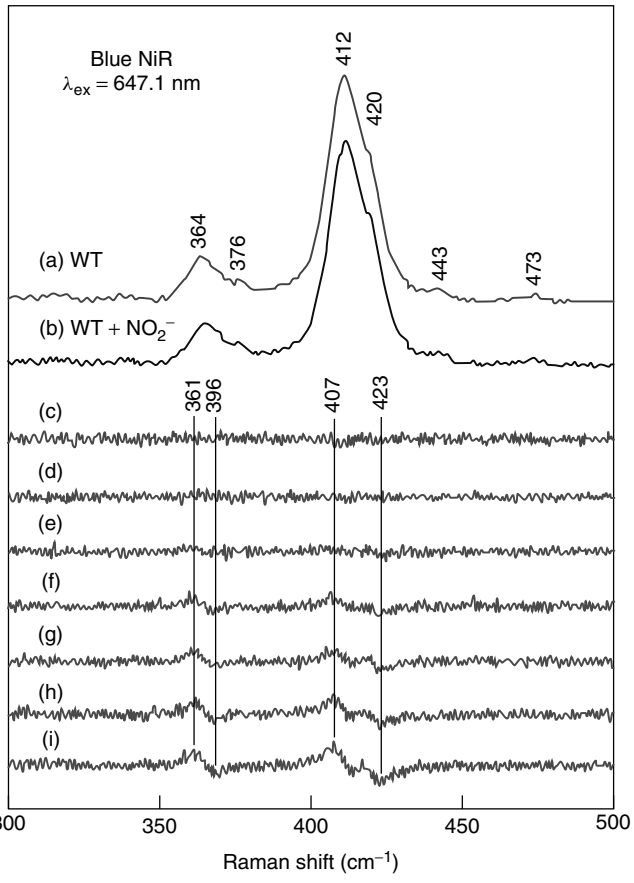

Figure 33 RR spectra of (a) holo-*Ax*NiR (0.5 mM) and (b) its complex with nitrite (10 mM). Traces (c–i) are difference RR spectra between those in the absence and presence of nitrite: (c) none; (d) 0.5 mM; (e) 1.25 mM; (f) 2.5 mM; (g) 4.0 mM; (h) 5.0 mM; (i) 10 mM

Encyclopedia of Inorganic and Bioinorganic Chemistry, Online © 2011 John Wiley & Sons, Ltd.

This article was originally published in the *Encyclopedia of Inorganic Chemistry* in 2008 by John Wiley & Sons, Ltd.
DOI: 10.1002/9781119951438.eibc0303

3.6 The Mononuclear FeS_4 Site in Rubredoxins

Iron–sulfur clusters (*see* ***Iron–Sulfur Proteins***), involved in a variety of biological redox processes, photosynthesis, nitrogen fixation, and respiration, have a common building block with Fe tetrahedrally coordinated to four S-donor ligands.[16,22,79] In 1-Fe rubredoxins, in which the building block itself constitutes their active site, the sulfur atoms belong to four cysteine amino acids of the protein backbone. In [2Fe–2S] ferredoxins, the iron ions are bridged by inorganic μ_2-sulfides and bound to two sulfur atoms of cysteine residues. In cuboidal [3Fe–4S] clusters, each iron is ligated to three of the four acid-labile sulfur atoms and to one additional cysteinyl sulfur. The most prevalent cluster type is found in [4Fe–4S] proteins, the bacterial ferredoxins, and high-potential iron–sulfur proteins, in which each iron interacts with three inorganic μ_3-sulfides and sulfur atom of cysteine, forming a cubane shape with iron and sulfur atoms in alternation.[79] The Fe–S proteins are brown in color, owing to visible absorption bands that are associated with CT transitions from sulfur (both bridging and terminal) to Fe(III). Consequently, the structurally diverse 1-Fe, 2-Fe, 3-Fe, and 4-Fe centers of Fe–S proteins have been probed extensively with room- and cryogenic-temperature RR spectroscopy, using isotope labeling to identify the Fe–S cluster vibrational modes in the RR spectra.[22,79–85] As expected, the RR spectra show selective enhancement of Fe–S vibrations, due to the extension of the Fe–S bonds in the CT-excited states. The spectral patterns are unique and distinctive for different structural types and several detailed reviews on this subject have been published.[16,22,79]

Rubredoxin was the very first metalloprotein to which RR spectroscopy was applied. In 1970 and 1971, Long and coworkers found four bands in the metal–ligand stretching and bending region in the 488.0-nm excitation RR spectra of rubredoxin from *Clostridium pasteurianum*,[86,87] just the number of normal modes expected for a tetrahedral FeS_4 complex. A strong polarized band at 314 cm^{-1} was assigned to the totally symmetric breathing mode $\nu_1(A_1)$, involving the in-phase stretching of all four Fe(III)–S(Cys) bonds. The other three stretches (there must be four altogether, one for each bond) were assigned to the triply degenerate out-of-phase mode $\nu_3(T_2)$, observed weakly as a depolarized band at 368 cm^{-1}. The remaining two bands at 126 and 150 cm^{-1} were identified with the S–Fe–S bending modes, $\nu_2(E)$ (doubly degenerate) and $\nu_4(T_2)$ (triply degenerate), respectively. These four bands are close in frequency to the modes of the isoelectronic complex $[FeCl_4]^-$ = 385 (ν_3), 330 (ν_1), 133 (ν_4), and 108 cm^{-1} (ν_2).[88] Thus, the analysis of the protein RR spectrum was satisfyingly straightforward.

Subsequent RR studies,[89] with better spectral quality and with isotope shift data, have shown the situation to be more complex, however. Figure 34 shows an interesting variation

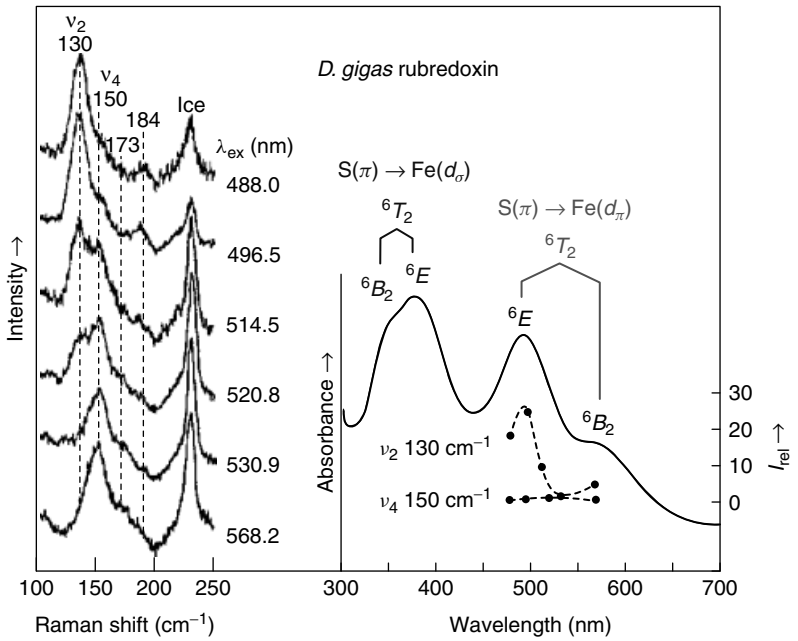

Figure 34 Variable wavelength RR spectra of a frozen *D. gigas* rubredoxin solution in the bending-mode region. The intensities of ν_2 and ν_4 were determined by ratioing them with the 227 cm^{-1} ice band (marked with an asterisk) intensity. The resulting excitation profiles are compared with the absorption spectrum, showing that ν_2 is strongly resonant with the 495-nm absorption band, while ν_4 is weakly resonant with the 565-nm shoulder. These transitions are assigned respectively to the ^6E and $^6B_2$ components of the S(π) → Fe(dπ)) charge-transfer transition, split by symmetry lowering from T_d to D_{2d}. The former electronic component provides A-term enhancement of the A_1 vibrational component of the E bending mode (ν_2), while the latter provides B-term enhancement to the E component of the T_2 mode (ν_4), via vibronic coupling with the nearby ^6E electronic transition

Encyclopedia of Inorganic and Bioinorganic Chemistry, Online © 2011 John Wiley & Sons, Ltd.

This article was originally published in the *Encyclopedia of Inorganic Chemistry* in 2008 by John Wiley & Sons, Ltd.
DOI: 10.1002/9781119951438.eibc0303

with laser wavelength of the $\nu_2(E)$ and $\nu_4(T_2)$ bending modes of rubredoxin from *Desulfovibrio gigas*. The excitation profiles, constructed by ratioing the band intensities of the frozen protein sample to the intensity of the nearby ice band at 227 cm^{-1}, showed $\nu_2(E)$ to be strongly resonant with the strong absorption band at 495 nm, while $\nu_4(T_2)$ is weakly resonant with the 565-nm shoulder. These results were interpreted on the basis of a previous electronic assignment by Eaton and Lovenberg,[90] also shown in Figure 34. Two CT transitions are expected in the visible region, from the sulfur π to the Fe d_π and d_σ orbitals, but these are split by a lowering of the effective symmetry of the chromophore, from T_d to at least D_{2d}, because of an elongation of the tetrahedron along the S_4 symmetry axis. The 495-nm band and its 565-nm shoulder were assigned respectively to the ^6E and $^6B_2$ components of the $Fe(d_\pi) \leftarrow S(\pi)$ transition. These components can be coupled vibronically via a mode of $B_2 \times E = E$ symmetry. The T_2 vibrational modes also have E and B_2 components in D_{2d} symmetry. Therefore, the E component of the T_2 mode can couple the weak 565-nm transition with the strong nearby 495-nm transition, thereby accounting for the ν_4 enhancement via the B-term scattering mechanism. On the other hand, the ν_2 enhancement in resonance with the strong 495-nm transition can be attributed to FC scattering, since the E (T_d) mode has A_1 and B_1 components in D_{2d} symmetry, and the A_1 component is subject to A-term enhancement. The second components of each mode, B_2 of ν_4 and B_1 of ν_2, are not observed because they lack effective enhancement mechanisms.

Further complexity was discovered when the Fe–S stretching region was reexamined at higher resolution in frozen protein solution at 77 K.[89] When the low-temperature spectrum was recorded with 568.2-nm excitation (Figure 35), three bands were now seen at 376, 363, and 348 cm^{-1}, not one, in the $\nu_3(T_2)$ region, implying the degeneracy being completely lifted. In addition, a prominent shoulder at 324 cm^{-1} became apparent on the ν_1 band. The assignment of the bands at 376, 363, and 348 cm^{-1} to ν_3 components was established by examining their isotope shifts in ^{54}Fe-reconstituted protein via RR difference spectroscopy, as shown in Figure 36. All three bands showed clear ^{54}Fe-isotope shifts to higher frequency, as expected for antisymmetric Fe–S stretching vibrations. The dominant RR band at 314 cm^{-1} did not shift on ^{54}Fe substitution, confirming its assignment to the FeS_4 breathing mode, ν_1 (the Fe atom does not move in such a mode). Likewise, a side band at 324 cm^{-1} showed no discernible ^{54}Fe shift; the intensity is canceled in the difference spectrum over the 314–324 cm^{-1} band envelope (Figure 36). This band was therefore assigned to a cysteine SCC bending mode, δ(SCC).[89]

To account for the main features of the rubredoxin RR spectrum, vibrational modes of a series of small molecule analogs, $[Fe^{III}(SMe)_4]^-$, $[Fe^{III}(SEt)_4]^-$, and $[Fe^{III}(S_2\text{-}o\text{-}xyl)_2]^-$ (SMe = methylthiolate, SEt = ethylthiolate, and S_2-o-xyl = o-xylene-α,α'-dithiolate), have been analyzed using RR and IR spectra of isotopomers (^{54}Fe, ^{34}S, and ^{2}H).[91] The vibrational spectra of analog complexes revealed that the splitting of the triply degenerate ν_3Fe–S stretching mode is mainly due to (i) nontetrahedral S–Fe–S angles, (ii) out-of-plane rotation of the S–C bonds, and (iii) kinematic coupling between Fe–S stretching and S–C–C bending modes, which is greatly dependent on the FeS–CC dihedral angles. Using a consistent force field for all three complexes, NCA calculations provided a good match to the observed values of ν_1, ν_2, ν_{3a-c}, and ν_4, and their respective isotope shifts.

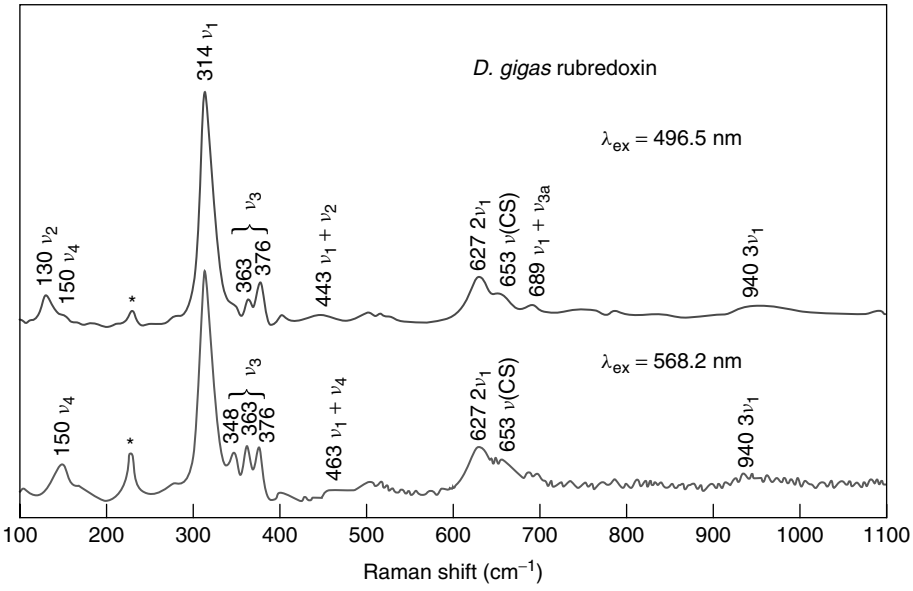

Figure 35 Low-temperature (77 K) RR spectra of *D. gigas* rubredoxin obtained in the 100–1100 cm^{-1} region using 496.5- and 568.2-nm excitations

Encyclopedia of Inorganic and Bioinorganic Chemistry, Online © 2011 John Wiley & Sons, Ltd.

This article was originally published in the *Encyclopedia of Inorganic Chemistry* in 2008 by John Wiley & Sons, Ltd.
DOI: 10.1002/9781119951438.eibc0303

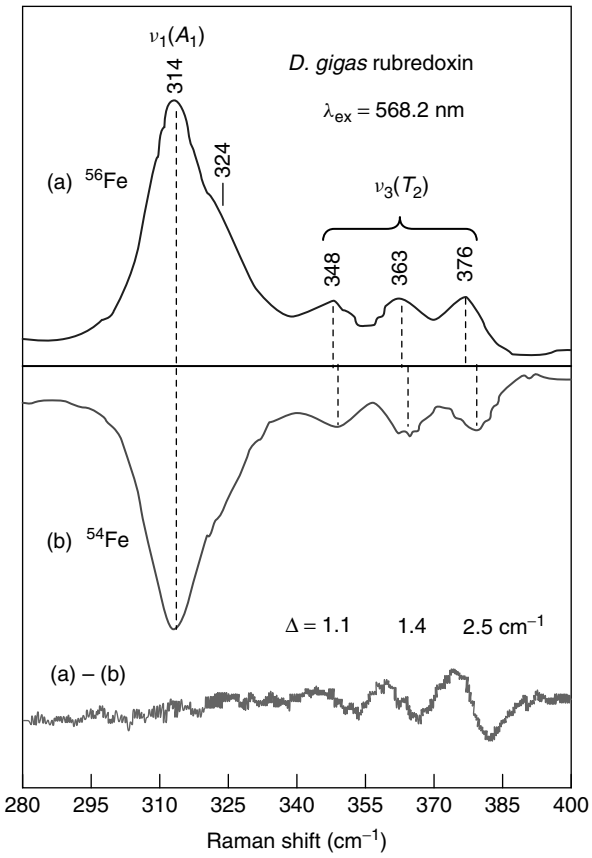

Figure 36 568.2-nm excited RR spectrum in the Fe–S stretching region for (a) natural abundance *D. gigas* rubredoxin and (b) of the protein reconstituted with ^{54}Fe

The rubredoxin RR bands and ^{54}Fe isotope shifts were also modeled with the same force field, which revealed a dominant influence of ν(FeS)/δ(SCC) mixing due to 180° FeS–CC dihedral angles for two of the cysteine ligands at the rubredoxin active site. However, proper calculation of the ν_1 frequency of rubredoxin required a significant reduction of the Fe–S stretching force constant (1.27 mdyn/Å), relative to that of the analog complexes (1.34 mdyn Å^{-1}). The lower force constant implies weaker Fe(III)–S(Cys) bonds. This reduction was proposed to reflect the influence of H bonding to the cysteinate S atom in the protein.[89] The H bonds reduce the negative charge on the S atoms and reduce their donor strength, i.e., weaken the Fe–S(Cys) bonds in the protein.

3.7 The FeS_4 and Fe–O–Fe Sites in Rubrerythrin

This intriguing nonheme homodimeric protein (*see* ***Iron Proteins with Dinuclear Active Sites***), originally isolated from the anaerobic sulfate-reducing bacterium *Desulfovibrio vulgaris*,[92] contains a unique combination of two types of chromophoric iron(III) sites in each subunit: one rubredoxin-like Fe(S-Cys)$_4$ center in the *C*-terminal domain and one nonsulfur, (μ-oxo)*bis*(μ-carboxylato)-triply bridged binuclear Fe(III) cluster in the *N*-terminal domain.[93,94] The initial spectroscopic indications of these sites have been confirmed by protein X-ray crystallography structural studies[95–97] (Figure 37), but the first evidence for the Fe–O–Fe structural unit in rubrerythrin came from RR spectroscopy.[92] Figure 37 shows low-temperature (77 K) RR spectra of as-isolated *D. vulgaris* rubrerythrin in a liquid N_2 cell with excitation at 496.5 and 406.7 nm.[92] These excitation wavelengths are in resonance with the well-separated (Cys)S → Fe(III) (~492 nm) and μ-oxo → Fe(III) (~370 nm) CT electronic absorption bands, respectively, of rubrerythrin. Figure 38 compares RR spectra obtained with 406.7-nm excitation for the protein contained in H_2O and the recrystallized protein dissolved in $H_2{}^{18}O$, D_2O, and $D_2{}^{18}O$. Band frequencies, isotope shifts, and assignments are listed in Table 8. The 496.5-nm excitation spectrum in Figure 37 (upper trace) is overwhelmingly dominated by the vibrational modes characteristic of rubredoxin-like Fe(Cys)$_4$ sites: a strong band at 314 cm^{-1}, assigned to the cluster breathing ν_1 mode; a set of widely spaced weaker bands at 340, 355, and 374 cm^{-1}, assigned to three components of the ν_3 antisymmetric Fe–S(Cys) stretch; weak bands at 128 and 156 cm^{-1}, assigned to ν_2 and ν_4 S–Fe–S bending modes; and numerous overtone and combination bands of the Fe–S(Cys) stretches in the 450–800 cm^{-1} region. Indeed, the number, positions, and intensities of these resonance-enhanced Raman bands closely match those observed for frozen solutions of rubredoxins from *D. gigas* (Figure 35, Table 8)[89] and *Pyrococcus furiosus*.[98]

In contrast, the RR spectrum of *D. vulgaris* rubrerythrin excited at 406.7 nm shows dramatically diminished intensities of the FeS_4 bands with concomitant enhancement of a band at 514 cm^{-1} (Figure 37, bottom trace). This band shifts 18 cm^{-1} to lower frequency (496 cm^{-1}) when the protein is dissolved in $H_2{}^{18}O$ (Figure 38). Therefore, the 514-cm^{-1} band must involve vibrational motion of a water-exchangeable oxygen atom. The frequency of this band and the ^{18}O isotope shift are those expected for the symmetric Fe–O–Fe stretch, ν_s(FeOFe), of a bent μ-oxo-bridged diiron(III) cluster that has one or two additional cobridging carboxylate ligands.[92] From the observed ν_s(FeOFe) frequency (514 cm^{-1}) and its ^{18}O isotope shift (−18 cm^{-1}), an Fe–O–Fe angle of 124° was calculated for the diferric cluster in rubrerythrin by solving a simple X–Y–X three-body vibrational problem.[21] The bridge substitution experiments also revealed a small but reproducible shift (+2 cm^{-1}) to higher frequency for the ν_s(FeOFe) stretch when the rubrerythrin crystals are dissolved in D_2O and $D_2{}^{18}O$ (Figure 38), implying involvement of hydrogen bonding to the oxo group at the Fe–O–Fe site. All these RR inferences have later been confirmed by protein X-ray crystallography performed on single crystals of all-ferric recombinant *D. vulgaris* rubrerythrin.[95,96] As shown in Figure 37, its Fe^{3+} ions are both pseudo-octahedrally coordinated; one Fe^{3+} ion is ligated terminally by one bidentate glutamate and one histidine, the other Fe^{3+} ion

Encyclopedia of Inorganic and Bioinorganic Chemistry, Online © 2011 John Wiley & Sons, Ltd.

This article was originally published in the *Encyclopedia of Inorganic Chemistry* in 2008 by John Wiley & Sons, Ltd.
DOI: 10.1002/9781119951438.eibc0303

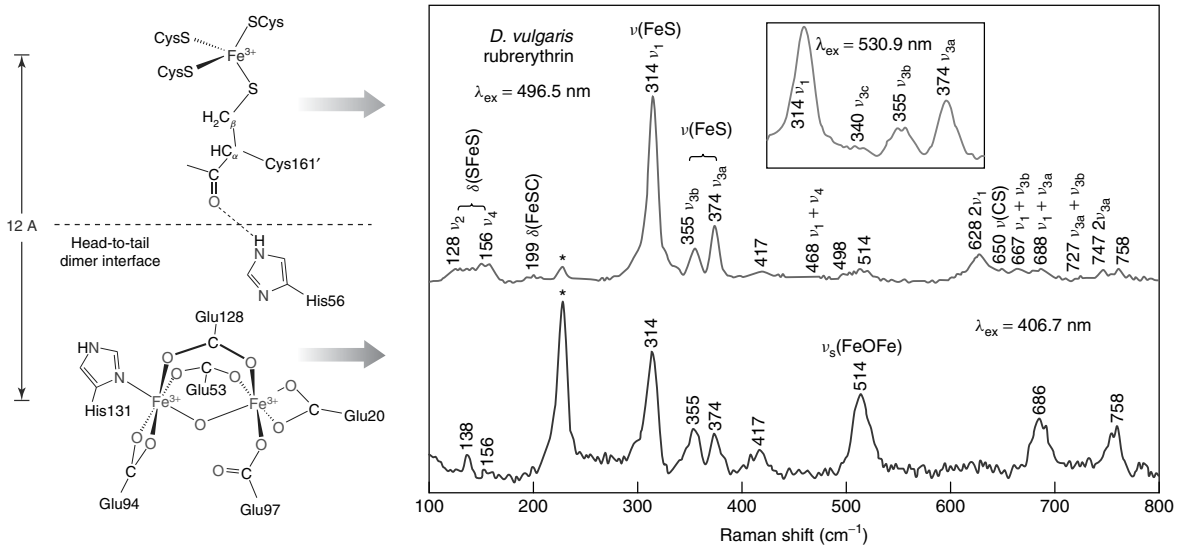

Figure 37 Low-temperature (77 K) RR spectra of *D. vulgaris* rubrerythrin obtained in the 100–800 cm^{-1} region with 496.5- (upper trace) and 406.7-nm (lower trace) excitation wavelengths. The spectrum excited at 496.5 nm is totally dominated by the bands arising from the $Fe(S\text{-}Cys)_4$ cluster, whereas that excited at 406.7 nm shows dramatically diminished intensities of the Fe–S bands with a concomitant enhancement of the band at 514 cm^{-1} assigned to ν_s(FeOFe) mode of a bent Fe–O–Fe cluster. Asterisks indicate the 228 cm^{-1} ice band

Table 8 Observed RR frequencies (cm^{-1}) and assignments for *D. gigas* rubredoxin and *D. vulgaris* rubrerythrin[a]

D. gigas rubredoxin	*D. vulgaris* rubrerythrin	Assignment
130	128	δ(SFeS),[b] ν_2,[c] $A_1(E)$[d]
150	156	δ(SFeS), ν_4, $E(T_2)$
174		δ(FeSC)
184	199	δ(FeSC)
314	314	ν(FeS), ν_1, $A_1(A_1)$
324		δ(SCC)
348	340	ν(FeS), ν_{3c}, $E(T_2)$
363	355	ν(FeS), ν_{3b}, $E(T_2)$
376	374	ν(FeS), ν_{3a}, $B_2(T_2)$
403	417	?
443	442	$\nu_1 + \nu_2$
463	468	$\nu_1 + \nu_4$
502	498	?
518	514	?
	514(−18)[+2][e]	ν_s(FeOFe)[f]
627	628	$2\nu_1$
653	650	ν(CS)
	667	$\nu_1 + \nu_{3b}$
	686[−1]	?
689	688	$\nu_1 + \nu_{3a}$
733	727	$\nu_{3a} + \nu_{3b}$
751	747	$2\nu_{3a}$
	758[−17]	?
757	759	$2\nu_1 + \nu_2$
777		$2\nu_1 + \nu_4$

[a]Rubredoxin data and assignments from Czernuszewicz *et al.*[89] Rubrerythrin data from Dave *et al.*[92]. ? = Indeterminate assignment. [b]δ(XYZ) and ν(XY) are bending and stretching coordinates involving the indicated atoms. [c]ν_{1-4} are normal modes of a XY_4 tetrahedron. [d]Symmetry designation for the $D_{2d}(T_d)$ point groups. [e]The numbers in () and [] indicate the frequency shifts in $H_2{}^{18}O$ and D_2O, respectively. [f]ν_s is the symmetric (in-phase) Fe–O–Fe stretching coordinate.

is ligated terminally by two glutamates, and the two Fe^{3+} ions are bridged by two bidentate glutamate ligands and an oxo (O^{2-}) group derived from the solvent. From the Fe···Fe (3.33 Å) and Fe–O (average 1.93 Å) distances,[96] the Fe–O–Fe angle of ∼120° can be calculated for the binuclear Fe(III) structure in rubrerythrin, which compares well with the bridge angle of 124° derived from RR spectroscopy. The Fe–O–Fe site is located close to the protein surface such that the μ-oxo-bridge is accessible to bulk solvent through a crevice formed between two α-helices (A and C).[91] Thus, intramolecular hydrogen bonding between the bridging μ-oxo group and H_2O can be anticipated and is responsible for the deuterium isotope effects on the ν_s(FeOFe) stretch in the RR spectrum of rubrerythrin (Figure 38).[92]

3.8 Cysteine Ligand Substitution in Rubredoxin

Systematic replacement of cysteine ligands at the $Fe(S\text{-}Cys)_4$ active site of rubredoxin[99,100] by site-directed mutagenesis has proven useful in probing many fundamental properties of iron–sulfur proteins.[99–104] For example, mutant forms of rubredoxin from *C. pasteurianum* (Rd*Cp*) in which each of its four cysteine ligands was replaced, in turn, with serine (C6S, C9S, C39S, and C42S)[99,101] constitute a set of four geometric isomers that have differently oriented $Fe(S\text{-}Cys)_3(O\text{-}Ser)$ centers within the same protein chain. Their properties fall into two pairs, depending upon whether a surface (C9, C42) or an interior (C6, C39) ligand is substituted (Figure 39). A comparison of the solution optical spectra of the WT protein and its surface ligand cysteine-to-serine mutants (C9S, C42S, and C9S/C42S) showed blue shifts of the absorption bands arising from (Cys)S → Fe(III)

Encyclopedia of Inorganic and Bioinorganic Chemistry, Online © 2011 John Wiley & Sons, Ltd.

This article was originally published in the *Encyclopedia of Inorganic Chemistry* in 2008 by John Wiley & Sons, Ltd.
DOI: 10.1002/9781119951438.eibc0303

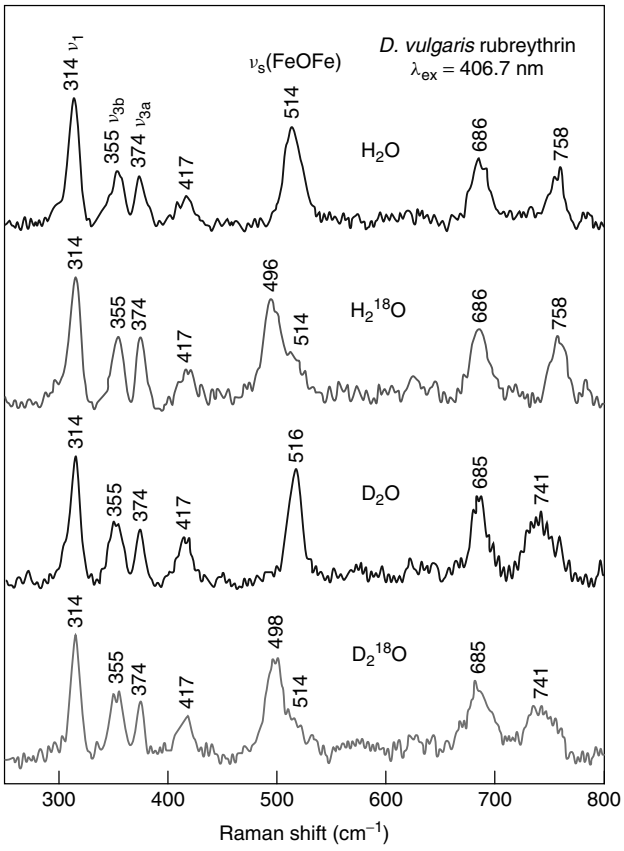

Figure 38 406.7-nm excited RR spectra of *D. vulgaris* rubrerythrin contained in H_2O, $H_2{}^{18}O$, D_2O, and $D_2{}^{18}O$ (frozen protein solutions at 77 K), showing the effects of $^{16/18}O$ and H/D exchange on the resonance-enhanced vibrational modes

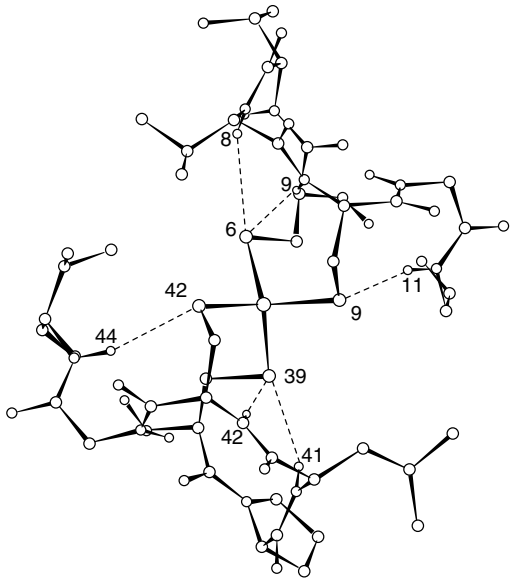

Figure 39 NH···S interactions (- - - -) around the Fe(S-Cys)$_4$ center in Rd*Cp* (pdb5rxn.ent).[105] A pseudo-2-fold axis is perpendicular to the page, passing through the Fe atom

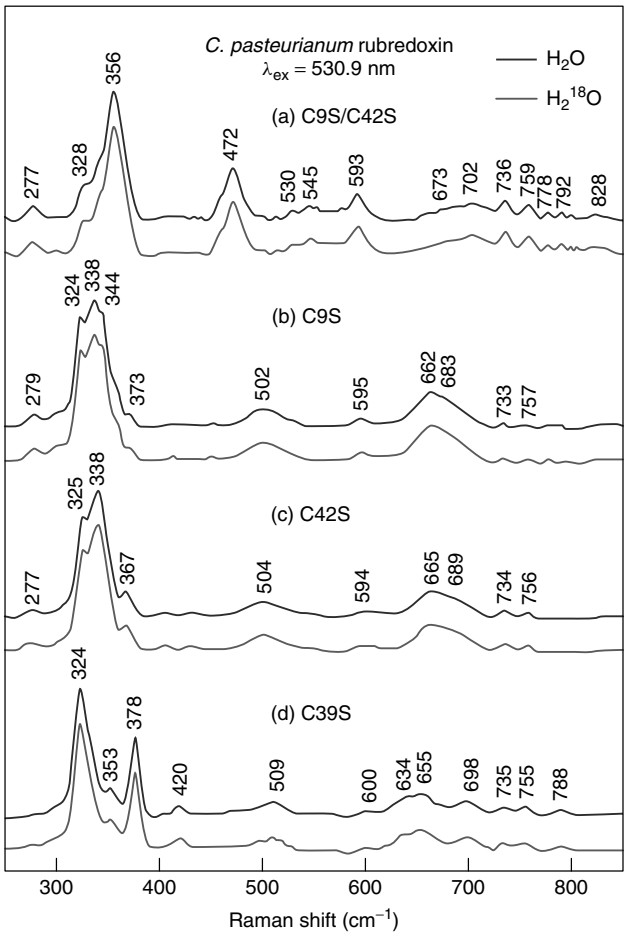

Figure 40 Low-temperature (77 K) RR spectra (530.9-nm excitation) of oxidized Rd*Cp* proteins: (a) C9S/C42S, (b) C9S, (c) C42S, and (d) C39S mutants in H_2O and $H_2{}^{18}O$

CT, consistent with the number of oxygen atoms increasing in the order FeS_4, FeS_3O, FeS_2O_2.[101] Figure 40 compares RR spectra for the C9S/C42S doubly mutated protein in H_2O and $H_2{}^{18}O$ with those of single mutants C9S, C42S, and C39S, using an excitation wavelength of 530.9 nm.[99] Each protein exhibits strong $\nu(FeS_{2,3})$ stretching modes of vibration in the range 325–475 cm^{-1} and a cluster of weaker overtone and combination bands associated with $\nu(FeS_{2,3})$ in the range 650–850 cm^{-1}, as expected for Raman scattering excited in resonance with the rubredoxin (Cys)S → Fe(III) CT transitions.[22,43,89,98] In addition, each gives a band at $597 \pm 4\,cm^{-1}$ that is not present in the WT protein spectrum. These frequencies (i) shift by 1.5–3.0 cm^{-1} to higher frequency in ^{54}Fe-reconstituted protein samples; (ii) do not shift in samples that have been freeze-dried and redissolved in $H_2{}^{18}O$ (compare with the C6S protein discussed later); and (iii) are independent of pH in the range pH 6–10. The new band at $597 \pm 4\,cm^{-1}$, which exhibited a ca. $+3\,cm^{-1}$ ^{54}Fe isotope upshift, may be assigned to $\nu(FeO_x)$ (x 1, 2) vibrational

Encyclopedia of Inorganic and Bioinorganic Chemistry, Online © 2011 John Wiley & Sons, Ltd.

This article was originally published in the *Encyclopedia of Inorganic Chemistry* in 2008 by John Wiley & Sons, Ltd.
DOI: 10.1002/9781119951438.eibc0303

modes, consistent with the presence of ferric $Fe(S\text{-}Cys)_3(O\text{-}Ser)$ and $Fe(S\text{-}Cys)_2(O\text{-}Ser)_2$ centers in the single and double mutants, respectively.[99] An enhancement of the Fe–O(Ser) stretching vibration is possible via kinematic coupling with the intense $\nu(FeS_{2,3})$ modes.

RR spectra of the interior ligand C6S mutant dissolved in H_2O and in isotopically labeled waters, $H_2{}^{18}O$ and D_2O, are presented in Figure 41.[99,100] Also shown there is the spectrum of C6S reconstituted with ^{54}Fe. The C6S spectra are independent of pH in the range 6–10, but in contrast to those of the other cysteine-to-serine mutants (Figure 40), it is sensitive to $H_2{}^{18}O$. A band at $\sim 617\,cm^{-1}$ in H_2O (Figure 41a), which occurs at $\sim 620\,cm^{-1}$ for the ^{54}Fe-reconstituted C6S protein (Figure 41b), and shifts down by $\sim 25\,cm^{-1}$ on $H_2{}^{18}O$ exchange (Figure 41c). This band must involve vibrational motion of an iron atom and a water-exchangeable oxygen atom and is attributed to a ν(FeOH) vibration of an Fe–OH fragment. Evidence that the $617\,cm^{-1}$ band is associated with a hydroxyl group is provided by its $13\,cm^{-1}$ *increase* in frequency in D_2O (Figure 41d), resulting from differential coupling of the stretching ν(FeOH) coordinate with the bending δ(FeOH) coordinate involving H or D atoms.[106] The frequencies of the δ(FeOH) bending modes are variable but can be close to $700\,cm^{-1}$ for strongly H-bonded hydroxyl groups. The interaction between ν(FeOH) at $617\,cm^{-1}$ and δ(FeOH) near $700\,cm^{-1}$ would be relieved in D_2O because of the large drop in the δ(FeOD) frequency. This would result in the observed *increase* of the ν(FeOD) stretching frequency. The observed upshift of $13\,cm^{-1}$, upon dissolution of C6S in D_2O, has been reproduced by a simplified NCA calculation with a three-atom Fe–O–H model using reasonable force constants and structure parameters.[99] The RR spectra of the C6S and C39S proteins are very similar, indicating the presence of a similar $Fe^{III}S_3O$ center in each protein. Thus, while an $[Fe^{III}(S\text{-}Cys)_3(O\text{-}Ser)]^-$ center is maintained in C39S, the weakness of a longer Fe(III)–O(Ser) bond in C6S has led to its hydrolysis and the presence of an $[Fe^{III}(S\text{-}Cys)_3(OH)]^-$ center and an unligated HO-Ser-6 residue. The $[Fe^{III}(S\text{-}Cys)_3(OH)]^-$ center in the C6S protein is a promising model system for a number of $M(S\text{-}Cys)_3$ sites, including the mononuclear iron sites in NifU and IscU proteins involved in the iron–sulfur cluster assembly.[103,104] The RR spectrum reported for the monomeric iron-binding site in NifU[103] is very similar to that of the C6S mutant of *C. pasteurianum* rubredoxin.[107]

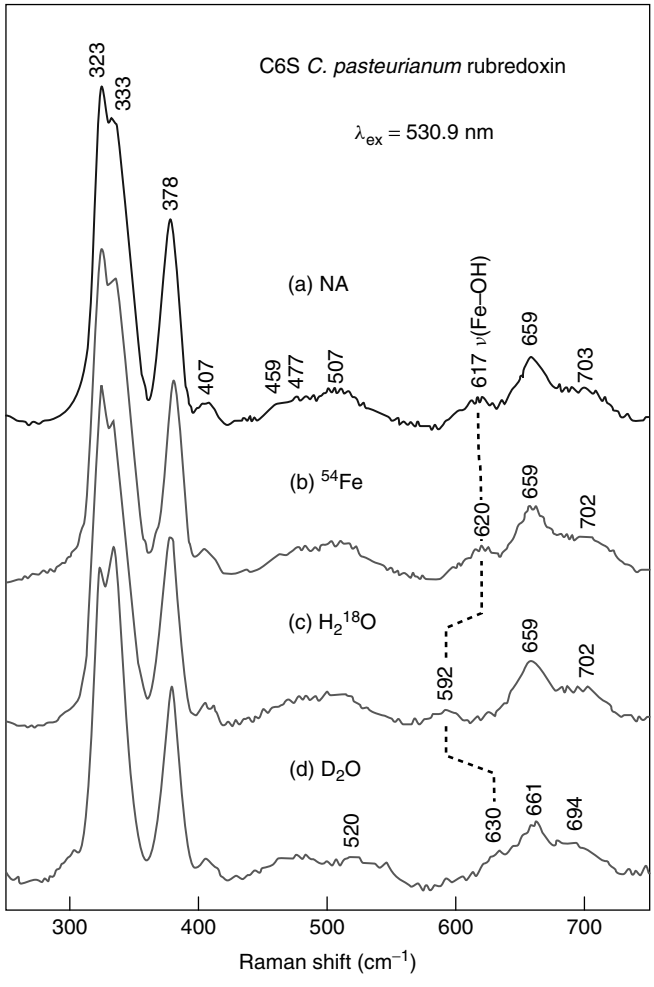

Figure 41 530.9-nm excited (77 K) RR spectra of C6S Rd*Cp* mutant: (a) in natural abundance, (b) ^{54}Fe-reconstituted protein, (c) in $H_2{}^{18}O$, and (d) in D_2O

4 FURTHER READING

R. S. Czernuszewicz, E. M. Maes, and J. G. Rankin, *Resonance Raman Spectroscopy of Petroporphyrins*, in eds. K. M. Kadish, K. M. Smith and R. Guilard, 'The Porphyrin Handbook', Academic Press, 2000, Vol. 7. Metalloporphyrins have provided a particularly rich opportunity for resonance Raman studies and this book chapter discusses various aspects of pioneering work in the area of geological metalloporphyrins.

R. S. Czernuszewicz and T. G. Spiro, *IR, Raman and Resonance Raman Spectroscopy* in eds. E. I. Solomon and A. B. P. Lever, 'Inorganic Electronic Structure and Spectroscopy', John Wiley & Sons, New York, 1999, Vol. I, Methodology. A detailed compilation of the principles of IR, Raman, and resonance Raman spectroscopies and their applications in bioinorganic chemistry.

M. Diem, 'Introduction to Modern Vibrational Spectroscopy', John Wiley & Sons, New York, 1993. This easy to read book features detailed discussion of the theoretical and experimental aspects of IR and Raman spectroscopy and provides many examples for the interpretation of vibrational spectra.

J. R. Ferraro and K. Nakamoto, 'Introductory Raman Spectroscopy', Academic Press, New York, 1994. A well-balanced Raman text on an introductory level that explains basic theory, instrumentation and experimental techniques (including special techniques), and a wide variety of applications in structural chemistry, biochemistry, biology and medicine, solid-state chemistry and industry will serve well as a guide for beginners.

Encyclopedia of Inorganic and Bioinorganic Chemistry, Online © 2011 John Wiley & Sons, Ltd.

This article was originally published in the *Encyclopedia of Inorganic Chemistry* in 2008 by John Wiley & Sons, Ltd.
DOI: 10.1002/9781119951438.eibc0303

D. C. Harris and M. D. Bertolucci, 'Symmetry and Spectroscopy: An Introduction to Vibrational and Electronic Spectroscopy', Oxford University Press, New York, 1979. Easy-to-follow, instructive textbook on vibrational and electronic spectroscopy with numerous helpful figures, line drawings, and exercises illustrating important concepts. Excellent choice for anyone teaching or studying molecular spectroscopy at junior to beginning graduate level. Also available in paperback from Dover, New York.

J. R. Kincaid, *Resonance Raman Spectra of Heme Proteins and Model Compounds*, in eds. K. M. Kadish, K. M. Smith and R. Guilard, 'The Porphyrin Handbook', Academic Press, New York, 2000, Vol. 7. An excellent review that summarizes and clearly illustrates the power of RR spectroscopy in probing structure–function relationships for a wide variety of heme proteins.

I. R. Lewis and H. G. M. Edwards eds, 'Handbook of Raman Spectroscopy', Marcell Dekker Inc, New York, 2001. This comprehensive handbook lays out the richness and technical details of Raman techniques, instrumentation and measurements now employed in a variety of industrial and academic research fields.

D. A. Long, 'Raman Spectroscopy', McGraw-Hill, New York, 1977. The most comprehensive, unified and fully illustrated treatment of the basic theory and physical principles of Raman, resonance Raman and nonlinear Raman scattering. Readers will be inspired by the elegance and information content of the technique to delve further into the book.

K. Nakamoto, 'Infrared and Raman Spectra of Inorganic and Coordination Compounds', Wiley-Interscience, New York, 1997. Unsurpassed resource textbook available for researchers and graduate students in the field of vibrational spectroscopy, inorganic chemistry, organometallic chemistry, and bioinorganic chemistry.

E. Smith and G. Dent, 'Modern Raman Spectroscopy', John Wiley & Sons, New York, 2005. A practical approach to modern Raman spectroscopy that provides the information necessary to enable new users to understand and apply the technique correctly, including descriptions of the many pitfalls that can be encountered.

T. G. Spiro ed, 'Biological Applications of Raman Spectroscopy', Wiley-Interscience, 1988, Vol. 1–3. Through summaries of representative areas by authorities in biological Raman applications, this set of three volumes provides in-depth coverage of the theoretical and experimental aspects of modern bio-Raman spectroscopy.

E. B. Wilson Jr, J. C. Decius, and P. C. Cross, 'Molecular Vibrations: The Theory of Infrared and Raman Vibrational Spectra', McGraw-Hill, New York, 1955. Classic graduate text; contains rigorous yet easily followed exposition of mathematics involved in detailed vibrational analyses of polyatomic molecules. Also available in paperback from Dover, New York.

5 REFERENCES

1. R. J. H. Clark and B. Stewart, *Struct. Bond.*, 1979, **36**, 1.
2. R. J. H. Clark, *Resonance Raman Spectra of Inorganic Molecules and Ions*, in 'Advances in IR and Raman Spectroscopy', eds. R. J. H. Clark and R. E. Hester, John Wiley & Sons, New York, 1975, Vol. 1, p. 143.
3. C. L. Angel, F. A. Cotton, B. A. Frenz, and T. A. Webb, *Chem. Commun.*, 1973, 399.
4. R. J. H. Clark and M. L. Franks, *J. Am. Chem. Soc.*, 1975, **97**, 2691.
5. C. D. Cowman and H. B. Gray, *J. Am. Chem. Soc.*, 1973, **95**, 8177.
6. F. A. Cotton, *Chem. Soc. Rev.*, 1975, **4**, 27.
7. T. C. Strekas and T. G. Spiro, *Biophys. Biochim. Acta*, 1972, **263**, 830.
8. T. C. Strekas and T. G. Spiro, *Biophys. Biochim. Acta*, 1972, **278**, 188.
9. T. G. Spiro and T. C. Streaks, *Proc. Natl. Acad. Sci.*, 1972, **69**, 2622.
10. T. G. Spiro and T. C. Strekas, *Acc. Chem. Res.*, 1974, **7**, 339.
11. T. G. Spiro and T. M. Loehr, *Resonance Raman Spectra of Heme Proteins and Other Biological Systems*, in 'Advances in IR and Raman Spectroscopy', eds. R. J. H. Clark and R. E. Hester, John Wiley & Sons, New York, 1975, Vol. 1, p. 98.
12. T. G. Spiro, *The Resonance Raman Spectroscopy of Metalloporphyrins and Heme Proteins*, in 'Iron Porphyrins', eds. A. B. P. Lever and H. B. Gray, Addison-Wesley, Reading, MA, 1983, p. 89.
13. T. G. Spiro, ed, 'Biological Applications of Raman Spectroscopy: Resonance Raman Spectra of Heme and Metalloproteins', John Wiley & Sons, New York, 1987, Vol. 3.
14. J. R. Kincaid, *Resonance Raman Spectra of Heme Proteins and Model Compounds*, in 'The Porphyrin Handbook', eds. K. M. Kadish, K. M. Smith, and R. Guilard, Academic Press, San Diego, 2000, Vol. 7, p. 225.
15. J. Behringer, *Observed Resonance Raman Spectra*, in 'Raman Spectroscopy. Theory and Practice', ed. H. A. Szymanski, Plenum Press, New York, 1967, Vol. 1, p. 168.
16. T. G. Spiro and R. S. Czernuszewicz, *Meth. Enzym.*, 1995, **246**, 416.
17. Y. Wang and H. E. Van Wart, *Meth. Enzym.*, 1993, **226**, 319.
18. T. M. Loehr and J. Sanders-Loehr, *Meth. Enzym.*, 1993, **226**, 431.
19. I. R. Lewis and H. G. M. Edwards, eds, 'Handbook of Raman Spectroscopy', Marcel Dekker, Inc., New York, 2001.
20. K. Nakamoto and R. S. Czernuszewicz, *Meth. Enzym.*, 1993, **226**, 259.
21. R. S. Czernuszewicz and T. G. Spiro, *IR, Raman and Resonance Raman Spectroscopy*, in 'Inorganic Electronic Structure and Spectroscopy', eds. E. I. Solomon and A. B. P. Lever, John Wiley & Sons, New York, 1999, p. 353.
22. T. G. Spiro and R. S. Czernuszewicz, *Resonance Raman Spectroscopy*, in 'Physical Methods in Bioinorganic Chemistry', ed L. Que Jr, University Science Books, Sausalito, CA, 2000, p. 59.

Encyclopedia of Inorganic and Bioinorganic Chemistry, Online © 2011 John Wiley & Sons, Ltd.

This article was originally published in the *Encyclopedia of Inorganic Chemistry* in 2008 by John Wiley & Sons, Ltd.
DOI: 10.1002/9781119951438.eibc0303

23. J. A. Koningsten, 'Introduction to the Theory of the Raman Effect', Reidel, Dordrecht, The Netherlands, 1973.
24. D. A. Long, 'Raman Spectroscopy', McGraw-Hill, New York, 1977.
25. C. V. Raman and K. S. Krishnam, *Nature*, 1928, **121**, 501.
26. C. V. Raman and K. S. Krishnam, *Nature*, 1928, **121**, 619.
27. G. S. Landsberg and L. J. Mandelstam, *Naturwissenschaften*, 1928, **16**, 557.
28. R. S. Czernuszewicz and M. K. Johnsson, *Appl. Spectrosc.*, 1983, **37**, 297.
29. R. S. Czernuszewicz, *Appl. Spectrosc.*, 1983, **40**, 571.
30. D. P. Strommen and K. Nakamoto, 'Laboratory Raman Spectroscopy', John Wiley & Sons, New York, 1984.
31. T. G. Spiro and H.-Y. Li, *Resonance Raman Spectroscopy of Metalloporphyrins*, in 'Biological Applications of Raman Spectroscopy', ed. T. G. Spiro, John Wiley & Sons, New York, 1988, Vol. 3, p. 1.
32. T. G. Spiro, R. S. Czernuszewicz, and X.-Y. Li, *Coord. Chem. Rev.*, 1990, **100**, 541.
33. R. S. Czernuszewicz, E. M. Maes, and J. G. Rankin, *Resonance Raman Spectroscopy of Petroporphyrins*, in 'The Porphyrin Handbook', eds. K. M. Kadish, K. M. Smith, and R. Guilard, Academic Press, San Diego, 2000, Vol. 7, p. 293.
34. W. Siebrand and M. Z. Zgierski, *Resonance Raman Spectra–A Key to Vibronic Coupling*, in 'Excited States', ed. E. C. Lim, Academic Press, New York, 1979, Vol. 4, p. 1.
35. T. G. Spiro and P. Stein, *Ann. Rev. Phys. Chem.*, 1977, **28**, 501.
36. A. C. Albrecht, *J. Chem. Phys.*, 1961, **34**, 1476.
37. J. Tang and A. C. Albrecht, *J. Chem. Phys.*, 1968, **49**, 1144.
38. A. C. Albrecht, *J. Chem. Phys.*, 1960, **33**, 937.
39. R. J. H. Clark and T. J. D. Dines, *Angew. Chem. Int. Ed. Engl.*, 1986, **25**, 131.
40. J. G. Rankin and R. S. Czernuszewicz, *Org. Geochem.*, 1993, **20**, 521.
41. M. Gouterman, *Optical Spectra and Electronic Structure of Porphyrin and Related Rings*, in 'The Porphyrins', ed. D. Dolphin, Academic Press, New York, 1979, Vol. 3, p. 1.
42. Q. Yan, '*Applications of Resonance Raman Spectroscopy to Complexes of Biological and Clinical Significance: I. High-Valent Oxo- and Nitridometalloporphyrins; II. μ-Oxo Vanadium(III) Dimers; III. Antitumor Drug-DNA Intercalators*,' PhD. Dissertation, University of Houston, 1996.
43. R. S. Czernuszewicz and E. M. Maes, *Biological Applications of Resonance Raman Spectroscopy: Copper-Cysteinate Active Sites*, in 'Education in Advanced Chemistry', eds. A. M. Trzeciak, P. Sobota, and J. J. Ziolkowski, Wydawnictwo Poznanskie, Poznan-Wroclaw, Poland, 2000, Vol. 7, p. 67.
44. R. S. Czernuszewicz, B. C. Dave, and J. P. Germanas, *A Probe of Metal-Ligand Interactions in Cupredoxin by Active Site Redesign and Resonance Raman Spectroscopy*, in 'Spectroscopic Methods in Bioinorganic Chemistry', eds. E. I. Solomon and K. O. Hodgson, American Chemical Society, Washington, DC, 1997, Vol. 692, p. 220.
45. J. Sanders-Loehr, 'Bioinorganic Chemistry of Copper', eds. K. D. Karlin and Z. Tyeklar, Chapmaan & Hall, New York, 1993, p. 51.
46. C. R. Andrew and J. Sanders-Loehr, *Acc. Chem. Res.*, 1996, **29**, 365.
47. W. H. Woodruff, R. B. Dyer, and J. R. Schoonover, *Resonance Raman Spectroscopy of Blue Copper Proteins*, in 'Biological Applications of Raman Spectroscopy', eds. T. G. Spiro and X.-Y. Li, John Wiley & Sons, New York, 1988, Vol. 3, p. 413.
48. E. N. Baker, *J. Mol. Biol.*, 1988, **203**, 1071.
49. H. Nar, A. Messerschmidt, and R. Huber, *J. Mol. Biol.*, 1991, **221**, 765.
50. B. R. Crane, A. J. Di Bilio, J. R. Winkler, and H. B. Gray, *J. Am. Chem. Soc.*, 2001, **123**, 11623.
51. E. T. Adman, *Copper Protein Structures*, in 'Advances in Protein Chemistry', eds. C. B. Anifsen, J. T. Edsall, F. M. Richards, and D. S. Eisenberg, Academic Press, New York, 1991, Vol. 42, p. 45.
52. D. Qiu, L. Kilpatrick, N. Kitajima, and T. G. Spiro, *J. Am. Chem. Soc.*, 1994, **116**, 2585.
53. N. Kitajima, F. Kiyoshi, and M. Yoshihiko, *J. Am. Chem. Soc.*, 1990, **112**, 3210.
54. L. Nestor, J. A. Larrabee, G. Woolery, B. Reinhammer, and T. G. Spiro, *Biochemistry*, 1984, **23**, 1084.
55. B. C. Dave, J. P. Germanas, and R. S. Czernuszewicz, *J. Am. Chem. Soc.*, 1993, **115**, 12175.
56. R. S. Czernuszewicz, G. Fraczkiewicz, R. Fraczkiewicz, B. C. Dave, and J. P. Germanas, *Ground and Excited State Dynamics of Blue Copper Active Site from Resonance Raman Spectroscopy of Azurin*, in 'Spectroscopy of Biological Molecules', eds. J. C. Merlin, S. Turrel, and J. P. Huvenne, Kluwer Academic Publishers, Dordrecht, The Netherlands, 1995, p. 273.
57. C. R. Andrew, H. Yeom, J. S. Valentine, B. G. Karlsson, N. Bonander, G. van Pouderoyen, G. Centers, T. M. Loehr, and J. Sanders-Loehr, *J. Am. Chem. Soc.*, 1994, **116**, 11489.
58. A. M. Nersissian, Z. B. Mehrabian, R. M. Nalbandyan, P. J. Hart, G. Fraczkiewicz, R. S. Czernuszewicz, C. J. Bender, J. Peisach, R. G. Herrmann, and J. S. Valentine, *Protein Sci.*, 1996, **5**, 2184.
59. D. Qiu, S. Dong, J. A. Ybe, M. H. Hecht, and T. G. Spiro, *J. Am. Chem. Soc.*, 1995, **117**, 6443.
60. G. Fraczkiewicz, N. Bonander, and R. S. Czernuszewicz, *J. Raman Spectrosc.*, 1998, **29**, 983.
61. G. Franczkiewicz, R. Franczkiewicz, J. P. Germanas, and R. S. Czernuszewicz, 'Proceedings of the XVth International Conference on Raman Spectroscopy', John Wiley & Sons, New York, 1996, p. 408.

Encyclopedia of Inorganic and Bioinorganic Chemistry, Online © 2011 John Wiley & Sons, Ltd.

This article was originally published in the *Encyclopedia of Inorganic Chemistry* in 2008 by John Wiley & Sons, Ltd.
DOI: 10.1002/9781119951438.eibc0303

62. S. Dong and T. G. Spiro, *J. Am. Chem. Soc.*, 1998, **120**, 10434.
63. D. Qiu, S. Dasgupta, P. M. Kozlowski, and T. G. Spiro, *J. Am. Chem. Soc.*, 1998, **120**, 12791.
64. D. F. Blair, G. W. Campbell, J. R. Schoonover, S. I. Chan, H. B. Gray, B. G. Malmstrom, I. Pecht, B. I. Swanson, W. H. Woodruff, W. K. Cho, A. M. English, H. A. Fry, V. Lum, and K. A. Norton, *J. Am. Chem. Soc.*, 1985, **107**, 5755.
65. G. van Pouderoyen, C. R. Andrew, T. M. Loehr, J. Sanders-Loehr, S. Mazamudar, H. A. O. Hill, and G. W. Canters, *Biochemistry*, 1996, **35**, 1397.
66. T. den Blaauwen and G. W. Canters, *J. Am. Chem. Soc.*, 1993, **115**, 1121.
67. C. R. Andrew, J. Han, T. den Blaauwen, G. van Pouderoyen, E. Vijgenboom, G. W. Canters, T. M. Loehr, and J. Sanders-Loehr, *J. Bioinorg. Chem.*, 1997, **2**, 98.
68. J. Han, T. M. Loehr, Y. Lu, J. S. Valentine, B. A. Averill, and J. Sanders-Loehr, *J. Am. Chem. Soc.*, 1993, **115**, 4256.
69. N. Bonander, B. G. Karlsson, and T. Vanngard, *Biochemistry*, 1996, **35**, 2429.
70. R. S. Czernuszewicz, G. Fraczkiewicz, and A. A. Zareba, *Inorg. Chem.*, 2005, **44**, 5745.
71. J. M. Moratal, A. Romero, J. Salgado, A. Perales-Alarcon, and H. R. Jimenez, *Eur. J. Biochem.*, 1995, **228**, 653.
72. J. P. Hannan, S. L. Davy, R. R. Eady, and C. R. Andrew, *J. Biol. Inorg. Chem.*, 1998, **3**, 282.
73. G. Musci, A. Desideri, L. Morpurgo, and L. Tosi, *J. Inorg. Biochem.*, 1985, **23**, 93.
74. T. Kohzuma, M. Kikuchi, N. Horikoshi, S. Nagatomo, T. Kitagawa, and R. S. Czernuszewicz, *Inorg. Chem.*, 2006, **45**, 8474.
75. J. G. Grossmann, Z. H. L. Abraham, E. T. Adman, M. Neu, R. R. Eady, B. E. Smith, and S. S. Hasnain, *Biochemistry*, 1993, **32**, 7360.
76. M. Kukimoto, M. Nishiyama, M. E. Murphy, S. Turly, E. T. Adman, S. Horinouchi, and T. Beppu, *Biochemistry*, 1994, **33**, 5246.
77. S. V. Antonyuk, R. W. Strange, G. Sawers, R. R. Eady, and S. S. Hasnain, *Proc. Natl. Acad. Sci.*, 2005, **102**, 12041.
78. M. A. Hough, M. J. Ellis, S. V. Antonyuk, R. W. Strange, G. Sawers, R. R. Eady, and S. S. Hasnain, *J. Mol. Biol.*, 2005, **350**, 300.
79. T. G. Spiro, R. S. Czernuszewicz, and S. Han, *Iron-Sulfur Proteins and Analog Complexes*, in 'Biological Applications of Raman Spectroscopy', ed. T. G. Spiro, John Wiley & Sons, New York, 1988, Vol. 3, p. 523.
80. S. Han, R. S. Czernuszewicz, T. Kimura, M. W. W. Adams, and T. G. Spiro, *J. Am. Chem. Soc.*, 1989, **111**, 3505.
81. S. Han, R. S. Czernuszewicz, and T. G. Spiro, *J. Am. Chem. Soc.*, 1989, **111**, 3496.
82. M. K. Johnson, R. S. Czernuszewicz, T. G. Spiro, J. A. Fee, and W. V. Sweeney, *J. Am. Chem. Soc.*, 1983, **115**, 6671.
83. M. K. Johnson, R. S. Czernuszewicz, T. G. Spiro, R. R. Ramsay, and T. P. Singer, *J. Biol. Chem.*, 1983, **258**, 12771.
84. R. S. Czernuszewicz, K. A. Macor, M. K. Johnson, A. Gewirth, and T. G. Spiro, *J. Am. Chem. Soc.*, 1987, **109**, 7178.
85. E. M. Walters, R. Garcia-Serres, G. N. L. Jameson, D. A. Glauser, F. Bourquin, W. Manieri, P. Schurmann, M. K. Johnson, and B. H. Huynh, *J. Am. Chem. Soc.*, 2005, **127**, 9612.
86. T. V. Long and T. M. Loehr, *J. Am. Chem. Soc.*, 1970, **92**, 6384.
87. T. V. Long, T. M. Loehr, J. R. Alkins, and W. Lovenberg, *J. Am. Chem. Soc.*, 1971, **93**, 1809.
88. L. A. Woodward and M. J. Taylor, *J. Chem. Soc.*, 1960, 4473.
89. R. S. Czernuszewicz, J. LeGall, I. Moura, and T. G. Spiro, *Inorg. Chem.*, 1986, **25**, 696.
90. W. A. Eaton and W. Lovenberg, *The Iron-Sulfur Complex in Rubredoxin*, in 'Iron Sulfur Proteins', ed. W. Lovenberg, Academic Press, New York, 1973, Vol. 12, p. 131.
91. R. S. Czernuszewicz, L. K. Kilpatrick, S. A. Koch, and T. G. Spiro, *J. Am. Chem. Soc.*, 1994, **116**, 7134.
92. B. C. Dave, R. S. Czernuszewicz, B. C. Prickril, and D. M. Kurtz Jr, *Biochemistry*, 1994, **33**, 3572.
93. J. LeGall, B. C. Prickril, I. Moura, A. V. Xavier, J. J. G. Moura, and B. Huynh, *Biochemistry*, 1988, **27**, 1636.
94. I. Moura, P. Tavares, and N. Ravi, *Meth. Enzym.*, 1993, **243**, 216.
95. F. deMare, D. M. Kurtz Jr, and P. Nordlund, *Nat. Struct. Biol.*, 1996, **3**, 539.
96. S. Jin, D. M. Kurtz Jr, Z.-J. Liu, J. Rose, and B.-C. Wang, *J. Am. Chem. Soc.*, 2002, **124**, 9845.
97. M. Li, M. Liu, L. Gall, L. Gui, J. Liao, T. Jiang, J. Zhang, D. Liang, and W. Chang, *J. Biol. Inorg. Chem.*, 2003, **8**, 146.
98. Y. Xiao, H. Wang, S. J. George, M. C. Smith, M. W. W. Adams, F. E. Jenney, Jr., W. Sturhahn, E. E. Alp, J. Zhao, Y. Yoda, A. Dey, E. I. Solomon, and S. P. Cramer, *J. Am. Chem. Soc.*, 2005, **127**, 14596.
99. Z. Xiao, A. R. Gardner, M. Cross, E. M. Maes, R. S. Czernuszewicz, M. Sola, and A. G. Wedd, *J. Biol. Inorg. Chem.*, 2001, **6**, 638.
100. M. Cross, Z. Xiao, E. M. Maes, R. S. Czernuszewicz, S. C. Drew, J. R. Pilbrow, G. N. George, and A. G. Wedd, *J. Biol. Inorg. Chem.*, 2002, **7**, 781.
101. Z. Xiao, M. J. Lavery, M. Ayhan, S. D. B. Scrofani, M. C. J. Wilce, J. M. Guss, P. A. Tregloan, G. N. George, and A. G. Wedd, *J. Am. Chem. Soc.*, 1998, **120**, 4135.
102. J. Meyer, J. Gaillard, and M. Lutz, *Biochem. Biophys. Res. Commun.*, 1995, **212**, 827.
103. J. N. Agar, P. Yuvanyiama, R. F. Jack, V. L. Cash, D. R. Smith, D. R. Dean, and M. K. Johnson, *J. Biol. Inorg. Chem.*, 2000, **5**, 167.

Encyclopedia of Inorganic and Bioinorganic Chemistry, Online © 2011 John Wiley & Sons, Ltd.

This article was originally published in the *Encyclopedia of Inorganic Chemistry* in 2008 by John Wiley & Sons, Ltd.
DOI: 10.1002/9781119951438.eibc0303

104. J. N. Agar, L. Zheng, V. L. Cash, D. R. Dean, and M. K. Johnson, *J. Am. Chem. Soc.*, 2000, **122**, 2136.

105. K. D. Watenpaugh, L. C. Sieker, and L. H. Jensen, *J. Mol. Biol.*, 1980, **138**, 615.

106. R. S. Czernuszewicz, Y. O. Su, M. K. Stern, K. A. Macor, D. Kim, J. T. Groves, and T. G. Spiro, *J. Am. Chem. Soc.*, 1988, **110**, 4158.

107. E. M. Maes, '*Structural Characterization of Iron and Copper Active Sites by Resonance Raman Spectroscopy: Nitrophorin, Nitrite Reductase, and Iron-Sulfur Proteins*,' PhD. Dissertation, University of Houston, 2000.

Encyclopedia of Inorganic and Bioinorganic Chemistry, Online © 2011 John Wiley & Sons, Ltd.

This article was originally published in the *Encyclopedia of Inorganic Chemistry* in 2008 by John Wiley & Sons, Ltd.
DOI: 10.1002/9781119951438.eibc0303